DEPOSITION OF Co_xS_y , Ni_xS_y, MnS and CdS THIN FILMS FROM THEIR ALKYLTHIOUREA PRECURSORS USING THE AEROSOL ASSISTED CHEMICAL VAPOUR DEPOSITION(AACVD) TECHNIQUE

A dissertation submitted by

LONDIWE PATIENCE MGABI

(St. No. 990486)

To the Department of Chemistry, University of Zululand

In fulfillment of the requirement for the award of the degree of

Master of Science

in Chemistry

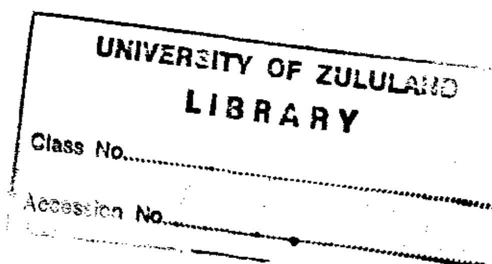
UNIVERSITY OF ZULULAND
LIBRARY
Class No.
Accession No.

Supervisor: Prof. N. Revaprasadu

Co- Supervisor : Dr J. Moloto

Declaration

"I declare that Deposition of Co_xS_y, Ni_xS_y, MnS and CdS thin films using alkylthiourea precursors by the Aerosol Assisted Chemical Vapour Deposition (AACVD) Technique" is entirely my own work, which was conducted in the Department of Chemistry at the University of Zululand and in the Department of Materials Science and Engineering at the University of Manchester. I declare that all the sources used or quoted have been indicated and acknowledged by means of complete references"

Mgabhi, Londiwe Patience

....

Abstract

Various complexes of Co (II), Ni (II), Mn (II) and Cd (II) thiourea and alkylthiourea have been successfully synthesized, using the 1:2 mole ratio metal salts of ($NiCl_2$, $CoCl_2$, $MnCl_2$ and $CdCl_2$) with their respective ligands. These complexes were characterized using melting points and elemental analysis to distinguish their monomeric character and confirm the purity of the complexes. Single X-ray crystal structures of $[NiCl_2(SC(NHC_6H_{11})_2)]_2$ and $[MnCl_2(CS(NH_2)_2)_4]$ were obtained.

Thermogravimetric studies on each complex were conducted to elucidate their volatility, for the deposition of thin films. Their decomposition patterns were found to yield predominantly a 2-stage TGA profiles with the resultant leading to the formation of the respective metal sulfide. Thin films were successfully deposited via the single source precursor method on glass and GaAs substrates by the Aerosol Assisted Chemical Vapour Deposition (AACVD) technique. Their lower volatility nature yielded less uniform deposition of thin films such that the substrate was changed as well the suspension of the substrate on the stubs with improved uniformity of the thin film. The respective metal chalcogenide thin films deposited were characterized by X-ray Diffraction (XRD) for their crystallinity, Scanning Electron Microscopy (SEM) for their morphological properties, Ultraviolet (UV) - Visible (Vis) spectra for their optical properties and Energy Dispersive X-ray (EDAX) for the composition of the films. Thin film measurement was performed using the Interferometer method.

The X-ray diffraction pattern revealed different phases for the metal chalcogenide film, stoichiometric cobalt sulfide exhibited a mixture of cubic linnaeite Co_3S_4 and cattierite CoS_2, stoichiometric NiS, NiS_2 (pyrite), β- NiS (millerite), $Ni_{3-x}S_2$ and $NiS_{1.97}$, Manganese sulfide revealed the presence of the α - alabandite phase and CdS showed the mixture of hexagonal and orthorhombic (300-350 °C) and cubic phase at (400-450 °C) respectively. Their morphological properties demonstrated the presence of mostly granulated spheres for the stoichiometric CoS, star-fish like rods for stoichiometric NiS, polycrystalline growth for the MnS films and mostly cubic and spore-like rods for CdS. Their absorption spectra revealed blue-shifted spectra with a mostly a higher optical band

gap energy relative to that of bulk for all the metal chalcogenides. Thickness measurements showed that most thin films were deposited uniformly with minor contours and showed optimum adherence to the substrates.

CONTENTS

Title page i
Declaration ii
Abstract iii
Contents v
List of tables ix
List of abbreviations x
List of figures xi
Acknowledgements xiv
Dedication xv

CHAPTER 1 : **Background to semiconductor thin films**

1. General Background 2
1.1 Introduction on the theory of semiconductor thin films 2
1.2 Direct and Indirect semiconductors 4
1.3 Background of Chemical Vapour Deposition (CVD) 5
1.3.1 Processes of Chemical Vapour Deposition 6
1.3.2 Processes principles and deposition mechanism 7
1.3.2.1 Advantages and disadvantages of CVD 8
1.4 Thin film CVD techniques 9
1.4.1 Metal Organic Chemical Vapour Deposition (MOCVD) 9
1.4.1.1 Limitations of MOCVD 10
1.4.2 Flame Assisted Chemical Vapour Deposition (FACVD) 10
1.4.2.1 Advantages of FACVD 12
1.4.2.2 Limitations of FACVD 12
1.4.3 Plasma Electron Chemical Vapour Deposition (PECVD) 12
1.4.3.1 Limitations of PECVD 13
1.4.3.2 Advantages of PECVD 14
1.4.4 Aerosol Assisted Chemical Vapour Deposition (AACVD) 14

1.4.4.1 Principles and Characteristics of AACVD 15
1.4.4.2 Ultrasonic aerosol generation 17
1.4.4.3 Evaporation of aerosol droplets 18
1.4.4.4 Adsorption of solution constituents onto substrate 19
1.4.4.5 Advantages of AACVD 21
1.5 The rate of deposition on film growth 22
1.6 Difference between dual source and single source precursor 23
1.7 Literature review on the use of single source precursor methods 24
1.8 Properties of CoS, NiS, MnS and CdS yielding feasibility for thin film 26
1.8.1 Manganese sulphides 26
1.8.2 Cobalt sulphides 27
1.8.3 Nickel sulphides 28
1.8.4 Cadmium sulphide 28
1.9 Precursors of semiconductor thin films 29
1.10 Applications of semiconductor thin films 30
1.10.1 Semiconductor films for microelectronics 30
1.11 Applications in Optoelectronics 34
1.12 Thin film structure 36
1.13 Techniques for studying thin film structure 38
1.13.1 X-ray methods 39
1.13.1.1 X-ray diffraction 39
1.13.2 Electronic methods 41
1.13.2.1 Transmission (TEM) and Replication (REM) Electron microscopy 41
1.13.3 Scanning Electron Microscopy 42
1.13.4 Optical Methods 44
1.13.5 Chemical Methods 45
1.13.5.1 Selective Chemical Etching for crystalline films or substrates 46
1.14 Substrates 47
1.14.1 Classification and requirements 47
1.14.2 Properties and uses of substrates 49
1.15 Measurement of thin film thickness 50

1.15.1 Mechanical Methods 51
1.15.1.1 Sample weighing method 51
1.15.1.2 Profilometer Method 52
1.15.1.3 Interferometer Method 53

CHAPTER 2 : **Synthesis of complexes for the deposition of thin films**

2. Experimental Section 56
2.1 Reagents and Materials 56
2.1.1 Instrumentation 56
2.1.2 Preparation of Precursors 57
2.1.2.1 Synthesis of Cobalt Precursors 57
2.1.2.2 Synthesis of Nickel Precursors 58
2.1.2.3 Synthesis of Manganese Precursors 60
2.1.2.4 Synthesis of Cadmium Precursors 61
2.2 Results and Discussion 62
2.2.1 Synthesis of all precursors 62
2.2.2 Infrared Studies 63
2.2.3 Single X-ray crystallography 64
2.2.4 Conclusions 73

CHAPTER 3 : **Deposition of metal chalcogenide thin films**

3.1 General Introduction 75
3.2 Experimental section - Preparation of thin films 76
3.2.1 Chemicals and Materials 76
3.2.2 Instrumentation 76
3.2.2.1 Thermogravimetric analysis (TGA) 76
3.2.2.2 X- ray diffraction (XRD) 76
3.2.2.3 Scanning electron microscopy (SEM) 77
3.2.2.4 Uv- vis spectroscopy 77

3.2.2.5 Scanning Interferometer 77
3.3 Substrate cleaning Procedures 77
3.3.1 General cleaning method 77
3.3.2 Glass wet chemical etching 77
3.3.3 Piranha clean 78
3.4 Thin film deposition by CVD 79
3.4.1 Growth of thin films by AACVD 79
3.5 Results and Discussion 80
3.5.1 TGA analysis of Cobalt Precursors 80
3.5.2 Optical Properties of CoS thin films 87
3.5.3 Thickness measurements for CoS thin films 87
3.5.4 TGA analysis of Nickel Precursors 89
3.5.5. Optical Properties of NiS thin films 95
3.5.6 Thickness measurements of NiS thin films 96
3.5.7 TGA analysis for Manganese Precursors 97
3.5.8 Optical Properties of MnS thin films 101
3.5.9 Thickness measurements for MnS thin films 102
3.5.10 TGA analysis for Cadmium Precursors 103
3.5.11 Optical Properties of CdS thin films 109
3.5.12 Thickness measurements of CdS thin films 110
3.5.13 Conclusions 111
References 112

List of tables

Table 1.1	Application of semiconductor films in industry	31
Table 1.2	Methods for detecting and characterizing defects in crystalline and Amorphous CVD films	38
Table 2.1	Spectroscopic frequencies for the complexes [I-XII]	64
Table 2.2	Crystal data and detailed structure refinement for complexes $[NiCl_2(SC(NHC_6H_{11})_2)_2]$ (VI) and $[MnCl_2(CS(NH_2)_2)_4]$ (VII)	65
Table 2.3	Selected bond distances and bond angles for complex VI	66
Table 2.4	Selected bond distances and bond angles for complex $[MnCl_2(CS(NH_2)_2)_4]$ (VII)	70
Table 2.5	Hydrogen – geometry (Å) for complex $[MnCl_2(CS(NH_2)_2)_4]$ VII.	70
Table 3.1	XRD JCPDS data for cobalt sulphide.	82
Table 3.2	XRD JCPDS data for NiS and GaAs.	93
Table 3.3	XRD JCPDS data for MnS.	99
Table 3.4	The summary of all TGA data for complexes I- XII.	105
Table 3.5	XRD JCPDS data for CdS.	106

List of Abbreviations

Techniques and Methods

FT-IR	Fourier Transform Infrared Spectroscopy
UV-Vis	Ultraviolet visible spectroscopy
TGA	Thermogravimetric analysis
CVD	Chemical Vapour Deposition
AACVD	Aerosol Assisted Chemical Vapour Deposition
LP-MOCVD	Low Pressure Metalorganic Chemical Vapour Deposition
PECVD	Plasma Enhanced Chemical Vapour Deposition
FACVD	Flame Assisted Chemical Vapour Deposition
XRD	Powder X-Ray Diffraction
SEM	Scanning Electron Microscopy
Int.	Interferometer Method
EDAX	Energy dispersive X-ray analysis

Symbols and constants

V_m	Volume for depositing metal atom
P_s	Precursor partial pressure
α	Fraction of reactant molecules that react after striking a surface
K_b	Boltzmann's constant
T	Temperature
E_a	Electron Affinity
D_v	Diffusivity vapours
N_∞	Droplet concentration
f	Frequency
Å	Angstrom

List of figures

Figure 1.1	Schematic presentation of a band structure of the semiconductor	3
Figure 1.2	Excitation and electron transition across the band gap by proton absorption.	5
Figure 1.3	Schematic presentation of LP-MOCVD Apparatus.	10
Figure 1.4	Schematic presentations of FACVD Apparatus.	11
Figure 1.5	Schematic presentation of the PECVD apparatus.	13
Figure 1.6	Schematic presentations of the AACVD Apparatus.	20
Figure 1.7	Schematic presentation of the AACVD process.	21
Figure 1.8	Planar structure of the field SHF MOS transistor on gallium arsenide with a narrow approximated gate.	33
Figure 1.9	Structure of the monolithic integrated circuit that unites a waveguide and a photodetector by the use of a Schottsky barrier Platinum indium gallium- arsenide.	34
Figure 1.10	Stages for $GaAs_{1-x}$ red LED fabrication (x = 0.4).	35
Figure 1.11	X-ray diffractometer.	40
Figure 1.12	(a) Electron and photon signals emanating from tear-shaped interaction volume during electron beam impingement on specimen surface (b) Effect of surface topography on electron emission.	44
Figure 1.13	Schematic image of the Normaski differential interference contrast microscope with translating wedge for phase adjustment.	45
Figure 1.14	Schematic diagram of a surface relief measuring instrument (profilometer).	52
Figure 2.1	Reaction scheme for the synthesis of complexes.	62
Figure 2.2a	Molecular structure of complex, $[NiCl_2(SC(NHC_6H_{11})_2)_2]$, VI	68
Figure 2.2b	Packing diagram of complex, $[NiCl_2(SC(NHC_6H_{11})_2)_2]$, VI	69

Figure 2.3a	Molecular structure of complex, $[MnCl_2(CS(NH_2)_2)_4]$	71
Figure 2.3b	Packing diagram of complex, $[MnCl_2(CS(NH_2)_2)_4]$	72
Figure 3.1	Schematic presentation for the AACVD setup.	80
Figure 3.2	TGA graph of the cobalt complexes I, II, III.	81
Figure 3.3	XRD pattern for cobalt sulphide from precursor [I] exhibiting CoS_2 and Co_3S_4.	82
Figure 3.4	XRD pattern for cobalt sulphide from [II] exhibiting Co_3S_4.	83
Figure 3.5	SEM micrograph of CoS from [II] at (a) 400 °C (b) 300 °C showing the formation of granulated spheres.	84
Figure 3.6	SEM micrographs of cobalt sulphide from [II] at 450 °C (a) slow condensation of spheres (b) formation of small cubes (c) condensation of granular spheres (d) cobalt sulphide at 500 °C forming larger cubic particles.	85
Figure 3.7	SEM micrograph of CoS from [I] (a) showing small irregular shapes (b) less crystalline aggregates of irregular shapes.	86
Figure 3.8	Optical absorption of CoS at 400 °C and 450 °C.	87
Figure 3.9a	Surface morphology of CoS at 400 °C.	88
Figure 3.9b	Interference pattern of the CoS thin film deposited at 400 °C,	89
Figure 3.10	TGA graph of nickel complexes IV, V, VI	90
Figure 3.11	XRD pattern of NiS at 350 °C and 400 °C for $Ni_{3-x}S_2$ and NiS_2.	91
Figure 3.12	XRD pattern of NiS at 400 °C exhibiting NiS_2 and $NiS_{1.97}$.	92
Figure 3.13	XRD pattern of NiS deposited from GaAs.	92
Figure 3.14	SEM micrographs of NiS from [IV] (a) initial growth at 350 °C (b) pertrusion of rod-like structures (c) NiS at 400 °C	93
Figure 3.15	(a) Plain view of film grown from [IV] 400 °C showing the presence of spheres (b) granules forming cubes.	94
Figure 3.16	SEM micrographs (a) spheres and rod-like elements (b) heterogeneous uniform deposits of spheres.	95
Figure 3.17	Optical properties of NiS at • 400 °C • 450 °C and • 500 °C.	96
Figure 3.18	Surface morphology of NiS films (a) 400 °C and (b) 450 °C.	97

Figure 3.19 TGA curves of manganese complexes VII, VIII, IX 98
Figure 3.20 XRD pattern of MnS at 450 °C. 98
Figure 3.21 SEM micrographs of MnS deposited at 300 °C. 99
Figure 3.22 SEM micrographs of MnS deposited at (a) 400 °C (b) 450 °C. 100
Figure 3.23 EDAX spectrum illustrating the ratios of MnS. 100
Figure 3.24 Absorption spectrum of MnS thin film deposited at 350 °C. 101
Figure 3.25 Absorption spectrum of MnS thin film deposited at 400 °C. 102
Figure 3.26 Surface morphology of MnS film at 400 °C. 103
Figure 3.27 Interference patterns of MnS at 400 °C. 103
Figure 3.28 TGA graph of cadmium complexes X, XI and XII 104
Figure 3.29 XRD pattern of CdS thin film *ca* (250-450 °C). 106
Figure 3.30 SEM micrographs of CdS deposited at 250 °C. 107
Figure 3.31 SEM micrographs of CdS deposited at 300 °C. 107
Figure 3.32 SEM micrograph of CdS (a) CdS at 400 °C from [XII] (b) CdS at 400 °C from [XI]. 108
Figure 3.33 SEM micrograph of CdS deposited at 450 °C from [X]. 108
Figure 3.34 Absorption spectrum of CdS thin film (a) 400 °C (b) 450 °C. 109
Figure 3.35 Surface morphology of CdS thin film (a) 400 °C (b) 450 °C. 110
Figure 3.36 Interference pattern of CdS film (a) 400 °C (b) 450 °C. 110

Acknowledgements

First and certainly the most important source of my inspiration I would like to thank Jehovah Jireah who has been my provider, for granting me the strength and wisdom to be able to complete this study. I would also extend my utmost gratitude to my promoter Prof. Neerish Revaprasadu for his dedicative support throughout my work both financially and with regards to the necessary resources for the project. To my co-promoter Dr Justice Moloto of whom I am most grateful for his persuasive suggestions, tolerance in all my endeavours and positive attitude towards this project. My deepest appreciation goes to Prof. Paul O' Brien for allowing me to attain my results by offering me a research visit at the University of Manchester for my work to take shape.

I would like to thank Prof. Paul O' Brien group for the help and assistance during my stay. I would especially like to thank Sbusiso for his endless help and making my stay in Manchester very interesting and rewarding. I would like to thank Mohammed Afzaal for his signatures and contribution in my work. Mostly am indebted to Javeed for his tireless assistance with the instrumentation and being a friend. Thanks to Pui for her "magic" fume cupboard and workspace and Arunkumar for his time in showing me other techniques to try in my work. I would also like to thank the technical team both in Manchester and UKZN where all my results were obtained and Andrew Forrester, for Interferometer measurements. To the Royal Society for financing my work in Manchester and National Research Fund (NRF) for the duration of my study, I am most grateful.

My greatest acknowledgement goes to the Chemistry Department at the University of Zululand, the staff and the research team for their input and support throughout my work. Of course, special thanks go to my family and extended families for their endless love and support my siblings Nozipho, Thabi, Livie, Ntuthuko and Nonto for standing with me while attaining my goals. To my dear and amazing friends who have supported me in prayers and their assurance of support at all times, my appreciation is beyond words.

Dedication

I would like to dedicate this dissertation to my beloved Mother, Mrs A.N. Jila for her remarkable love and support and my late father, Mr M.G. Jila

CHAPTER I

GENERAL INTRODUCTION TO SEMICONDUCTOR THIN FILMS

1. GENERAL BACKGROUND

1.1 Theory of semiconductor thin films

One of the earliest reports on thin films was by Badeker[1], who prepared cadmium oxide (CdO) films by thermal oxidation of sputtered films of cadmium. These films were reported to be transparent as well as conductive. Thin films of metals such as Fe, Cu, Co, Mn, and Ag have also been found to have similar properties, but the films, in general, are not very stable and their properties change with time. Coatings based on semiconductor materials have a large number of applications because their stability and hardness are superior to those of thin metallic films. A semiconductor is a material that behaves in between a conductor and an insulator as shown in Figure 1.1, but less readily than a conductor. Semi-conductors can be divided into two types, intrinsic and extrinsic. Semiconductors that rely on temperature to conduct charge or emit light are called intrinsic semiconductors. The 'doped' semiconductors are called extrinsic semiconductors. They contain impurities incorporated into the crystal structure of the semiconductor.

At very low temperatures, pure intrinsic semiconductors behave like insulators. At higher temperatures though under light intrinsic semiconductors can become conductive. The addition of impurities to a pure semiconductor can also increase its conductivity. Dopants are introduced in order to enhance the conducting potential of a semiconductor. The quantity of the dopant is not the only factor that can limit the electrical properties of the semiconductor, the type of impurity is also particularly important. Those impurities can either be unintentional due to lack of control during the growth of the semiconductor thin film, or either be added deliberately to provide mobile current carriers in the semiconductor thin film.

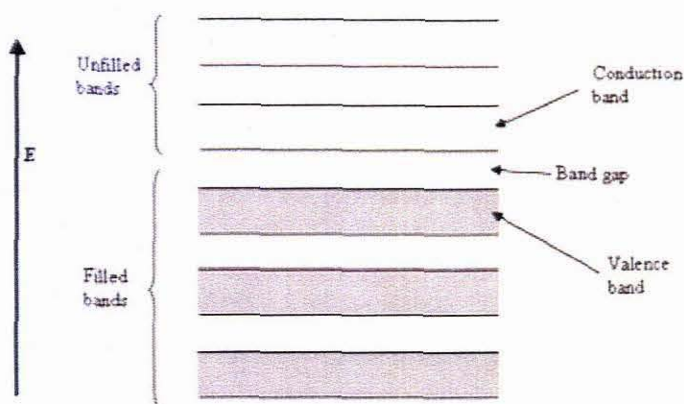

Figure 1.1 Schematic presentation of a band structure of the semiconductor.[2]

An overview of the electronic structure of semiconductors is necessary in understanding the origin of semiconductor thin films. The optical response of a semiconductor is critically controlled by its energy bandgap (E_g) which gives the threshold energy for an electronic transition from the valence band to the conduction band.[2]

Thin films with a large energy band-gap exhibit high electrical conductivity, high optical transmittance in the visible region and high reflectance in the IR region. These unique properties of the transparent conducting sulphide films make them suitable for a variety of applications. Thus the growth technique plays a significant role in governing the properties of these films, because the same material deposited by two different techniques usually has different physical properties. This is due to the fact that the electrical and optical properties of these films strongly depend on the structure, morphology and the nature of the impurities present. Moreover, the films grown by any particular technique may often have different properties due to the involvement of various deposition parameters. The properties, however, can be tailored by controlling the deposition parameters by different techniques. Although there are many techniques available for preparing semi-conducting thin films, it is generally difficult to maintain the stoichiometry of the materials.[3-5] It is, therefore, essential to make a detailed investigation of the relationship between the properties of these films and the method of deposition.

1.2 Direct and Indirect semiconductors

It is known that semiconductor materials undergo two types of optical transitions which are in accordance with the peculiarities of the energy band structures of semiconductor.

There are as follows :

1) The transitions with only one photon participation (direct transitions).
2) And the transitions in which side by side with photon absorption as a part of energy and momentum are called indirect transitions.

Selvan used equation (1) to show the association of the absorption coefficient and the photon energy of the direct transition.

$$\alpha (h\upsilon) = k (E_g - h\upsilon)^{1/2} \qquad (1)$$

(k is constant of proportionality; α is the absorption coefficient and E_g is the band gap energy, hυ the photon of energy)

The absorption coefficient for a photon of a given energy (hυ) is proportional to the probability (P_{if}), the density of states in the initial state (n_i) and the density of the final available states (n_f).

A review by O'Brien *et al.*[6] indicates that for all possible transitions between states separated by an energy difference equal to the energy of the incident photon these processes must be summed up by equation (2):

$$\alpha (h\upsilon) = \Sigma P_i f n_i n_f \qquad (2)$$

On the other hand, some forms of transitions are forbidden which are referred to as indirect transitions (Figure 1.2). These are in the semiconductors with small absorption coefficients and in which the lowest electronic transition between the valence band and

the conduction band is formally forbidden. In thin films the indirect transitions take place in the size-quantized films, whether in either phonon dislocation or surface roughness as a third body which have been studied previously by several researchers.

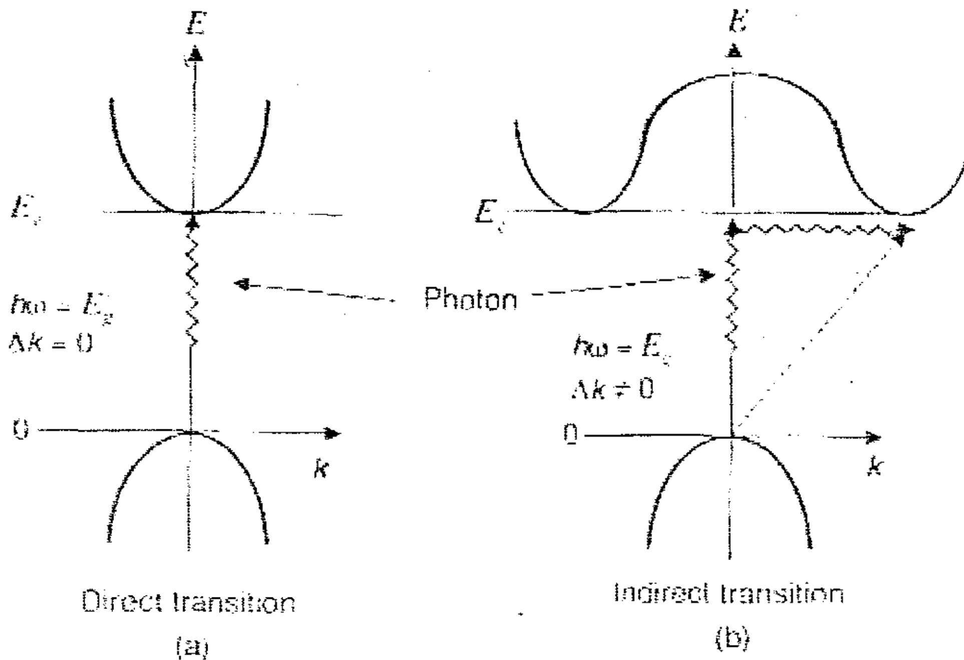

Figure 1.2 Excitation and electron transition across the band gap by photon absorption[6].

1.3 Background to Chemical Vapour Deposition (CVD)

Industrial exploitation of CVD could be traced back to the literature by de Lodyguine[9] in 1983 who deposited tungsten onto carbon lamp filaments through the reduction of WCl_6 by H_2. Around this period the CVD process was developed as an economically viable industrial process in the field of extraction and pyrometallurgy for the production of high purity refractory metals such as Ti, Ni, Zr and Ta. Chemical vapour process is one of the most important techniques for producing thin films of semiconductor materials. CVD has been the most commonly used technique for the fabrication of compound thin films. The fabrication of metallic thin films using CVD is a matter of interest, due to advantages arising, among others, from kinetically controlled deposition processes. It is also a

promising technique for the practical application of High Temperature Superconducting (HTS) films having special properties such as a high deposition rate, also the possibility of long time deposition, with no limitation of the shape and the scale[10]. The CVD techniques are based on homogenous or heterogeneous chemical reactions. Depending on conditions such as vapour pressure and temperature, both types of reaction or only one of them, takes place during the deposition process. These processes employ various gaseous, liquid and solid chemical substances as sources (precursors) of elements of which the film is to be formed. A large variety of single crystalline, polycrystalline and amorphous thin films of metals are formed.

1.3.1 Processes of Chemical Vapour Deposition

The technique involves a reaction of one or more gaseous reacting species on a solid surface (substrate). In this process, metallic sulphides or oxides are generally grown by the vaporization of a suitable organometallic compound. A vapour containing the condensate material is transported to a substrate surface, where it is decomposed, usually by a heterogeneous process. The nature of the decomposition process varies according to the composition of the volatile transporting species. The decomposition condition should be such that the reaction occurs only at or near the substrate surface and not in the gaseous phase, to avoid formation of powdery deposits which may result in haziness in the films.

The vapours of a volatile compound are carried by a carrier gas e.g. O_2, N_2, Ar, from a hot bubbler through a heated line to a reaction chamber to which oxygen/H_2O vapour is introduced. In this growth chamber the vapours decompose and the homogenous oxide/ sulfide films form at the preheated substrate surface. CVD can be performed in a 'closed' or 'open' system. In the 'closed' system, both reactants and products are recycled. This process is normally used where reversible chemical reactions can occur with a temperature difference. A closed system is of less importance nowadays since only a small fraction of CVD processes are performed in this system.

The quality of the films depends on various parameters such as substrate, temperature, gas flow rate, the precursor concentration and system geometry. In order to obtain the best quality films all these parameters have to be optimized and controlled. The substrate temperature and gas flow rate largely determines the deposition rate. If the substrate temperature is low, carbon occlusions are found in the films as a result of incomplete oxidation of the organic material. If the substrate temperature is too high, excessive diffusion of surface impurities during film growth can occur. In addition, radiations from the substrate heater may preheat the gas in the reaction chamber. Thus results in decomposition of organometallic compounds in the gas phase rather than at the substrate surface, thereby producing a powder-like deposit instead of a smooth film. The gas flow and system geometry determines the uniformity of the films deposited over large areas. Thus, it is of importance to introduce the gas into the reaction chamber in a controlled manner both in terms of gas inlet location and flow rate.

1.3.2 Process principles and deposition mechanism

In general, the CVD process involves the following key steps[11] :

(1) Generation of active gaseous reactant species.

(2) Transport of the gaseous species into the reaction chamber.

(3) Gaseous reactants undergo gas phase reactions forming intermediate species :

(a) At a high temperature above the decomposition temperatures of intermediate species inside the reactor, homogeneous gas phase reaction can occur where the intermediate species undergo subsequent decomposition and/or chemical reaction, forming powders and volatile by-products in the gas phase. The powder will be collected on the substrate surface and may act as crystallization centres, and the by-products are transported away from the deposition chamber. The deposited film may have poor adhesion.

(b) At temperatures below the dissociation of the intermediate phase, diffusion or convection of the intermediate species across the boundary layer (a thin layer close to the substrate surface) occurs. These intermediate species subsequently undergo steps (4)-(7).

(4) Absorption of gaseous reactants onto the heated substrate, and the heterogeneous reaction occurs at the gas-solid interface (i.e. heated substrate) which produces the deposit and by-product species.

(5) The deposits will diffuse along the heated substrate surface forming the crystallization centre and growth of the film.

(6) Gaseous by-products are removed from the boundary layer through diffusion or convection.

(7) The unreacted gaseous precursors and by-products will be transported away from the deposition chamber. For the deposition of dense films and coatings, the process conditions are tailored to favour the heterogeneous reaction. Whereas, a combination of heterogeneous and homogenous gas phase reaction is preferred for the deposition of porous coatings.

1.3.2.1 Advantages and disadvantages of CVD

Although CVD is a complex chemical system, it has the following distinctive advantages:

a) The capability of producing highly dense and pure materials.
b) Produces uniform films with good reproducibility and adhesion at reasonably high deposition rates.

The limitations of CVD are :

a) Chemical and safety hazards caused by the use of toxic, corrosive, flammable or explosive precursor's gases. However, these drawbacks have been minimized using variants of CVD such as Electrostatic Spray Assisted Vapour deposition (ESAVD) and Combustion Chemical Vapour deposition (CCVD).
b) Difficult to deposit multicomponent materials with well controlled stoichiometry using multi-source precursors because different precursors have different vaporization rates. However, this limitation can be overcome using single source chemical precursors.

1.4 Thin film CVD techniques

1.4.1 MOCVD (Metal-Organic Chemical Vapor Deposition)

Metal-organic chemical Vapour deposition (MOCVD) is a variant of CVD which has been classified according to the use of metal-organics as precursors. MOCVD can be used to deposit a wide range of materials in the form of amorphous, epitaxial and polycrystalline films. Some metal-organics precursors are commonly used to grow III-V and II-VI and IV-VI semiconducting materials, as well as metallic films, dielectric films, and other applications. The metalorganic or organometallic precursors generally undergo decomposition or pyrolysis reactions. At deposition temperatures below 500 °C, the reaction in the MOCVD process is kinetically limited. Whereas at a middle temperature range between 550 °C and 750 °C, the reaction is diffusion-rate limited.

MOCVD tend to involve endothermic reactions, thus cold-wall reactors with a single temperature zone can be used. The thermal environment for the decomposition and or deposition reaction of the precursors can be supplied using resistance heating, radio-frequency or infrared lamp heating. The MOCVD can be performed at atmospheric pressure and low-pressure (about 2.7-26.7 kPa) (Figure 1.3). For a typical MOCVD process, the deposition is entirely kinetically limited in a MOCVD process that is performed under ultrahigh vacuum (< 0.01 kPa) condition, such ultrahigh vacuum MOCVD is also known as "metalorganic molecular–beam epitaxy" or "chemical beam epitaxy". The common carrier gas and growth environment used during the deposition is hydrogen. Hydrogen is often used as the precursor carrier gas and growth environment for non-oxide films.

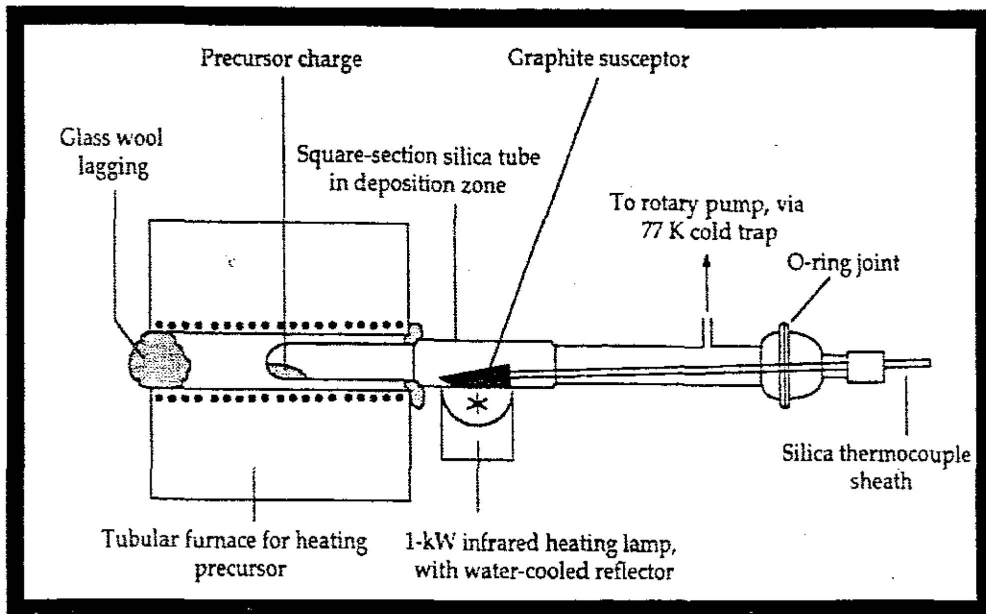

Figure 1.3: Schematic presentation of Low Pressure Metal Organic Chemical Vapour Deposition Apparatus

1.4.1.1 Limitations

Metalorganic precursors tend to be very expensive compared to halides, hydrides, and halohydrides and they are not widely available commercially for some coating systems. Therefore, they often need to be synthesized specifically for certain applications. The organometallic precursors are normally very reactive and hence they are difficult to purify. The growth of high quality semiconductor materials requires precursors with low oxygen content.

1.4.2 FACVD (Flame Assisted Chemical Vapor Deposition)

Flame Assisted chemical vapour deposition (FACVD) is another variant of CVD. This process involves the combustion of liquid or gaseous precursors injected or delivered into diffused/premixed flames where the liquid precursor will decompose or vaporize and undergo chemical reaction/combustion in the flame (Figure 1.4). The flame source and the combustion process provide the required thermal environment for vaporization, decomposition and chemical reaction. The flame source also helps to heat the substrate to enhance the diffusion and surface mobility of the absorbed atoms on the substrate surface during the deposition of films. The FACVD method can also be distinguished

from the thermal spraying method and its variants such as plasma spraying which involves the use of solid powders as starting materials and, the high energy thermal source such as hydrogen fuel/plasma to melt the solid precursor powder into a molten/ semi-molten state before being sprayed onto water cooled substrates to form the coatings with a splat–like structure that normally contains micropores.

The main process parameters that can be optimized in order to control the crystal structure, morphology and particle size are flame temperature and its distribution, choice of precursors and its residence time in the flame, ratio of precursor to fuel. Additives can also be introduced into the flame to alter the size phase and shape of the products.[13, 14]

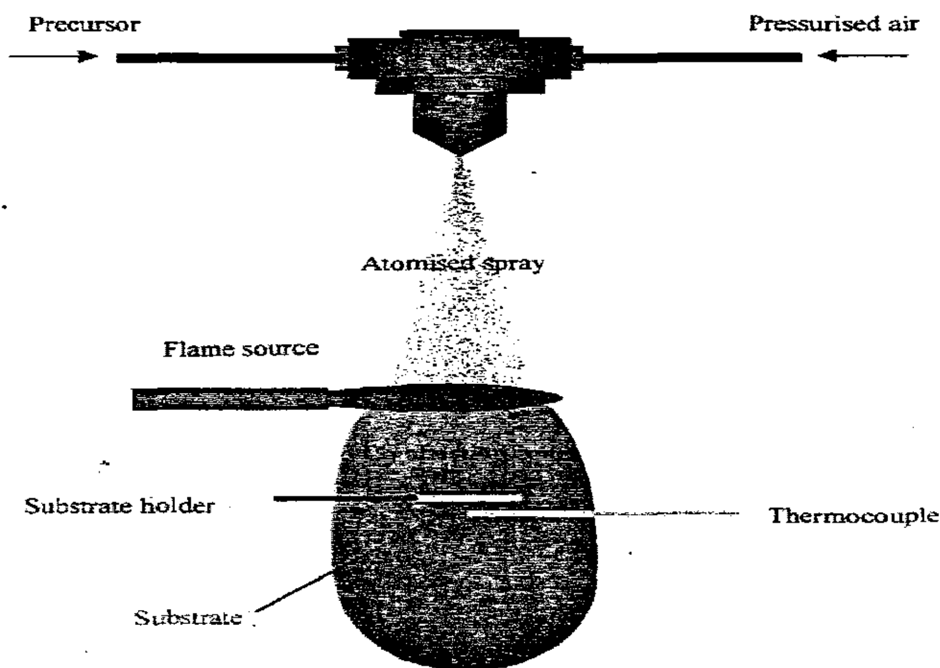

Figure 1.4: Schematic presentation of Flame Assisted Chemical Vapour Deposition Apparatus

1.4.2.1 Advantages of FACVD

The advantages of FACVD are that the high flame temperature allows:

I. the use of volatile as well as less volatile chemical precursors to form a chemical vapour. Therefore, it is a true CVD process and possesses the non-line-of-sight-capability for the deposition of coatings onto non planar substrates;
II. the formation of the reaction product in a single step without post-processing such as calcinations;
III. the rapid mixing of reactants on a molecular scale, thus reducing the processing time significantly and enable a better control of the stoichiometry of the multicomponent films as compared to conventional CVD and Physical Vapour deposition (PVD) methods;
IV. the vaporization, decomposition and chemical reactions to occur rapidly leading to a high deposition rate; and
V. the relatively low cost compared to the conventional CVD and PVD methods as the FACVD process can be performed in an open atmosphere for the deposition of oxide coatings without the need for a sophisticated reactor or vacuum system.

1.4.2.2 Limitations of FACVD

The major drawback of the FACVD method is the large temperature fluctuation of the flame source during deposition due to the large temperature gradient present in the flame. As a result of such limitations, the FACVD is not widely used for the deposition of uniform thin films or adherent thick films. However, it is more commonly used commercially for the production of micron or sub-micron size powders by tailoring the homogeneous gas phase reactions.

1.4.3 Plasma Electron Chemical Vapour Deposition (PECVD)

PECVD is also known as glow discharge CVD. It uses electron energy plasma as the activation method to enable deposition to occur at a low temperature and at a reasonable rate. Supplying electrical power at a sufficiently high voltage to a gas at reduced pressures (< 1.3 kPa), results in the breaking down of the gas and generates a glow

discharge plasma consisting of electrons, ions and electronically excited species. The vapour reactants are ionized and dissociated by electron impact, and hence generating chemically active ions and radicals that undergo the heterogeneous chemical reaction at or near the heated substrate surface and deposit the thin film (Figure 1.5). PECVD can be operated using either direct or remote modes.

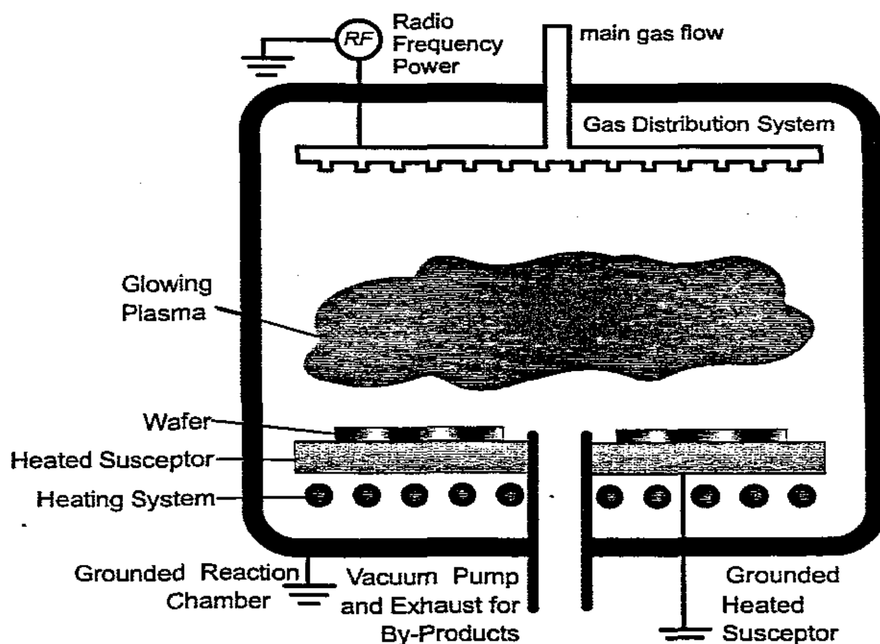

Figure 1.5: Schematic presentation of the Plasma Electron Chemical Vapour Deposition Apparatus

1.4.3.1 Limitations of PECVD

The major drawback of the PECVD technique is that it requires the vacuum to generate the plasma, and a more sophisticated reactor to contain the plasma.

Due to it being highly sophisticated it is rather too expensive to maintain and also when compared to the thermally activated APCVD system. Generally PECVD has difficulty in producing ultra high purity thin films, which is mostly due to the incomplete desorption of the by-product and unreacted precursor at low temperatures, especially hydrogen which remain incorporated into the films. This is can act as both limitation and an

advantage in both instances. As a limitation the impurities such as in refractory ceramics of carbides, nitrides, oxides and silicides, the impurities affect the stoichiometry of the deposited films and hence the physical, chemical, mechanical and electrical properties of the film.

1.4.3.2 Advantages of PECVD

Some of the impurities deposited may be most beneficial for example the incorporation of hydrogen in amorphous silicon provides improved optoelectronic properties and is advantageous for solar cell applications.

The main advantage of the PECVD is that deposition can occur at relatively large areas and, offers the flexibility for the microstructure of the film and deposition to be controlled separately. The deposition temperature of PECVD can be lowered further by the use of metalorganic precursors such as (MOPECVD). PECVD has the advantage to produce integrated multilayer structures with different physical properties.

1.4.4 AACVD (Aerosol assisted chemical vapor deposition)

In aerosol assisted chemical vapour deposition (AACVD), the aerosol can be generated by atomizing the chemical precursors into finely divided sub-micrometer liquid droplets (aerosol). The droplets are distributed throughout a gas medium using the ultrasonic aerosol generator, electrostatic aerosol generator or electrospraying method. The chemical precursor can be prepared by dissolving solid or liquid starting chemicals into a solvent (normally an organic solvent with a high boiling point) or a mixture of solvents to assist the vaporization of the chemicals and provide additional thermal energy for the dissociation or decomposition of the chemicals. The generated aerosol will be delivered into a heated zone, where the solvent is rapidly evaporated or combusted, and the intimately mixed chemical precursors undergo subsequent decomposition and/or chemical reaction near or on a heated substrate to deposit the desired film.

1.4.4.1 Principles and Characteristics of AACVD

The starting solution can be a pure liquid, single source precursor or a mixture of several liquid chemicals, or can be prepared by dissolving solid or liquid starting materials in a solvent. Generally, a criterion for the selection of solvents for atomization is high solubility of the precursor, low vapour pressure, and low viscosity.[15]

The atomization of the starting precursor solution can be carried out using various types of aerosol generators. Carrier gases are used to assist the generation of aerosol and transport of the aerosol to the reaction zone. Argon and nitrogen are the most common inert carrier gases, while compressed air is used for the deposition of oxide products. Reactive gases such as H_2 may also be introduced at this stage with other primary carrier gases, to aid the subsequent CVD reaction.[16]

After atomization, the precursor aerosol is transported to the heated zone, where evaporation of solvent and vaporization of precursor takes place prior to the major chemical reactions. For pure precursor, the vaporization can occur directly from the aerosol droplets. As the vaporization of precursor is the key feature of AACVD, differing from other aerosol processes for material synthesis, the selection of the starting precursor and the control of processing parameters are very important to ensure a true CVD process. If the aerosol droplets reach the heated substrates before complete vaporization, a spray pyrolysis process will take place rather than a true CVD mechanism.

In the heterogenous reaction: Preliminary decomposition of vaporized precursor may occur in the gas phase. The vaporized precursors and their gaseous intermediate species can be adsorbed onto the surface of the heated substrates, where they undergo substantial decomposition and chemical reactions, and yield the desired materials. External reactive gases can also be introduced into the reaction zone directly to assist the chemical reactions. This mechanism is similar to the heterogeneous CVD deposition process, which tends to produce high-quality films with good adhesive strength.

In the homogenous reaction: If the deposition temperature is too high, the major decomposition and/or chemical reactions may occur much earlier in the vapour phase, leading to homogenous nucleation and the formation of fine particles. External reactive gases can also be introduced to the homogenous reaction. If these fine particles are adsorbed on to the substrate, the subsequent heterogeneous reaction will lead to the formation of porous films. Alternatively, powders can be collected from the gas phase, with the size ranging from the nanometer to micrometer scales, depending on the processing conditions.

The chemical precursor as seen from Figure 1.7, in an AACVD process, must be in the form of chemical vapour that undergoes homogenous and heterogeneous chemical reactions. This description narrows down various aerosol-based deposition techniques which have been reviewed with reference to a few true CVD processes.[17] Actually, some spray pyrolysis processes can also be classified as "AACVD-like" processes,[18] as long a they use chemical precursors with low boiling points and high deposition temperatures.

Thus, because of the relatively low cost of the equipment, precursor chemicals, and processing, high quality materials can be potentially produced on a large scale by the AACVD method. Since it involves atomization, vaporization, and vaporization of solvent and precursor, the deposition mechanism of AACVD is more complicated, compared to that of conventional CVD. The theory of standard CVD has been well developed, and numerous models of varying complexity are available.[19] Conversely, there is no full model developed to describe the AACVD-based processes. In an AACVD process, residue and contamination may remain in the form of particles in the gas phase after solvent evaporation because of the limited purity of available solvents and reactants. Sometimes, precursors can react in solution to form involatile intermediate particles. The presence of solid particles in the gas phase strongly impacts deposition rates and morphology of the deposits and often leads to degradation of microstructures and properties of the products. Thus to avoid the formation of undesirable particles, it is useful to understand the processing features in AACVD.

Atomization of the Precursor: The Liquid chemical precursor or the precursor solutions are atomized to aerosol droplets prior to being delivered to the reaction zone. The atomization of precursor is the key processing feature of the AACVD process. There are 3 major aerosol generation methods used for AACVD;[15,16,18,20] Ultrasonic aerosol generations, pneumatic aerosol jet and, electrostatic atomization. They have different aerosol formation mechanisms and produce precursor droplets with different sizes and size distributions at different generation rates. Controllable droplet size, narrow size distribution and large aerosol output are requirements to optimize AACVD-based processes. A robust and precise atomization device has yet to be developed.

1.4.4.2 Ultrasonic Aerosol Generation

Ultrasonic Aerosol Generation is the most common method for the AACVD process. An ultrasonic aerosol generation has a piezoelectric transducer placed underneath the precursor. When a high-frequency electric field is applied, the transducer vibrates and instigates the formation of fine droplets.[16] The diameter d of the droplets can be described using equation 1[21]

$$d = k\left(\frac{2\pi y}{f^2}\right)^{2/3} \qquad (1)$$

f is the excitation frequency of the transducer, k is a constant, and ρ and γ are the density and surface tension of the liquid, respectively. Equation 1 suggests that when the physical characteristics of a precursor liquid are known, the diameter of the aerosol droplets is only an inverse function of the ultrasonic frequency f. A higher ultrasonic frequency will be needed to obtain a finer droplet that is because finer droplets can facilitate the vaporization of the precursor and the occurrence of the true vaporization, which is desirable for the deposition of high quality products by AACVD. The droplet size is not affected by the power setting of the transducer, while the amount of aerosol produced can be varied by altering the transducer power and the flow rate of carrier gases. Ultrasonic generation offers advantages in terms of providing a suitable droplet size for AACVD process.[22-24] The atomized droplet sizes are mainly in the range 1-10

μm. Further, finer and uniform droplets are always important for the precise control of processing and synthesis of better quality CVD products.

1.4.4.3 Evaporation of Aerosol Droplets

The atomized precursor droplets are transported to a heated zone where the evaporation of the solvent and vaporization of the precursor occur. During the evaporation/ vaporization of a neutral droplet, the diameter of the droplet, d, changes with time, t, as described in equation 2.[25]

$$d^2 = d_0^2 - 8t\,\frac{C_A D}{C_p}\left[\ln\frac{1-x_{A\infty}}{1-x_{As}}\right] \qquad (2)$$

d_o is the original droplet diameter at time t = 0, C_A is the molar concentration of species A in the vapour phase, C_p is the molar concentration of species A in the liquid phase, D is the binary diffusivity of vapour A in gas B, and x_{AS} and $x_{A\infty}$ are the l mole fractions of species A at the droplet surface and far from the droplet, respectively.

The condition for complete evaporation can be estimated by considering the time required for evaporation of droplets and comparing it with the appropriate residence time in a deposition system.[18] The characteristic time, τ_{sat}, for an evaporation process of droplets is given by eqn (3).

$$\tau_{sat} = \left(\frac{1}{2\pi d\, D_V N_\infty}\right) \qquad (3)$$

τ_{sat} is the characteristic time to saturate gas with vapour from evaporating droplets, D_v is the diffusivity of the vapour, and N_∞ is the droplet concentration (number per volume). Eqn 3 shows that the time required to saturate the gas is influenced by the droplet concentration and size. Larger droplets and higher droplet concentration leads to a shorter characteristic time. Hence, it is important to generate smaller aerosol droplets in

the atomization step. For a charged aerosol droplet, when evaporation occurs, the electric charge density on the droplet surface increases with the shrinking of the droplet, until the so called Raleigh limits reached at which point the repulsion of electric charges overcomes the surface tension cohesive force, ultimately leading to the disintegration of the droplet into finer fragments.[26] The instability that results from exceeding the Raleigh limit tears the droplet apart, produces smaller droplets that also evaporates. This sequence of events is repeated until evaporation of precursor droplets can be enhanced significantly by an electric charge.[27]

1.4.4.4 Adsorption of solution constituents onto substrate

Deposition or adsorption of the prepared metal sulphide to the substrate is the most important aspect of the aerosol deposition process as it is the major determinant of the experiments success. Considering this factor the parameters or shortcomings of a deposition process need to be monitored so as reduce non-reproducibility of the desired material. According to Frenkel theory of adsorption the inability of minimum deposition or adsorption to take place is due, to the failure of the impinging atoms to condense on a surface whose temperature is may be hundred degrees below the boiling point of the metal indicating that the atoms cannot be adsorbed by the substrate surface immediately on arrival. The reason for this may be the presence of an adsorbed gas layer on the surface, which prevents the condensing atom from coming within reach of the true surface forces of the substrate. Frenkel postulated that the atoms are free to move over the surface on arrival and do so for certain mean free time τ after which they evaporate. They may, however, collide with other metal atoms while on the surface, and so form pairs. The mean free time of such pairs is shown to be greater than that of a single atom, so that with the formation of pairs the chance of further collisions increases and the building up of nuclei and hence of a thick film is facilitated.

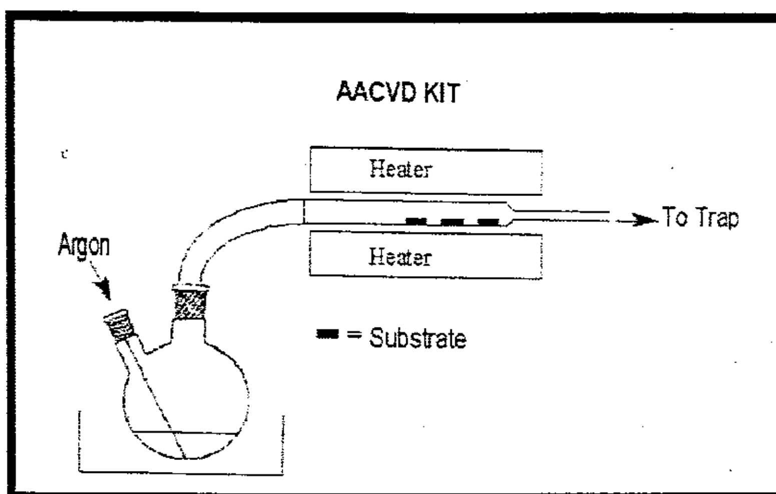

Figure 1.6 Schematic presentation of the Aerosol Assisted Chemical Vapour Deposition Apparatus

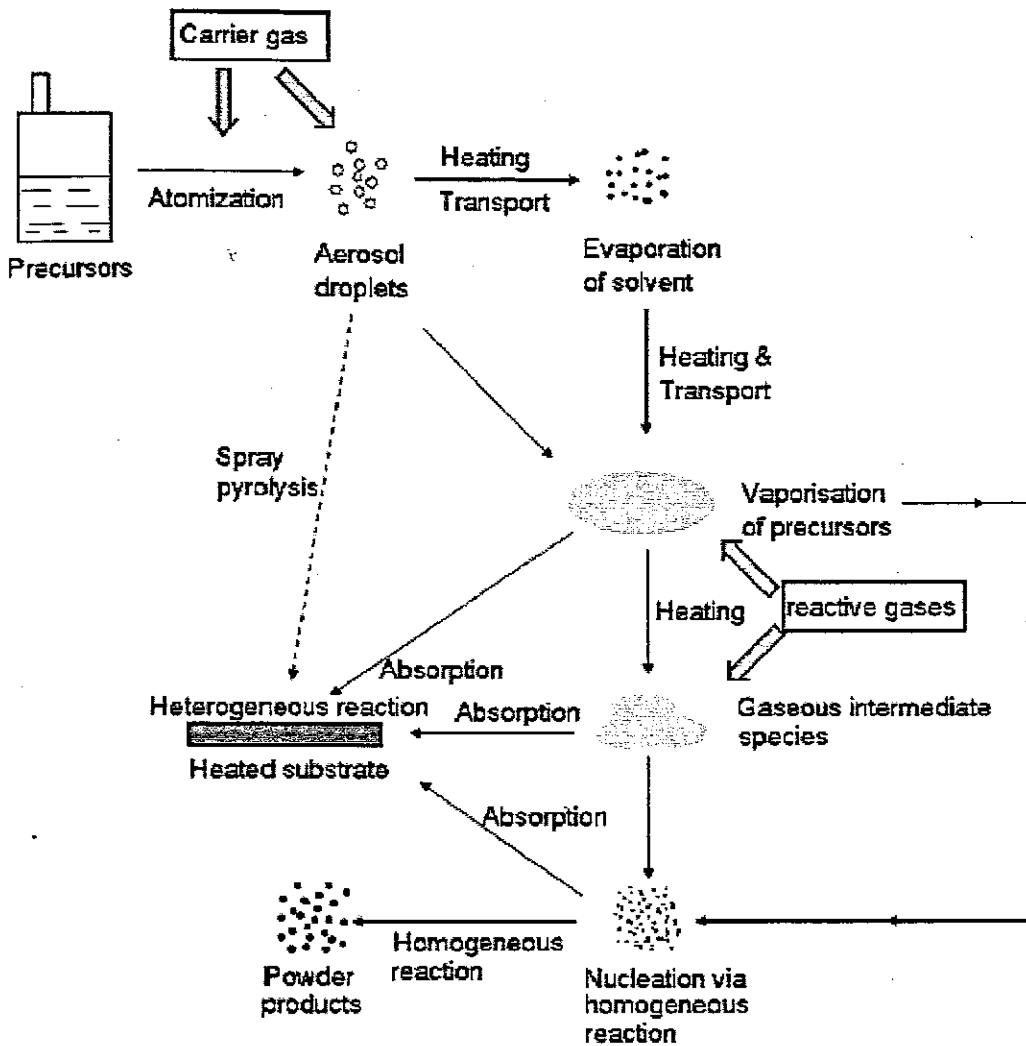

Figure 1.7 Schematic presentation of the AACVD process for deposition of films

1.4.4.5 Advantages of AACVD

a) It simplifies the vapour precursor generation and delivery method as compared to the conventional CVD method which uses a bubbler/vaporizer method, and hence, lowers the cost of the deposition process;

b) It tends to use single source precursors which provide good molecular mixing of chemical precursors which enables the synthesis of multi-component materials with well controlled stoichiometry;

c) It allows rapid formation of the deposited phases at relatively low temperatures due to the small diffusion distances between reactant and intermediates; and

d) It is relatively low cost process as compared to conventional CVD because the AACVD process can be performed in an open atmosphere for the deposition of oxide and some less oxygen sensitive non-oxide materials without the need of any sophisticated reactor and/or vacuum system.

1.5 The rate of deposition on film growth

Fundamentally the rate of deposition is greatly influenced by the reactor design or reactor operating conditions. Thus it is important to understand the CVD reactors to interpret rate measurements which are obtained with every new precursor. A variety of measurements are typically made when studying new precursors for deposition purposes, but one of the simplest measurement is the dependence of the deposition rate on the substrate temperature although this measurement is often not made.

The temperature dependence of the deposition rate can reflect the kinetics of the surface reactions (but only under the surface-reaction-limited deposition). A somewhat more sophisticated measurement is the dependence of the rate on the reactant pressure. Insight into the surface reaction mechanisms may allow synthesis of new precursors or modification of operating conditions to provide new reaction pathway for increased deposition rates. For conventional precursor delivery, the deposition process involves a series of three steps; a) introduction of precursor vapour, b) transport of precursor to the surface substrate and, c) surface reaction of the precursor. Since these steps are in series, the slowest step will limit the overall rate of deposition.

The maximum deposition rate can be given by a simple expression from gas kinetic theory. In equation 4, rate (cm/s) is the deposition rate, α (dimensionless) the fraction of reactant molecules that react after striking the surface, P_s [dynes (cm^2)] the precursor partial pressure immediately above the surface, V_m (cm^3) the volume of depositing metal atom, M_r(g) the molecular mass of precursor, k_b Boltzmann's constant [1.38 x 10^{-16} erg/(molecule K)], T (K) the temperature of gas above the substrate, a_o (dimensionless) a constant, E_a (erg/mol) the activation energy, and R [erg/(mol K)] the gas constant.

$$\text{Rate} = \frac{\alpha P_s V_m}{2\pi M_r K_b T} = \frac{\alpha_o P_s V_m \exp[-E_A/(RT)]}{2\pi M_r K_b T} \qquad (4)$$

The parameter α takes into account the details of the adsorption-desorption reaction phenomena and depends exponentially on temperature. The maximum value of α is 1 and is achieved when every collision results in reaction. This equation predicts that approximately 1 monolayer (roughly 1 Å of metal) can be deposited every second at 10^{-6} torr if α = 1. At 10^{-2} torr, 10 000 monolayers per second can be deposited. In most cases, α << 1, and the actual deposition rate is much lower than the values mentioned above. The parameter α is also important because values of α near unity result in poor conformal deposition.

The value of α can be controlled through precursor design. At a given temperature precursors with lower decomposition temperatures will have higher values of α. Therefore conformality can be improved by using precursors that are more thermally inert but at the expense of lowering the deposition rate.

1.6 Difference between dual source and single source precursor

In CVD the precursor chemicals are those that make up the desired film and in which are first vaporized. These are then carried to the chamber in which the coating will be applied by an inert carrier gas such as nitrogen. If a single source precursor is used the

process is called single source CVD. In this case the precursor molecule must have a molecular 'Achilles heel' that decomposes on heating to make it adhere to the substrate surface.

If two reactant precursors are used then the process is known as dual source CVD. In this case the precursors are mixed just before entering the deposition chamber and the heat of the chamber encourages a gas phase bimolecular reaction. Both single and dual source CVD can produce uniform coatings that adhere to match the contours of the substrate. Most recently thin films that are made from single source precursor are increasingly becoming more stable, uniform and of high quality than the dual source precursors.

1.7 Literature review on the use of single source precursor methods for CVD

Single source precursors have been used to synthesize metal sulphide thin films, because they possess one advantage of forming a one-step synthesis and are compatible with established chemical vapour deposition methods.[28] Dithiocarbamates are used to stabilize a wide range of oxidation states of different metal ions.[29] A large number of compounds are known CS_2 binds in η^3-coordination modes.[30-32] Nowadays Copper (II) dithiocarbamate is successfully used as single source precursor for the growth of semiconducting copper sulphide thin films.[33] There are relatively few reports on the deposition of nickel sulphide thin films from single source precursors by CVD. Cheon *et al.*[34] has reported deposition of the ratio of NiS from both a thermal and photochemical CVD routes using $Ni(S_2COCHMe_2)_2$ and Namura and Hayata studied the deposition of $NiS_{1.03}$ from $Ni(S_2CNEt_2)_2$ on Si (III) at 350-400 °C by low-pressure metal-organic chemical vapour deposition (LP-MOCVD). More recently, thin films have been grown using single-source precursors by metal-organic chemical vapour deposition (MOCVD).

Single source precursors play a very important role in controlling the deposition of thin films. Their favorable possibility relies on controlling film properties by the use of suitable synthetic approaches starting from a single source molecule (SSMP) precursor,

with core architecture very similar to the building blocks of the desired material.[35] The advantages of SSM/SSP with respect to multiple source reagents include an easier control of the stoichiometry and a limitation of unwanted side reactions. Research on single source precursors, have been very active and there are examples of this approach in semiconductor thin film materials. The single source approach means that all the elements that are required in the film have been incorporated into one compound and this is then utilized as a precursor. Research has been aimed on single source precursors with approaches on thin films of semiconducting and conducting materials.[36]

$Co(SiCl_3)(CO_4)$ has also been employed as a new single source precursor for the deposition of three different silicides Co_2Si, CoSi and $CoSi_2$ using MOCVD. The earliest works on the growth of thin films of 12-16 materials, using single source precursor; relate to CdS grown by spray pyrolysis of aqueous mixtures of cadmium chloride and thiourea, $SC(NH_2)_2$ whereby the single molecule precursor forms when reacting the parent compound directly in the sprayed solution. The formation of intermediate complexes $Cd[SC(NH_2)_2]_2Cl_2$.[37-39], $Cd[SC(NH_2)_2]Cl_2$[39]; $Cd(H_2O)[SC(NH_2)_2]Cl_2$[38], was claimed, which depended on the pH, the initial $CdCl_2/SC(NH_2)_2$ molar ratio, and on whether anhydrous or hydrated cadmium chloride was used. Niinisto *et. al.*[41] has confirmed the formation of $Cd[SC(NH_2)_2]$, a tetrahedrally coordinated cadmium complex[42] with quite complex thermal behavior in air and under the conditions of spray pyrolysis[43] a single source precursor.

Namura *et al.*[37] have reported both the use of copper bis (diethyl dithiocarbamate) and the more complex dialkylindiumisopropylthioatocopper (II) dialkyl dithiocarbamate. Bismuth compounds with xanthate derivatives have also been investigated when making single source precursors. The utility of bismuth tris (O-alkyldithiocarbonate), i.e., Bi $(S_2COR)_3$, more commonly known as bismuth xanthate, as single source precursor in the chemical vapor deposition of bismuth sulfide nanomaterials has been investigated. Xanthates ligands are known to coordinate metal monodentate, bidentate, bridging etc. giving rise to a rich diversity in their structural motifs.[44] Another major interest at the moment is in the development of single source precursors of metal chalcogenides.[45-47]

Suitable single-source precursors for MS (M = Zn or Cd) would contain direct metal-sulphur bonds.

However, relatively little use has been made of thioureas in the formation of single-source precursors and their thin films. Thus it was decided to investigate the synthesis of novel molecular precursors based on thioureas and to study their potential for the production of MnS, CoS, NiS, CdS and thin films.

1.8 Properties of MnS, CoS, NiS and CdS yielding feasibility for thin film deposition

1.8.1 Manganese sulphide

The monosulphide MnS, the disulphide $Mn^{II}S_2$, and possibly the trisulphide MnS_3, exist. In general the structures and phase relations of the Mn-S system are similar to the zinc and cadmium sulphide at elevated pressures and this is probably a consequence of the spherical symmetry of the high spin d^5Mn^{2+} ion which is present in MnS and MnS_2. Manganese(II) sulphide, MnS exists in three forms.[48] The stable green form (alabandite), designated α-MnS which has a rock-salt structure with octahedrally coordinated Mn^{2+} and S^{2-} ions. The red forms, designated β-MnS and γ-MnS, have the cubic zinc blend and the hexagonal wurtzite structures respectively in which the M^{2+} and S^{2-} ions are tetrahedrally coordinated. All three forms can be prepared by precipitation with H_2S gas from aqueous manganese (II) solutions[49, 50], but only α-MnS can be obtained by direct reaction between the elements.[50] MnS belongs to VII-VI compound semiconductor materials. MnS is such a material which exhibits an interesting combination of magnetism and semiconductivity[51] and with a band gap energy, (E_g = 3.1 eV), having potential use in solar cell applications as a window/buffer material. The cubic α-phase of MnS appears to be stable above room temperature, but when they turned to α-phase of MnS, they can be prepared at low temperature, but they are turned to α-phase above 200 °C.

The electronic spectra of the three forms of MnS have been studied in detail as have the electronic spectra of Mn^{2+} in ZnS and e.s.r spectra of Mn^{2+} in diamagnetic sulphide. All these studies suggest that there is considerable mixing of the manganese 3d orbitals with sulphide orbitals. MnS and MnS_2 are both semiconductors. The magnetic properties of MnS_2 and of the three forms of MnS have been studied in detail. They become antiferromagnetic at low temperatures and the crystallographic symmetry is lowered below the Neel point.[48, 52]

Mass spectrometric studies on stoichiometric MnS and a mixture of MnS and graphite show that the former vapourizes congruently to give Mn(g) and CS(g). Small quantities of MnS^+, MnS_2^+ and MnS_3^+ are observed[53] and from these measurements a value of 67 ± 6 kcal $mole^{-1}$ has been determined for the heat of formation of MnS gas. The dissociation of MnS gas is 71 ± 4 kcal $mole.^{-1}$

1.8.2 Cobalt sulphide

The black precipitate (so-called α-CoS) obtained from cobalt (II) solutions by treatment with sodium sulphide has the composition $Co(SH, OH)_2$, the hydroxide content depending upon the alkalinity of the precipitation medium. When freshly precipitated, this composition is soluble in acids, but upon standing, this amorphous precipitate changes to a mixture containing crystalline. $Co_{1-x}S$ and Co_9S_8 which is insoluble in dilute acids. In the cobalt-sulphur system sulphides identified are CoS_2 (with the pyrites structure), Co_3S_4 (with the NiAs structure). Cobalt disulphide is ferromagnetic below 120 K; above this temperature the paramagnetism is that of the low spin configuration $t_{2g}6e_g$. The phase Co_3S_4 (which occurs naturally as linnaeite) is stable up to about 650 °C; thereafter CoS_2 and $Co_{1-x}S$ are formed. It is readily prepared by the action of hydrogen sulphide on cobalt powder at 400 °C. The phase Co_9S_8 is peritectically formed around 835 °C its structure is remarkable in that eight of the cobalt atoms occupy tetrahedral holes in a cubic close packing of sulphur while the ninth cobalt atom is in an octahedral environment.

Cobalt Sulphide belongs to VIII-VI compound semiconductor materials. Films obtained from CoS are black in colour. Cobalt sulphide (CoS) is a semiconductor with band gap energy equal to 0.9 eV, however, Co_3S_4 has optical band gap of about 0.78 eV. Electrical resistivity of CoS is of the order 10^4-10^6 Ω.cm. Cobalt Sulphide has potential applications in solar selective coatings, IR detectors and as a storage electrode in photoelectro-chemical storage device.[24]

1.8.3 Nickel sulphide

Nickel sulphide belongs to VIII-VI compound semiconductor materials. It has hexagonal crystal structure. The films are black in colour. The optical band gap is 0.35-0.8eV and it confers potential for use as a thermo photovoltaic converter[38] resistivity is of the order of 10-10^4 Ω.cm. Nickel sulphide films have a number of applications in various devices such as solar selective coatings, solar cells, photoconductors, sensors, IR detectors, as electrode in photoelectrochemical storage device. Nickel sulphide has been studied because of it's potential as a transformation toughening agent for materials used in semiconductor applications.[41] Its use as catalysts and coatings for photo galvanic cells have also been reported.[42] The existence of various compositions of nickel sulphide includes: $Ni_{3+x}S_2$, Ni_4S_{3+} x, Ni_6S_5, Ni_7S_6, Ni_9S_8 NiS, Ni_3S_4 and NiS_2 makes such studies both interesting and challenging. Nickel sulphide thin films has been prepared using chemical vapour deposition, chemical bath deposition, and electrodeposition.[43] Particles of nickel sulphide have been synthesized by solid-state reactions[44] and precipitation from aqueous[45] and organic solutions.[46]

1.8.4 Cadmium sulphide

Cadmium sulphide belongs to II-VI compound semiconductor materials. Cadmium sulphide exists as a mixed phase (wurtzite and zinc-blend). The optical band gap energy varies from 2.17 to 2.24 eV. The electrical resistivity of the CdS is in the order of 10^5 Ω.cm with η-type electrical conductivity and is often used in opto-electronic devices. Especially, in case of chalcopyrite heterojunction solar cells, it acts as a buffer layer. In the conventional absorber-window configuration of thin film heterojunction solar cells, n-CdS window have paired with p-Cu_2S, p-CdTe and p-$CuInSe_2$ absorber layers to result in

efficient solar cells. Also, cadmium sulphide is a promising semiconducting material in the conversion of solar energy into electrical energy by means of photoelectrochemical process. Cadmium sulphide (CdS) has been employed in high efficiency solar cells formed with Cu_2S[34] and CdTe.[35] The CdS are also used as photoconductors, photo-resistors and transistor image magnification and recently in light activated valves for large screen liquid crystal display. The thin films are dense, smooth and homogenous without visible pores. Manganese doped cadmium sulphide (CdS: Mn) thin films are the potential candidates in thin films photovoltaic devices as window/buffer material.

1.9 Precursors of semiconductor thin films

A great concern when it comes to CVD processes is a choice of precursor used, as it is a determinant of the materials that are to be deposited. The use of thin films of various inorganic materials in the electronics industry has recently driven interest in chemical vapour deposition CVD, in which a layer of material is deposited through reaction of vapour phase precursor at the substrate surface[54]. The use of single source precursors (SSP) has been employed in preparing precursors which are suitable for deposition of semiconductor thin films. SSP simply means that there is an incorporation of all the elements required for the synthesis into one compound, which is utilized as a precursor. Amongst many advantages of using SSP especially when depositing films via the AACVD or LP-MOCVD technique is the presence of only one molecule in the supply stream which reduces the likelihood and the extent of pre-reaction and the associated contamination of the q film permitting greater control of film stoichiometry. Despite the numerous potential advantages of SSPs, these materials come with their shortcomings. The high molecular weights tend to lead to lower volatility, which can be problematic in conventional atmospheric pressure CVD. This problem is exacerbated in systems requiring two/more metals, since the presence of additional metals would drive the molecular weight up. However, this problem can be overcome by using a low-pressure environment or by employing a solution of the precursor, e.g. in AACVD/liquid injection

CVD. A further problem associated with single-source precursors is the difficulty in depositing materials with non-integral stoichiometries or where dopants are required.

Thus the common precursors used in the CVD process are metals, metal hydrides, halides, halohydrides and metallorganic compounds. While in general metal halides and halohydrides are more stable than corresponding hydrides, early efforts in the area of precursor design focused on vapour pressure as the primary consideration.[56,57] Therefore the use of CVD reactors that volatilize liquid precursors by passing the carrier gas through a bubbler containing the complex e.g. AACVD technique became very popular. Sublimation of solid precursors can also be used for volatilization, however, in these techniques vapour pressure is still the determinant of whether sufficient precursor flux for film growth can be generated. As a result the development of aerosol assisted CVD (AACVD)[58,59] and related techniques such as liquid injection CVD[55], in which precursor solutions are dispersed from solution before transport to the substrate, has broadened the range of precursor candidates because these methods have less stringent volatility restrictions and thermally sensitive complexes.

1.10 Applications of Semiconductor Thin Films

1.10.1 Semiconductor films for microelectronics

The available forecasts for the development of microelectronics are supported by the relationship between materials and methods, whereby silicon plays an important role. The possibilities of using other semiconductor materials are underestimated, along with this germanium is successfully used in bipolar SHF-transistors amplifying devices with cooling down to cryogenic temperatures and in radiation detectors.

Gallium Arsenide and other III-V compounds permit production of radiating diodes and lasers, SHF oscillators, amplifiers and connections between microelectronic and optoelectronic devices that attracts the attention of many researchers. The use of semiconductor films in industry is shown in Table 1.1.

The latest development of microelectronics is characterised by a further increase of the packing density of active elements in a crystal up to 10^6-10^7 and an increase of fast response of microschemes up to 10^9-10^{10} actions per second. The improvement of silicon epitaxial technology, the use of electron lithography, ion-beam etching, ion doping and laser annealing has permitted realisation of very large integrated of microprocessors (in the 4th generation of computers) producing single crystal computers that are not inferior, in fast response and memory volume, to large computers of the 3rd generation.

On the other hand, the production of effective microelectronic circuits on germanium, gallium arsenide and other semiconductors is connected with the problem of obtaining thin homogenous single-crystal films of those materials as well as the preparation of dielectrics for masking and protecting them with perfect boundary formation. The methods developed to increase the response of schemes at the transition to MIS transistors using short channels, the technology of ion doping, insulating substrates (sapphire or spinel) and the method of signal transfer with bound charges (CCD) may be realised with new materials.

Table 1.1: Application of semiconductor films in industry

Type of films	Semiconductor	Recognisable application	Deduced Application
Homoepitaxial	Si	Integrated circuits & discrete devices	
	Ge	Discrete high-frequency transistors	
	GaAs	Devices on Gunn effect, Schottky diodes	
Heteroepitaxial	GaAlAs and	Light diodes	Intergrated circuits

	GaPAS on GaAs Si on sapphire		
Polycrystalline	Sb_2S_3PbO	Television camera picture tubes	Thin film transistors on II-VI compounds
	$CdS-Cu_2S$, Si	Solar batteries on elastic substrates	
	CdS(Cu) CdSe(Cu)	Photoresistors	Electroluminescent films, image amplifiers, piezoelectric devices
	III-V compounds	Galvanomagnetic devices	Photocathodes, thin film transistors
	SnO_2	Transparent electrodes	
	Si	MOS transistors with self-matched shutter	
	Pb-chalcogenides		
	Pb-Sn- Te, Cd, Hg-Te	IR-receivers	

At present the production problem of photolithography on MIS field-effect transistors (MISFET), using gallium arsenide, has been successfully resolved. In SHF circuits for satellite communication in the ranges of 6 and 12 GHz, these transistors are more effective than silicon devices; a lower noise level makes their use more reasonable at frequencies up to 4 GHz. Gallium arsenide is most successfully used in microwave devices of Japanese films. In MISFETS made by Nippon Electric, the gate width is 0.5 μm and noise does not exceed 4 dB at 14 GHz or 3 dB at 8 GHz.[60] The design peculiarities of transistors on silicon (a narrow approximated gate) fig.1 and high mobility of charge carriers in GaAs films are used in GaAs devices.

Monolithic integrated circuits combining micro- and opto-electronic devices are produced on the basis of multilayer structures including GaAs and solid solutions of the III-V type. Figure 1.8 shows the IC structure comprising of a passive planar waveguide that operates due to the difference in refractive indices n and n^+ of gallium arsenide, a photodetector and on amplifier on the Schottky barrier Pt-InGaAS. Ohmic contacts are made by good spraying.[61] Integrated optoelectronic circuits with lasers, waveguides, modulators and detectors have been produced on double AlGaAS-GaAs heterostructures with different Al content. New materials have been used as substrates in the production of active devices and they are discussed in many papers.

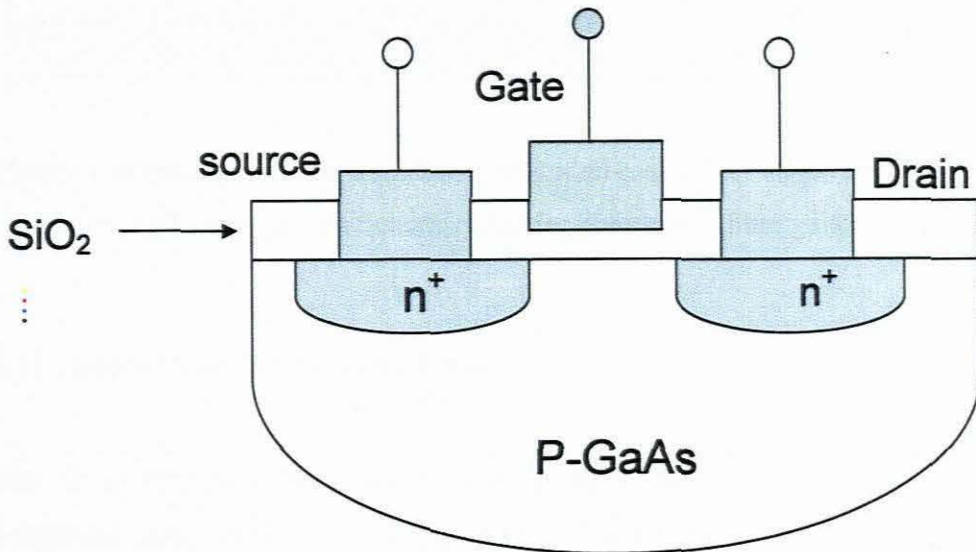

Figure 1.8: Planar structure of the field SHF MOS transistor on gallium arsenide with a narrow approximated gate

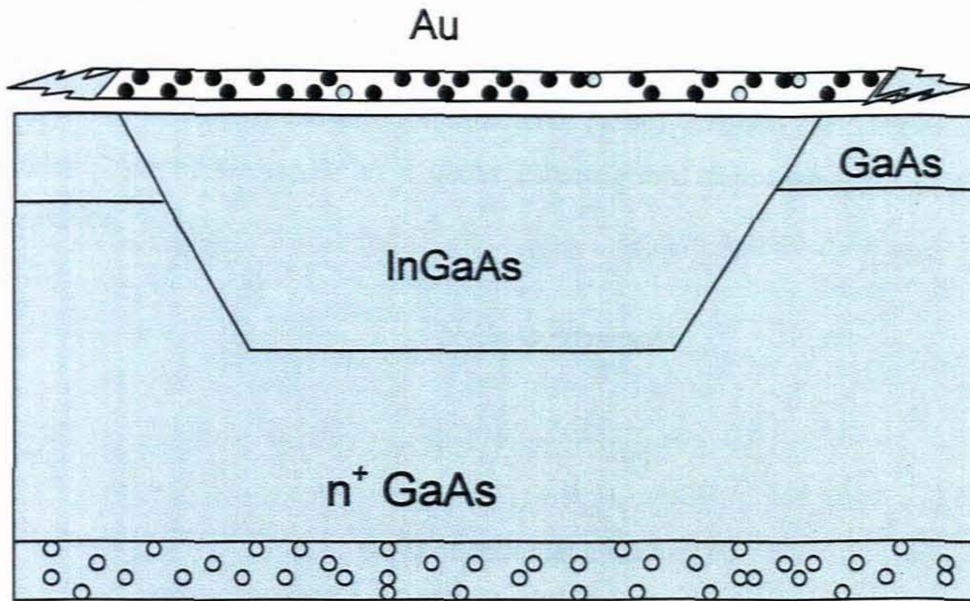

Figure 1.9: Structure of the monolithic integrated circuit that unites a waveguide and a photodetector by the use of a Schottky barrier platinum indium gallium-arsenide

1.11 Applications in Optoelectronics

The CVD technique by which it is possible to apprehend epitaxial depositions of compound semiconductors having a variety of electrical and optical properties became the main preparative method for producing optoelectronic devices having superior performance.

Optoelectronic devices include those converting electrical energy into optical radiation (electroluminescent diodes, laser diodes) or versa (photovoltaic devices), and those detecting optical signals using electronic processes (photodetectors, such as photoconductors, photodiodes, and phototransistors, as well as photocathodes). Other important devices optical waveguides. Electroluminescent diodes (light-emitting diodes)[62-66] are based on efficient spontaneous light emission by means of radioactive recombination processes in p-n junctions made in various III-V compounds. These include direct band gap materials such as $GaAs_{1-x}P_x (x < 0.49)$, $Ga_{1-x}Al_xAs$ ($x < 0.27$) and

$In_{1-x}Ga_xP$ ($x < 0.70$), and indirect band gap materials such $GaAs_{1-xp}P_x$($x < 0.49$), and GaP, in general the light emission being stronger in direct band gap materials. The fabrication technology of commercial electroluminescent diodes involves the epitaxial growth of a graded layer of $GaAs_{1-x}P_x$ on a GaAs substrate and subsequent planar p-n junction formation.

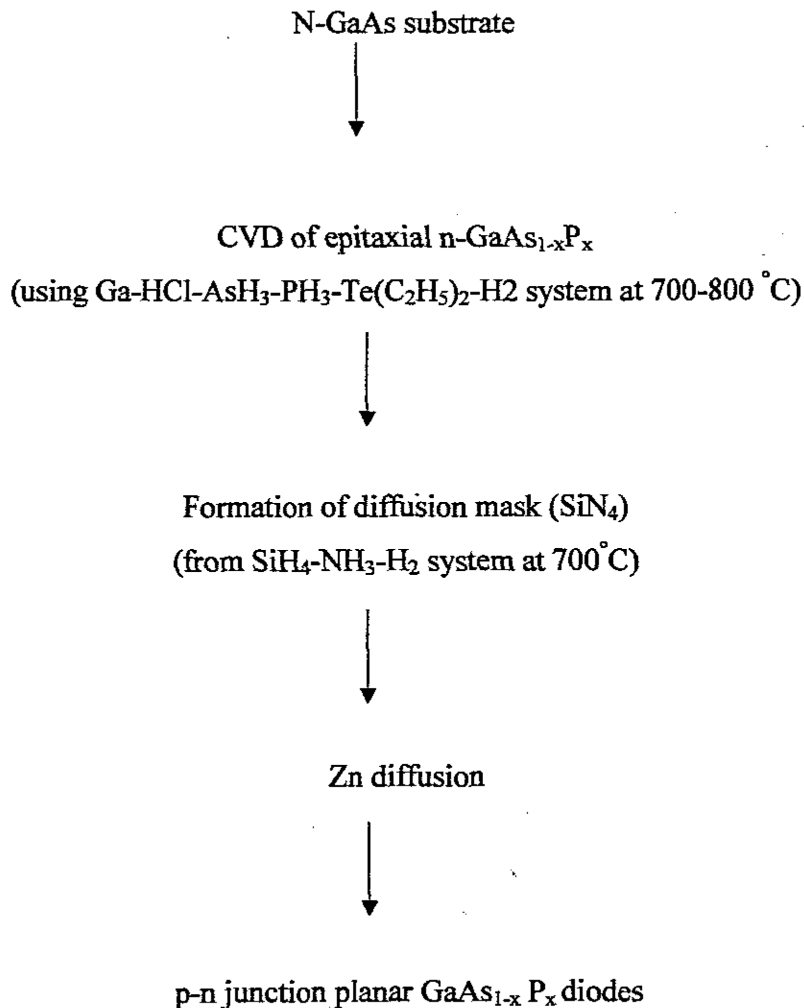

Figure 1.10: Stages for $GaAs_{1-x}P_x$ red LED fabrication ($x = 0.4$).

Using Zn-diffusion through a Si_3N_4 mask (Fig. 1.10). By introducing nitrogen doping, high performance red ($x = 0.4$), orange ($x = 0.65$), yellow ($x = 0.85$) and green ($x = 1.0$)

devices can be fabricated. Other light emitting diodes can be prepared by using the vapour–phase epitaxy of $Ga_{1-x}Al_xAs$ (red), $In_{1-x}Ga_xP$ (red-yellow), GaN (green, blue or violet), SiC (all visible range), etc. Laser diodes [67, 68] are based on stimulated infrared or visible light emission by using radiative recombination processes in p-n junctions made of various III-V compound semiconductors having direct band gaps. Compared with the light emitting diode, the laser diode has an optical cavity and requires electron population inversion. The high performance laser diode incorporates one or more $GaAs\text{-}Al_xGa_{1-x}As$, $GaAs\text{-}Ga_{1-x}In_xP$ or $In_{1-x}Ga_xAs_yP_{1-y}\text{-}InP$ heterojunction lasers (GaAs active layers of 200 Å or less), having a continuous room-temperature on emission based quantum size effects.

Optical waveguides (optical fibres)[69-71] serve for the low-loss transmission of light. A waveguide consists of a central core surrounded by a medium lower refractive index. Presently, the best optical fibres are prepared by means of plasma activated CVD, employing successive deposition of at least two different oxide layers (e.g. SiO_2, GeO_2, B_2O_3 or P_2O_5) onto inner wall of a quartz tube. Other procedures employed are outside vapour-phase oxidation (OVPO) and modified chemical vapour deposition (MCVD).

Solar cells with photovoltaic devices can convert sunlight directly into electrical energy.[72-75] A solar cell consists in principle of p-n homojunction[76, 77], a heterojunction[78], an MIS structure[79] or Schottky barrier. It is composed of the following parts: a substrate which forms a region of the junction (p- or n-type), a deposited or diffused region (n- or p-type, respectively), an antireflection coating, upper and lower metallic contacts and a protective transparent cover.

1.12 Thin film structure

This includes investigation of CVD layers in modern solid-state technology and their structural evaluation. Certainly in many cases there is direct correlation between the structural properties and the device characteristics. Present day semiconductor devices

and integrated circuits include, among others, many CVD layers of semiconductors, dielectric and metals, deposited on a single-crystal substrate.

Due to the continuous development of these increasingly complex multilayer sequences, has lead to the need for precise structural information of the desired film. Structural examination has progressed continuously by considerable improvement of experimental techniques and by development of extremely sophisticated equipment. One of the main objectives of research is to prepare complexes and once prepared characterized them to determine their structural information. Structural information reveals reliability and failure analysis activities of the research conducted. In thin film chemistry structural characterisation broadly deals with the geometry of patterned films where issues of lateral or depth dimensions and tolerances, uniformity of thickness and coverage, are of concern. Further than this, the film surface topography and morphology, including grain size and shape, existence of compounds, presence of hillocks, and evidence of film voids, microcracking or lack of adhesion, formation of textured surfaces are of concern. Somewhat more difficult to obtain, but crucial to microelectronic device fabrication and optical coating technology are the cross-sectional views of multilayer structures where interfacial regions, substrate interactions, and geometry and perfection of electronic devices with associated conducting and lastly, most complex of all, are diffraction patterns, the crystallographic. Information they convey, and the high resolution lattice images of both plain view and transverse film sections. Among the applications mentioned in the previous paragraph are normally addressed by the scanning electron microscope (SEM) and, occasionally by the reflection metallurgical microscope.

Thin film materials deposited using CVD (or other techniques) have the following three main structural forms: single-crystalline, polycrystalline and amorphous. Usually in solid-state technology, semiconducting films are required in the single-crystalline and polycrystalline forms, while dielectric films are used in the amorphous form. All CVD materials, both semiconductors and dielectric have imperfections which can influence their properties. Imperfections may be non-localized (nature) resulting from general film characteristics or localized (process-induced) formed during processing. The capabilities

and limitations of methods and instrumentation suitable for the structural examination of crystalline and amorphous films are discussed in a number of books and review articles.[80]

1.13 Techniques for Studying Thin Film Structure

There are many techniques for the deposition of thin films as listed in Table 1.2.

Table 1.2. Methods for Detecting and Characterizing Defects in Crystalline and Amorphous CVD Films[81]

1	X-ray Methods	X-ray diffraction Laue X-ray back-reflection X-ray double crystal spectrometry X-ray topography
2	Electronic methods	Transmission and replication electron microscopy Scanning electron microscopy Electron diffraction
3	Optical methods	Optical microscopy Multiple beam interferometry IR absorption spectroscopy IR reflectance spectroscopy Optical absorption Light scattering UV reflectance spectroscopy Raman spectroscopy
4	Electrical Methods	Inference from electrical properties Standard and self-healing dielectric breakdown Electrophoretic decoration Decoration by means of electrostatic charging Liquid crystal technique Current-noise measurement

5	Electrochemical Methods	Electrochemical autography Electrolytic gas-bubble formation Electrolytic (electrophoretic) copper decoration
6	Chemical Methods	Selective solution etching of films or substrates Preferential high temperature gas-phase etching
7	Mechanical Methods	Surface profilometry
8	Nuclear Methods	Rutherford ion backscattering and channeling Electron spectroscopy resonance

1.13.1 X-Ray Methods

1.13.1.1 X-Ray Diffraction

This is a very accurate and advantageous method for structural analysis, by using x-ray diffraction it is possible to measure the lattice spacing parameter by which the composition of each phase of the sample is established. The same parameter also allows the thermal expansion coefficient, the lattice strain and the orientation to be determined. Moreover, from the line width and the line intensity the crystalline perfection and polarity differentiation can be established.

The condition for obtaining constructure interference, i.e. the maximum X-ray intensity following diffraction by a crystalline film, is

$$2d \sin \theta = n\lambda \qquad (5)$$

In equation (5) where d is the spacing between two neighbouring planes, 2θ is the X-ray diffraction angle, n is the order, and λ is the x-ray wavelength. Thus from the measurement of 2θ position, d is calculated which is then used to determine the sample composition or orientation by comparing it with that for the powder standards of a particular material.

The effect of mechanical strain is considered negligible when the 2θ positions of the diffraction peaks are identical with those for the powder standards and do not vary with the deposition conditions.

A diffractometer contains an X-ray beam source, a sample mount, a counter for detecting the diffracted beam, a goniometer for measuring the rotation angle of the sample θ and of the detector arm 2θ and a recorder (Figure 1.11).

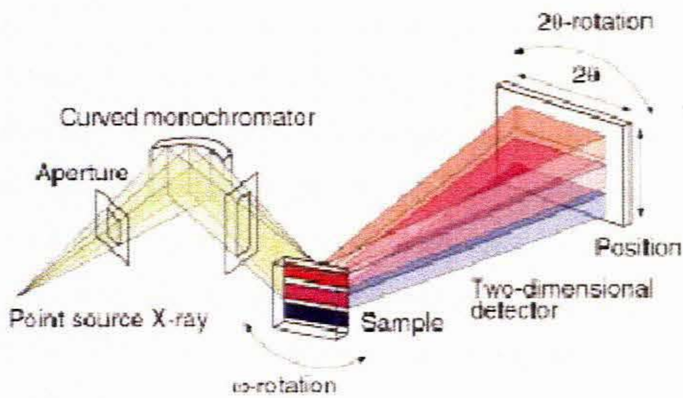

Figure 1.11: X-ray diffractometer

Thin films examined by X-ray diffractometer should have a sufficient thickness (0.1-1 μm depending on the nature of the film). X-ray diffraction has been extensively used in structural investigations of nearly all CVD films. There are a large number of applications of this technique, such as:

- The determination of film substrate orientation relationships in heteroepitaxial silicon[82-84] as well as III-V or II-VI semiconducting films on oxide substrates.
- The determination of crystallite size and orientation, e.g. relative amounts of (111), (100) and (100) texture in poly Si have been found to depend on the deposition rate and film thickness.[85, 86]
- The structural investigation of transparent conducting films (determination of the grain size and polycrystalline SnO_2 films) on glass substrates, observation of the

transition from the polycrystalline to the amorphous state for SnO_2: P once a critical level of P doping is exceeded.

1.13.2. Electronic Methods

1.13.2.1. Transmission (TEM) and Replication (REM) Electron Microscopy

Electron microscopy is widely used for obtaining information on morphology and defects of thin films.[87, 88] This method is based on obtaining a contrast due to both the differential absorption and especially diffusion and interference effects undergone by an electron beam in various regions of the sample, the method is applied either by the direct Transmission Electron Microscopy (TEM) or the indirect Selected Area Electron Diffraction (SAED) procedure. TEM can only be used with very thin samples, usually 100-5000 Å in thickness. Thinning of the sample substrate and, if necessary, of film can be done by two methods, depending on the substrate material, namely chemical or electrolytic methods.

The electron microscope is based on the possibility of electron beam focusing by electrostatic and magnetic field lenses, and consists of an electron gun, a condenser lens, a sample mount, an objective lens, a projector lens and a viewing screen or a photographic plate. TEM is appropriate for studying morphological aspects of CVD films such as grain size and defects, for example dislocation, twins and precipitates etc.

An example illustrating the application of TEM to structural investigations of CVD films is given below:

- Visualization of dislocation, stacking faults, precipitates and voids in epitaxial Si, Ge8[89] and GaAs[90,91]; investigation of interface in artificially structured materials (e.g. AlGaAs-GaAs[92])

1.13.3 Scanning Electron Microscopy

The technique of SEM[93-96] is where a narrow high energy electron beam is scanned across the film surface. The secondary electrons emitted from the interaction of the incident electron beam with the film material are detected amplified and displayed on a cathode ray tube. The contrast arises from the differences in secondary electron emission in various regions of the specimen.

Pairs of scanning coils located at the objective lens deflect the beam either linearly or in random fashion over a rectangular area of the specimen surface. Electron beams having energies ranging from a few thousand to 50 keV, with 30 keV a common value, utilized. Upon impinging on the specimen, the primary electrons decelerate and in losing energy transfer it inelastically to other atomic electrons and to lattice. Through continuous random scattering events, the primary beam effectively spreads and fills a tear drop-shaped interaction volume (Figure 1.12a) with a multitude of electronic excitations. The result is a distribution of electrons that manage to leave the specimen with an energy spectrum shown schematically (Figure 1.12b). In addition, target x-rays are emitted and other signals such as light, heat and specimen current are produced and the sources of their origin can be imaged with appropriate detectors.

The method exhibits many important advantages sufficiently good resolution (100-200 Å) high contrast, high magnification, a large inspection field, simple specimen preparation procedure and a very small sample size. It is very helpful for an easy and detailed examination of surface morphology and localized defects. Insulating specimens are readily made conductive to prevent surface charging from the beam by coating them with a very thin film of metal. The various SEM techniques are differentiated on the basis of what is subsequently detected and imaged.

SEM is like a large X-ray vacuum tube used in conventional X-ray diffraction systems. Electrons emitted from the filament (cathode) are accelerated and strike the specimen target (anode). In the process, X-rays characteristic of atoms in the irradiated area are emitted. By an analysis of their energies, the atoms can be identified and by a count of

the numbers of X-rays emitted the concentration of atoms in the specimen can be determined. This important technique, known as X-ray energy dispersive analysis (EDX) sometimes referred to as EDS or EDAX analysis. It is the technique used for identifying the elemental composition of the specimen, on an area of interest thereof. Most energy-dispersive X-ray analysis systems are interfaced to SEMs, where the electron beam serves to excite characteristic X-rays from the area of the specimen being probed. Attached to the SEM column is the liquid-nitrogen Dewar with its cooled Si (Li) detector is a reverse-biased Si diode doped with Li to create a wide depletion. An incoming X-ray generates a photoelectron that eventually dissipates its energy by creating electron hole pairs. The incident photon energy is linearly proportional to the amplitude of the voltage pulse they generate when separated. The pulses are amplified and then sorted according to voltage amplitude by a multi-channel analyzer, which also counts and stores the number of pulses within given increments of the voltage (energy) range.

SEM is one of the major methods for studying the structural properties of CVD films that can provide information on surface topography and crystallite orientation. Some representative examples illustrating various applications of this method are the following:

- The investigation of the surface appearance of heteroepitaxial semiconducting films of the deposition parameters;
- The investigation of the surface structure and smoothness of piezoelectric and electro-optic materials (AlN, GaN, ZnO) deposited on sapphire substrates;
- The investigation of the surface morphology of heteroepitaxial and polycrystalline semiconducting films for solar cell applications (InP/CdS.poly-GaAs graphite)
- The investigation of the growth morphology of a Si:H and a-Si:β:

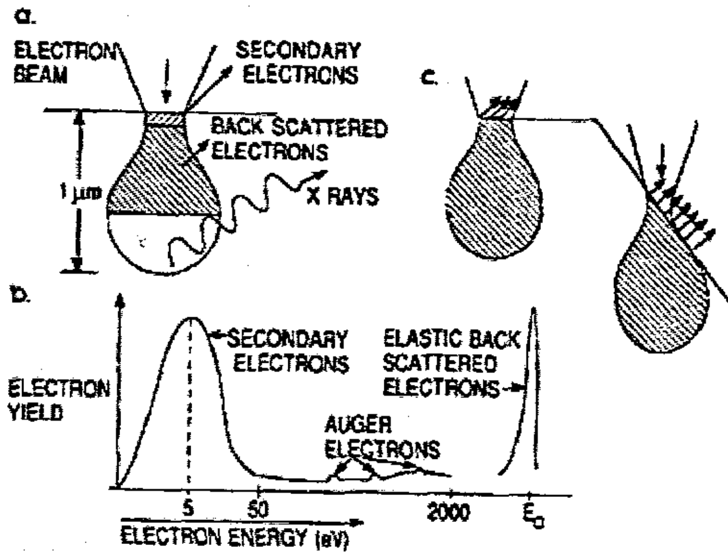

Figure 1.12 a) Electron and photon signals emanating from tear-shaped interaction volume during electron-beam impingement on specimen surface. b) Effect of surface topography on electron emission.[94]

1.13.4 Optical Methods

Optical magnification is the simplest and widest method used for nondestructively obtaining information on film surface topography as well as on the type and density of localized structural defects. The basic instrument is the standard optical metallograph microscope, using various types of illumination such as bright-field, dark-field and oblique or grazing lighting. Various optical contrast methods, such as polarized light, phase contrast, and interference contrast are applied to reveal otherwise invisible morphological details.[93]

The phase-shift microscope is based on shifting the phase of a direct beam with respect to light reflected/diffracted from a specimen. In the interference-contrast microscope, the incident white light is polarized and split into light with two perpendicular components which are slightly laterally displaced. Upon recombination, if there is any phase difference of the two rays i.e. the compounds are out of phase, a coloured interference image is obtained (Figure 1.12).

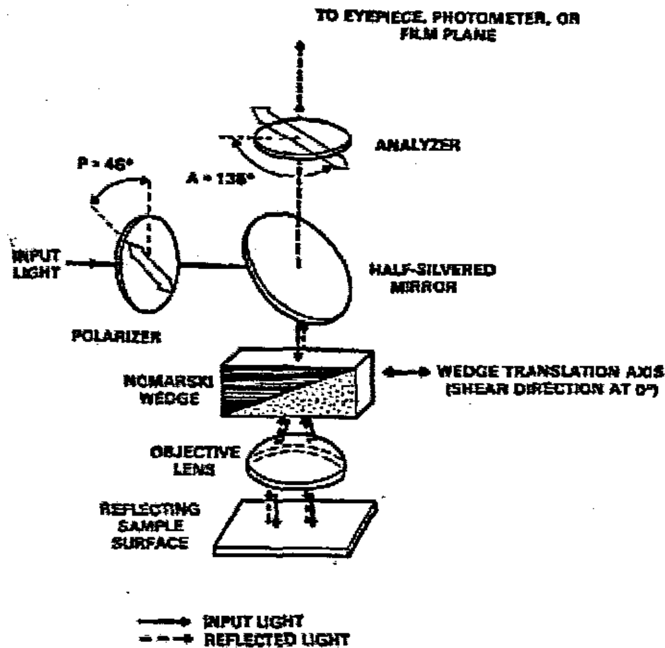

Figure 1.13: Schematic image of the Nomarski differential interference contrast microscope with translating wedge for phase adjustment.

The Nomarski interference technique[94] has been used for observing several defects in silicon epitaxial wafers, such as stacking faults, twins (pyramid growths), as well as various depressions and projections on the wafer surface. Other applications described in the literature are the investigation of surface smoothness and defects of various epitaxial (GaP/GaP, GaP/Si, AlAs/GaAs, $NiFe_2O_4$/MgO), polycrystalline (SnO_2/glass) and amorphous (AsSG/Si) films.

1.13.5 Chemical Methods

Selective chemical etching either in solution or in the gas phase is a widely used method for defect characterization, both for crystalline and amorphous films. Chemical methods, such as chemical dissolution and anodic sectioning, are also useful destructive methods for the structural depth profiling of CVD films. This also falls under the chemical properties of CVD films and their substrates which play a central role in the fabrication of semiconductor devices, i.e. etching, diffusion and oxidation.

Etching means erosion of selective portions of a film or substrate surface using various corrosive agents in order to produce the desired pattern on the surface. Depending on the type of corrosive agent (reactive chemicals, non-reactive ions, or both), the etching may be classified into main categories: chemical etching (subdivided into wet and gaseous chemical etching and plasma etching); physical etching (sputter and ion etching); chemical-physical etching (reactive ion and sputter etching). Recent (alternative etching techniques (such as laser and electrochemical etching and laser-assisted dry etching) also fall into the chemical etching category. Another classification divides etching into wet etching (solution etching, laser chemical etching and electrochemical etching) and dry etching (plasma, reactive ion sputter, ion, and laser etching).

Diffusion is the process of introducing selected impurity atoms into designated areas of a semiconductor substrate or film in order to modify the electrical properties of that area. This process can be considered as essentially a chemical process because, independently of the conventional impurity source type, it involves the reduction of the oxide of a dopant by the semiconductor substrate of film at the oxide-semiconductor interface.

1.13.5.1 Selective Chemical Etching for Crystalline Films or substrates

Chemical etching is one of the most used techniques in present-day semiconductor technology. Indeed, this process is used in almost every fabrication step of a semiconductor device (substrate surface preparation, substrate shaping, thin film patterning, etc.). It is also extensively used in the structural and compositional characterization of crystalline or amorphous semiconducting, amorphous dielectric, metallic, magnetic and superconducting thin films as well as of single crystal slices. Chemical etching is used for structural examination (the detection of lattice defects in crystalline semiconducting films, the determination of crystal orientation and polarity, and substrate thinning) and for analytical examinations.

Chemical etching may occur by the following types of reaction: (1) oxidation-reduction (redox); (2) electrochemical; (3) complexation; (4) exchange or (5) gas phase.

Oxidation-reduction etching reaction. This involves conversion of the material being etched to a soluble higher oxidation state. Some examples of this reaction type are the following.

a) Etching of Si in HNO_3-HF-H_2O mixtures[98-106], which occurs according to the overall etching reaction:

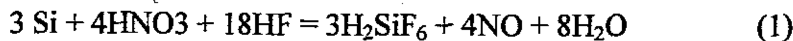

$$3\,Si + 4HNO3 + 18HF = 3H_2SiF_6 + 4NO + 8H_2O \qquad (1)$$

It is supposed that this reaction takes place in two steps, i.e. the oxidation of silicon by nitric acid followed by the reaction of the resulting silicon dioxide with HF forming a water-soluble compound:

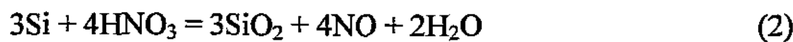

$$3Si + 4HNO_3 = 3SiO_2 + 4NO + 2H_2O \qquad (2)$$

$$SiO_2 + 6HF = H_2SiF_6 + 2H_2O \qquad (3)$$

b) Etching of Si in an aqueous solution containing copper and fluoride ions[21,22]:

$$Si^0 + 2Cu\,(NO_3)_2 + 6NH_4F \longrightarrow (NH_4)_2SiF_6 + 4NH_3 + 2Cu^0 + 4HNO_3 \;(4)$$

In this process, Si is oxidized to Si^{4+} and Cu^{2+} ions reduced by Si to metallic Cu.

1.14 Substrates

1.14.1 Classification and requirements

A substrate is a material on which a CVD film is deposited. When the material is a large single crystal of semiconductor (Si, GaAs), the substrate is usually called a wafer or a slice. Theoretically, a substrate must only provide mechanical support and not interact with the thin film except for ensuring sufficient adhesion. In practice, however, the substrate exerts a considerable influence on the characteristics of a CVD film. Substrate materials used in CVD thin film technology [108-110] can be classified according to several criteria:

1) *Crystallinity.* Amorphous (glass, silica), polycrystalline (alumina, metals) and monocrystalline (elemental and compound semiconductors, sapphire, spinel).

2) *Electrical conductivity.* Conductors (metals), semiconductors (Si, Ge, III-V, II-VI and IV-VI compounds) and insulators (sapphire, spinel).
3) *Chemical composition.* Elements (Si, Ge, metals, oxides (sapphire, spinel, garnets, silica, glass), sulphides (ZnS, CdS, PbS), selenides, tellurides, phosphides (GaP, InP), arsenides (GaAs, InAs) and antimonides (GaSb, InSb), etc.
4) *Application field.* Substrates used for discrete devices and integrated circuits (Si, Ge, sapphire, GaAs), optoelectronics (GaAs, GaP), microwave devices and circuits (GaAs, Si, alumina, sapphire), magnetic bubble memories (garnets) and surface acoustic wave devices (sapphire).
5) *Light transmission.* Transparent (glass, sapphire, spinel) and opaque materials.
6) *Operation.* Active (semiconductors, sapphire, garnets) and passive (glass, alumina) substrates; the utilization of the latter is not dependent on the deposition of an epitaxial layer.
7) *Deposited layer crystallinity.* Substrates used for homoepitaxial (monocrystalline substrates), heteroepitaxial (insulating and semiconducting crystalline substrates), polycrystalline (any substrate) and amorphous (any substrate) layer deposition.
8) *Thermal stability.* Substrates that are stable thermally only at lower ($\leq 500\ ^{\circ}C$) temperatures (glass, InSb), at intermediate ($\leq 700\text{-}900\ ^{\circ}C$) temperatures (GaAs, GaSb, InP, InAs) or in the entire temperature range ($\leq 1250\ ^{\circ}C$) used in CVD (Si, sapphire, spinel, garnets, silica).

Substrates used in a CVD film technology should meet some general and some special requirements. More stringent substrate requirements are always encountered in the production of high quality homo and heteroepitaxial films. General substrate requirements are as follows: single crystallinity with few crystalline defects and low lattice mismatch to the film material; a minimum number of surface defects; a thermal expansion coefficient similar to that of the film; chemical inertness to the growth conditions; chemical; mechanical and thermal stability. Fulfillment of the above requirements will allow the nucleation of a single crystal film with good crystalline quality, few interfacial defects, low stress and low contamination from and, with the ability to withstand further processing.

For particular applications, other considerations could be important such as: high thermal conductivity (required for high power microwave circuit applications), high transparency in a wide wavelength range (NEA photocathodes) and low acoustic wave attenuation (SAW devices) of the substrate.

1.14.2 Properties and uses of substrates

Active substrates: These substrates are very interesting especially for homo and heteroepitaxial growth. They can also be used for polycrystalline and amorphous film deposition. Si, GaAs, GaP, sapphire, spinel and garnets are the most used active substrates. Ge, SiC, GaSb, InAs, InP, InSb have, at present, only a limited commercial applicability.

Silicon wafers [111, 112] : In these wafers the starting material in the fabrication technology of most semiconductor devices and integrated circuits. They are prepared by converting polycrystalline silicon material into a single crystal, using two basic crystal growing processes, namely the float zone method and Czochralski method. The first process relies on freezing of a molten zone initially established at the lower end of a polycrystalline bar in contact with a single crystal seed. The second process consists of withdrawing the crystal from silicon melt contained in a quartz crucible, surrounded by RF or resistance heated graphite susceptors.

III-V compound semiconductor substrates (GaAs, GaP, etc.) [113, 114] : These substrates are widely used for fabricating various microwave and optoelectronic devices. Single crystals of III-V compound semiconductors are obtained mainly by two methods, namely the horizontal-gradient freeze techniques in silica boats and the liquid encapsulation Czochralski technique. Commonly available material may be undoped n-type doped or semi-insulating. For example, GaAs wafers may be undoped n-type (10^5-10^{16} atoms/cm^3), doped n-type (Se, Si, S, Te, Sn- 10^{17}-10^{18} atoms/cm^3), doped p-type (Cd, Zn 10^{17}-10^{19} atoms/cm^3) or semi-insulating (Cr 10^6-10^8 Ω cm). The diameter of the currently available GaAs wafers is greater than 2" (50 mm).

Glass substrates[115] : Have a barium aluminium borosilicate composition. Their properties, such as high volume resistivity, lack of alkaline ion impurities and high surface smoothness (60 Å) are required for some electronic thin film circuits such as those including resistors. Glass substrates are typically produced as 2" X 2" flat-plate substrate having a thickness of 0.5 to 1 mm.

Oxide substrates (sapphire, spinel)[116,117] : are obtained by the following four methods: the flame fusion method, the Czorchralski method, the heat exchanger method and the defined film fed method. Polished sapphire substrates are now available up to 10" in diameter. Sapphire substrates offer good stability at high temperatures, resistance to chemical attack, good electric isolation, excellent thermal conductivity, a high dielectric constant and a low loss factor. Consequently, they are extensively used in the preparation of heteroepitaxial semiconductor films for various electronic devices such as SOS devices, microwave integrated circuits and SAW devices.

Passive substrates : These substrates include alumina ceramic substrates and glass substrates which are applied to thin film resistors (hybrid integrated circuits) and conductors, dielectrics and resistors (hybrid microwave integrated circuits).

Alumina ceramic substrates[118] : are formed from a dense small-grained 99.5% aluminium-oxide and have a surface smoothness better than 2000 Å. Owing to their electrical insulation ability, thermal deformation stability and heat dissipation characteristics, these substrates are extensively used in microwave electronics. Glazed alumina, which offers a surface finish better than 250 Å, can be used for thin film deposition up to 700 °C. Al_2O_3 substrates are also prepared as 2" x 2" sheets.

1.15 Measurement of thin film thickness

The knowledge of thin film thickness is of great importance not only in the study of their formation kinetics or physicochemical properties, but also in technology, particularly in

the fabrication of electronic components where stringent tolerances are usually required. For a CVD thin film which generally has smooth and parallel boundary surfaces, the thickness can be defined as the least distance between two boundary surfaces.

There have been many numerous methods for measuring CVD film thickness in the range 0.01-10 μm, as used in the electronic device industry. All show both advantages and disadvantages, which must be taken into account when selecting the appropriate method for a particular application. Thin film thickness can be measured either during deposition process, or after removal of the sample from the deposition apparatus. *In-situ* measurements have many advantages, such as the possibility of continuously monitoring the film thickness and of halting the deposition process at any desired film thickness. Also, any fluctuations in the deposition are instantly detected so that a certain film thickness can eventually be reached by using an accelerated or retarded process, as required in some applications. Thin film measurement can be performed both destructively and nondestructively. Non-destructive methods are generally preferred because they are quicker, cheaper and allow direct control of all depositions obtained.

According to the type of measurement, techniques of CVD film thickness measurement can be divided into several groups, namely: mechanical (sample weighing, mechanical step-height measurement); mechanical-optical (angle lap and stain, stacking fault dimension, grooving); optical (colour chart, interferometry, ellipsometry, variable-angle monochromatic fringe observation, constant-angle reflection interference spectroscopy, infrared transmission or reflection, visible or infrared radiation interference, Fourier transform spectrometry, prism coupling); and electrical (capacitance bridge, conductivity) methods.

1.15.1 Mechanical Methods

1.15.1.1 Sample weighing method

Generally in this method, the substrate is weighed before and after deposition and the film thickness can be determined if the density is known.[119, 120] The method can be

useful for measuring the thickness even during layer deposition, when the support has been placed on one arm of a microbalance for example. If A, ρ, h, m, are the area, density, thickness and mass of the deposited layer, respectively, then $hA\rho = m$, hence $h = m/A\rho$. The method is simple, rapid and nondestructive. Its disadvantages are the difficulty of measuring the area for irregularly shaped substrates; the need to know the exact density of the film; the possibility of errors due to the deposition on the lateral sides and back of the substrate; the need to use a high sensitivity balance (0.1 μg); and only mean thickness can be measured.

1.15.1.2 Profilometer Method

The measurement of film thickness can be achieved by using a mechanical stylus (a pyramid-shaped diamond needle).[121-126] The method also enables the deposited surface layer profile to be traced. Because of irregularities in the surface examined, the stylus suffers a vertical displacement while being moved on the surface (Figure 1.14).

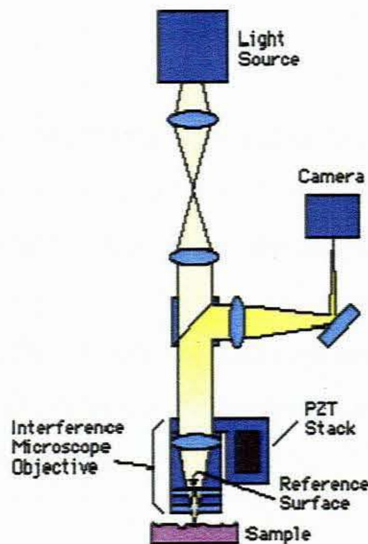

Figure 1.14: Schematic diagram of a surface relief measuring instrument (profilometer)

The variation in induction caused by the change in distance between the transducer and the silicon wafer is detected electronically. The amplified electric signal (maximum gain

10^6) is applied to a strip chart recorder and the surface profile of the film studied is reproduced to high accuracy. Measurement of the surface texture around a step etched in the film gives the film thickness. Such a thickness measuring instrument involves the following components: a transducer provided with gears and a motor to drive the stylus over the wafer surface, an electronic unit to amplify the signal obtained and a recorder (Fig. 1.14). This method is rapid and simple, the minimum measurable thickness being 5-50 Å. However, it requires creation of a layer-substrate step. Greater accuracy is obtained only when the film and substrate are smooth.

1.15.1.3 Interferometer Method

Interferometer method provides thin film thickness measurement based on the interference undergone by a monochromatic light beam incident on a reflecting surface possessing a step. This beam is split into fringes separated by a distance equal to $\lambda/2$, where λ is the monochromatic light wavelength. The fringe displacement due to the step height, as well as the interval between the fringes, can be measured and correlated with film thickness.[127-131]

The variant based on single-beam interference (Michelson interferometry) allows the measurement of film thickness of 200 Å minimum. The multiple beam interference variant (Tolansky interferometry) allows the measurement of film thickness of 25 Å to be measured. In the latter method, the multiple beams are obtained from the incident beam which is repeatedly reflected between two high-reflectivity low-absorptive surfaces. The monochromatic light interference fringes are produced in a space limited by the sample surface and a semi-silvered mirror.

Light passes from a monochromatic source (namely a sodium vapour lamp, $\lambda = 2.946$ Å) through a condenser, a diaphragm, a collimator and a filter and falls on a semi-silvered mirror. It is then partially reflected to the interference system, which consists of a substrate covered by a thin reflecting optical flat is placed. The optical flat forms an angle θ with the support. The interference fringes appear at a step in the film deposited on the support. The thickness h of the deposited layer is given by

$$h = \frac{\Delta l}{l} \frac{\lambda}{2} \qquad (7)$$

where Δl is the interference fringe displacement, and l is the distance between two neighbouring fringes. The accuracy of the method increases if a highly reflecting layer of aluminium or silver is deposited to cover the step in the film on the support surface. In order to obtain a sharp step in the deposited layer, the film deposited on part of the support is completely removed etching.

CHAPTER 2

SYNTHESIS AND CHARACTERISATION OF COMPLEXES FOR THE DEPOSITION OF THIN FILMS

2. EXPERIMENTAL SECTION

2.1. Reagents

Cobalt (II) chloride hexahydrate, nickel (II) chloride, manganese (II) chloride dihydrate, thiourea, N, N'-phenylthiourea, and N, N'-dicyclohexylthiourea obtained from Alfa Aesar and Aldrich, were used as purchased. Ethanol and benzene n-butyl alcohol (analytical grade) were used without further purification and distilled water was also used as solvents.

2.1.1 Instrumentation

(a) Microanalysis

Microanalysis was performed on a CARLO ERBA elemental analyzer for C, H, N, and S.

(b) FT-IR spectroscopy

Infrared spectra were recorded on FT-IR Perkin Elmer paragon 1000 spectrophotometer using KBr pellets in the range of (4000-400 cm^{-1}, 10% resolution)

(c) Mass Spectrometry

Mass Spectra was recorded on a Kratos concept 1S instrument

(d) Single X-ray crystallography

X-ray data were collected on a Bruker APEX CCD[132] diffractometer with MoKα radiation ($\lambda = 0.71069$ Å) using ϕ and ω scans. The crystals were mounted using a drop of fomblin (perfluoropolymethylisopropyl ether) oil in a Hamilton Cryoloop and sample cooling was achieved using a nitrogen gas stream from an Oxford Cryosystems 700 Series Cryostream Cooler. The data were processed using SAINT[133] and empirical absorption corrections were applied using SADABS.[132] Because the crystals of compound VI, $[NiCl_2(SC(NHC_6H_{11})_2)_2]$ diffracted very weakly, the data were cut at 0.95 Å resolution for this sample. The structures were solved by direct methods using SHELXS97[134] and refined anisotropically (non-hydrogen atoms) by full-matrix least-

squares on F^2 using SHELXL-97.[134] The H atoms were calculated geometrically and refined with a riding model. In compound VII, $[MnCl_2(CS(NH_2)_2)_4]$ the H atoms were refined anisotropically, and H atoms refined isotopically, with Ueq values constrained to be 1.2 times those of the parent atoms. The SHELXTL package[132] was used for all the calculations and preparation of the plots for publication.

2.1.2 Preparation of precursors

All precursors of Ni, Co, Cd and Mn were prepared in a stoichiometric amounts of [1:2] using the following alkylthiourea ligands, thiourea, phenylthiourea and dicyclohexylthiourea. Most complexes were synthesized using ethanol or methanol as solvents, except $[CoCl_2(CS(NH_2)_2)_2]$ complex which yielded a greater yield using *n*-butyl alcohol and intermittently the benzene added to supersaturate the solution, facilitating the production of a crystalline precipitate. Most complexes yielded monomers as expected except for some of the manganese complexes. The single crystal for nickel dicyclohexylthiourea complex and cobalt thiourea complex that crystallized was grown in warm methanol or ethanol solution, which was allowed to concentrate upon cooling at room temperature for several days. Attempts to grow crystals for Cd, Mn, and Co complexes yielded no crystals; giving products in powder form.

2.1.2.1 Synthesis of Cobalt Precursors

(a) $[CoCl_2(CS(NH_2)_2)_2]$ (I)

$CoCl_2.6H_2O$ (4.25 g; 0.02 mole) was dissolved in 30 mL hot n-butanol and (3.04 g, 0.04 mole) of thiourea added. The mixture was refluxed for 3 hrs on heating until complete dissolution of the entire solid was attained. After this solution had cooled to room temperature, benzene was added until a slight permanent turbidity was produced. Thus further cooling in an ice chest resulted in a blue solid precipitating out of solution. The precipitate was then filtered washed twice with ethanol and acetone under vacuum. Yield: 74.2%, 3.74 g, Mol. Wt: 282 g/mol., M.pt: 279.5-280.1 °C. $C_2H_8N_4Cl_2S_2Co$: Anal.

Calcd: C: 8.47, H: 2.46, N: 19.78, S: 22.63; Found: C: 8.52, H: 2.86, N: 19.86, S: 22.74, FT-IR (KBr pellets/cm^{-1}); $\nu s(CS)$ 704, $\delta_s(SCN)$ 462, $\rho(NH_2)$ 1094, $\nu s(NCN)$ 1493, $\delta(NH_2)$ 1618, $\nu s(NH_2)$ 3233, $\nu_{as}(NH_2)$ 3350.

(b) $[CoCl_2(CSNHC_6H_5NH_2)_2$ (II)

$CoCl_2.6H_2O$ (2.38 g, 0.01 mole) was dissolved in 30 mL hot ethanol and (3.04 g, 0.02 mol) of phenylthiourea was subsequently added. The mixture was refluxed for 2 hrs on heating and a colour change from red to dark blue was observed after 30 min. The blue solution was stirred hot for 30 min. and was allowed to cool at room temperature. The solution was filtered hot and left for 24 hrs for a crystalline precipitate to form, the crystalline precipitate was then suction filtered to yield a blue green crystalline product. Yield: 65.4%, 2.84 g, Mol. Wt: 434.02 g/mol., M.pt: 284.5-285.2 °C. $C_{14}H_{16}N_4Cl_2S_2Co$: Anal. Calcd: C: 38.50, H: 3.71, N: 12.90, S: 14.77; Found: C: 38.50, H: 2.95, N: 12.15, S: 14.05, FT-IR (KBr pellets/cm^{-1}); $\nu_s(CS)$ 744, $\delta_s(SCN)$ 505, $\rho(NH_2)$ 1054, $\nu_s(NCN)$ 1493, $\delta(NH_2)$ 1624, $\nu_s(NH_2)$ 3233, $\nu_{as}(NH_2)$ 3430.

(c) $[CoCl_2(SC(NHC_6H_{11})_2)_2]$ (III)

$CoCl_2.6H_2O$ (2.38 g, 0.01 mole) was dissolved in 30 mL hot ethanol and (4.80g, 0.02 mol) of dicyclohexylthiourea was added. The mixture was refluxed for 2 hrs on heating to form a blue precipitate. The solution was then suction filtered hot to yield a light blue powder. Yield: 65.7%, 4.00g; Mol. Wt: 609.20 g/mol., M.pt: 300-300.3 °C. $C_{26}H_{48}N_4Cl_2S_2Ni$: Anal. Calcd: C: 51.14, H: 7.92, N: 9.17, S: 10.50; Found: C: 50.87, H: 8.02, N: 9.11, S: 10.27, FT-IR (KBr pellets/cm^{-1}); $\nu_s(CS)$ 978, $\delta_s(SCN)$ 569, $\nu_s(NCN)$ 1450, $\nu_{as}(NH)$ 1564, $\nu_{as}(CS)$ 1233.

2.1.2.2 Synthesis of Nickel Precursors

(a) $[NiCl_2(CS(NH_2)_2)_2]$ (IV)

$NiCl_2.6H_2O$ (2.38 g, 0.01 mole) was dissolved in 30 mL hot ethanol and (1.52 g, 0.02 mol) of thiourea was added. The mixture was refluxed for 2 hrs on heating to form a yellowish green precipitate solution. On cooling, the yellow precipitate changed to green

colour. The solution was then filtered hot by suction under nitrogen to prevent decomposition by air which yielded a yellow powder. Yield: 71.0%, 2.00 g; Mol. Wt: 281.77 g/mol., M.pt:249.5-250.1 °C. $C_2H_8N_4Cl_2S_2Ni$: Anal. Calcd: C: 8.52, H: 2.86, N: 19.88, S: 22.75; Found: C: 8.16, H: 2.80, N: 18.96, S: 22.20, FT-IR (KBr pellets/cm^{-1}); v_s (CS) 711, δ_s(SCN) 463, $\rho(NH_2)$ 1075 v_s(NCN) 1478, v_{as}(CS) 1370, $\delta(NH_2)$ 1598, v_s (NH_2) 3259, $v_{as}(NH_2)$ 3350.

(b) $[NiCl_2(CSNHC_6H_5NH_2)_2]$ (V)

$NiCl_2.6H_2O$ (2.38 g, 0.01 mole) was dissolved in 30 mL hot ethanol and (3.04 g, 0.02 mol) of phenylthiourea was added. The mixture was refluxed for 2 hrs on heating changing from a yellowish green solution to a light green brownish solution. On cooling, the greenish-brown precipitate settled at the bottom. The solution was then suction filtered and the light brown powdery product was left under nitrogen until it was stable from decomposition by air. The light brown precipitate was washed twice with ethanol and acetone. Yield: 74.7%, 3.24 g Mol. Wt: 433.77 g/mol., M. pt: 208.2-208.7 °C $C_{14}H_{16}N_4Cl_2S_2Ni$: Anal. Calcd: C: 40.61, H: 5.84, N: 6.77, S: 15.49; Found: C: 39.85, H: 5.81, N: 6.70, S: 15.10, FT-IR (KBr pellets/cm^{-1}); v_s(CS) 736, δ_s(SCN) 594, $\rho(NH_2)$ 1068 v_s(NCN) 1450, v_{as}(NH) 1554 v_{as}(CS) 1292, $\delta(NH_2)$ 1616, $v_s(NH_2)$ 3197, $v_{as}(NH_2)$ 3417.

(c) $[NiCl_2(SC(NHC_6H_{11})_2)_2]$ (VI)

$NiCl_2.6H_2O$ (2.38 g, 0.02 mole) was dissolved in 30 mL hot ethanol and (4.81 g, 0.02 mol) of dicyclohexylthiourea was added. The mixture was refluxed for 2 hrs on heating yielding a dark green precipitate solution. The dark green precipitate solution was suction filtered hot under nitrogen until it was stable from decomposition by air. The dark green crystalline precipitate was washed twice with ethanol and acetone. The filtrate was left for 48 hrs under room temperature which yielded dark green crystals. A single x-ray crystal was isolated for analysis as per the structure in Figure 2.2 a. Yield: 75%, 4.58 g; Mol. Wt: 610.41 g/mol., M.pt: 294.3-294.8 °C. $C_{26}H_{48}N_4Cl_2S_2Ni$: Anal. Calcd: C: 52.19, H: 6.06, N: 9.36, S: 10.72; Found: C: 51.93, H: 6.02, N: 9.28, S: 10.53, FT-IR (KBr pellets/cm^{-1}); v_s(CS) 984, δ_s(SCN) 546, v_s(NCN) 1446, v_{as}(NH) 1542, v_{as} (CS) 1224.

2.1.2.3 Synthesis of Manganese Precursors

(a) $[MnCl_2(CS(NH_2)_2)_4]$ (VII)

$MnCl_2.4H_2O$ (3.24 g, 0.02 mol) was dissolved in 30 mL hot ethanol and (3.04 g, 0.04 mol) of thiourea was added. The mixture was refluxed for 3 hrs on heating yielding a faint yellow precipitate solution. The precipitate was suction filtered and washed twice with ethanol and left to dry under vacuum. The filtrate was left under room temperature for 72 hrs to obtain light yellow crystals. Yield: 86.0%, 3.56 g; Mol. Wt: 430.33 g/mol., M.pt: 199.5-200.1 °C. $C_4H_{16}N_8Cl_2S_4Mn$: Anal. Calcd: C: 11.17, H: 3.75, N: 26.04, S: 29.80; Found: C: 10.90, H: 3.59, N: 25.31, S: 29.30, FT-IR (KBr pellets/cm^{-1}); ν_s(CS) 704, δ_s(SCN) 485, $\rho(NH_2)$ 1084 ν_s(NCN) 1438, ν_{as}(CS) 1377, $\delta(NH_2)$ 1601, $\nu s(NH_2)$ 3270, $\nu_{as}(NH_2)$ 3458.

(b) $[MnCl_2(CSNHC_6H_5NH_2)_2]$ (VIII)

$MnCl_2.4H_2O$ (1.98 g, 0.01 mol) was dissolved in 30 mL hot ethanol and (3.04 g, 0.02 mol) of phenylthiourea was added. The mixture was refluxed for 3 hrs on heating yielding a light white precipitate solution. The precipitate was suction filtered and washed twice with ethanol and left to dry under vacuum. Yield: 74.1%, 2.98 g; Mol. Wt: 402.26 g/mol., M.pt: 350.2-350.7 °C. $C_{14}H_{16}N_4Cl_2S_2Mn$: Anal. Calcd: C: 41.80, H: 4.01, N: 6.96, S: 15.94; Found: C: 40.86, H: 3.56, N: 6.26, S: 14.99, FT-IR (KBr pellets/cm^{-1}); ν_s(CS) 745, δ_s(SCN) 476, $\rho(NH_2)$ 1021 ν_s(NCN) 1443, ν_{as}(NH) 1514, ν_{as}(CS) 1312, $\delta(NH_2)$ 1589, $\nu_s(NH_2)$ 2996, $\nu_{as}(NH_2)$ 3188.

(c) $[MnCl_2(SC(NHC_6H_{11})_2)_2]$ (IX)

$MnCl_2.4H_2O$ (1.98 g, 0.01 mol) was dissolved in 30 mL hot ethanol and (4.81 g, 0.02 mol) of dicyclohexylthiourea was added. The mixture was refluxed for 3 hrs on heating yielding a colourless solution. The colourless solution was left for 24 hrs thereafter white crystals formed which were suction filtered and washed twice with ethanol and left to dry under vacuum. Yield: 69.3%, 4.20 g; Mol. Wt: 606.66 g/mol., M.pt: 287.4-287.9 °C. $C_{26}H_{48}N_4Cl_2S_2Cd$: Anal. Calcd: C: 51.48, H: 7.98, N: 9.24, S: 10.57; Found: C: 51.60, H:

6.98, N: 8.96, S: 10.00, FT-IR (KBr pellets/cm^{-1}); ν_s(CS) 981, δ_s(SCN) 599, ν_s(NCN) 1443, ν_{as}(NH) 1528 ν_{as}(CS) 1339.

2.1.2.4 Synthesis of Cadmium Precursors

(a) $[CdCl_2(CS(NH_2)_2)_2]$ (X)

$CdCl_2.H_2O$ (1.83 g, 0.01 mol) was dissolved in 30 mL hot ethanol and (1.52 g, 0.02 mol) of thiourea was added. The mixture was refluxed for 3 hrs on heating yielding a white precipitate solution. The precipitate was suction filtered and washed twice with ethanol and left to dry under vacuum. Yield: 80.0%, 2.68 g; Mol. Wt: 335.55 g/mol., M.pt: 213.7-214.2 °C. $C_2H_8N_4Cl_2S_2Cd$: Anal. Calcd: C: 7.16, H: 2.40, N: 16.70, S: 19.11; Found: C: 7.20, H: 2.17, N: 16.51, S: 19.29, FT-IR (KBr pellets/cm^{-1}); vs(CS) 710, δ_s (SCN) 485, ρ(NH_2) 1108, ν_{as}(NCN) 1499, ν_{as}(CS) 1390, δ(NH_2) 1607, ν_s(NH_2) 3283, ν_{as} (NH_2) 3381.

(b) $[CdCl_2(CSNHC_6H_5NH_2)_2]$ (XI)

$CdCl_2.H_2O$ (1.83 g, 0.01 mol) was dissolved in 30 mL hot ethanol and (3.04 g, 0.02 mol) of phenylthiourea was added. The mixture was refluxed for 3 hrs on heating yielding a yellow precipitate solution. The precipitate was suction filtered and washed twice with ethanol and left to dry under vacuum. Yield: 71.9%, 3.50 g; Mol. Wt: 487.74 g/mol., M.pt: 249.6-250.1 °C. $C_{14}H_{16}N_4Cl_2S_2Cd$: Anal. Calcd: C: 41.80, H: 4.01, N: 6.96, S: 15.94; Found: C: 40.86, H: 3.56, N: 6.26, S: 14.99, FT-IR (KBr pellets/cm^{-1}); ν_s(CS) 790, δ_s(SCN) 580, ρ(NH_2) 1058, ν_s(NCN) 1488, ν_{as}(NH) 1524, ν_{as}(CS) 1294, δ(NH_2) 1609, ν_s (NH_2) 3287, ν_{as}(NH_2) 3380.

(c) $[CdCl_2(SC(NHC_6H_{11})_2)_2]$ (XII)

$CdCl_2.H_2O$ (1.83 g, 0.01 mol) was dissolved in 30 mL hot ethanol and (3.04 g, 0.02 mol) of dicyclohexylthiourea was added. The mixture was refluxed for 3 hrs on heating yielding a yellow precipitate solution. The precipitate was suction filtered and washed twice with ethanol and left to dry under vacuum. Yield: 67.1%, 4.44 g; Mol. Wt: 664.13, M.pt: 279.8-280.3 °C. $C_{26}H_{48}N_4Cl_2S_2Cd$: Anal. Calcd: C: 47.02, H: 7.22, N: 8.44,S: 9.66;

Found: C: 46.75, H: 7.28, N: 8.40, S: 9.16, FT-IR (KBr pellets/cm^{-1}); ν_s(CS) 761, δ_s (SCN) 569, $\rho(NH_2)$ 1101, ν_s(NCN) 1444, ν_{as}(NH) 1568, ν_{as}(CS) 1228.

2.2 Results and Discussion

2.2.1 Synthesis of all precursors

All the complexes were prepared by the general reaction scheme shown in Figure 2.1 whereby all the atoms required in a deposited material are present in a single molecule. All Co, Ni, Mn and Cd complexes of thiourea, phenylthiourea and dicyclohexylthiourea were refluxed in ethanol in stoichiometric amounts. The respective complexes were obtained in reasonable yield and their melting points were taken indicating the presence of monomers while those of manganese had higher melting points. In this regard, their infrared studies were conducted to elucidate bonding of the metal to the respective sulphur atoms and elemental analysis confirmed their purity as well as the monomeric nature of these manganese complexes. Thermogravimetric studies were also performed to check the feasibility of these complexes and their potential for the deposition of metal chalcogenide thin film as discussed in the second section of this study.

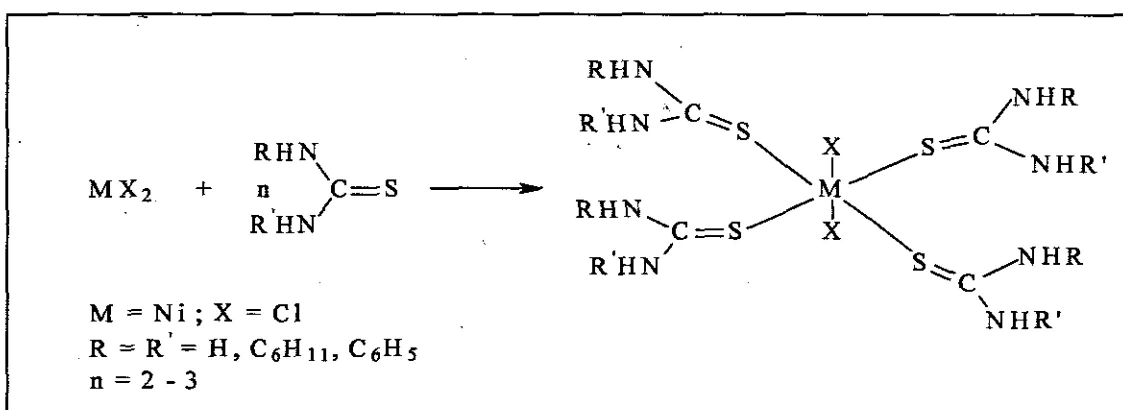

Figure 2.1: Reaction scheme for the synthesis of complexes

2.2.2 Infrared studies

Thiourea has a large dipole moment and an ability to form extensive network of hydrogen bonds. A thermochemistry study with an emphasis on the fundamental measure of the total co-ordinate bond strength conducted by Ashcroft *et al.* showed that thiourea has a low basicity and in aqueous solution, forms complexes with metal ions which are of similar stability to that of the protonated ligand itself.[135-136] The δ_s(S-C-N) bending modes for the complexes [I-XII – 462-569 cm^{-1}] as expected shows a decrease in the frequency shift on coordination of the sulphur to the metal. It is evident that coordination of the thiourea makes the unpaired electrons on the sulphur atom less available for bonding with the other thiourea molecule and readily available to bond with the metal.

The N-H absorption bands are not shifted to the lower frequencies which indicates that nitrogen to metal bonds are not present and the bonding must be between the sulphur and the metal. Similarly from the N-C-N stretching mode at 1493 cm^{-1} there are no observable features of the M-N bond but much enhanced sensitivity to coordination through sulphur, because of the increased double bond character of the C-N bond. Absorptions at 1094cm^{-1}, are attributable to NH_2 rocking mode, which is also not affected by the formation of a metal-sulphide bond. Similar features are observable for all the complexes while those of the dicyclohexylthiourea ligand [III, VI, IX, and XII] do not show peaks for NH_2, which is highly expected but similarly shows the behaviour of the N-H asymmetric stretching of unperturbed sensitivity due to bonding of the sulphur.

These observable features are similar to the attributes of thiourea on coordination reported by Yamaguchi *et al.*[137] that most metals of thiourea exhibit coordination of the metal to sulphur. The is also a clear indication that the cadmium (II), cobalt (II), Mn (II) and Ni (II) alkylthiourea complexes show marked similarity in their structures in that they form clusters, dinuclear or polynuclear compounds on coordination through the M-S bond. It is apparent that infrared studies not only gives information about the compound's structure, but also reveals coordination of the metal to the sulphur.

Table 2.1: Spectroscopic frequencies for the complexes [I- XII]

Assignment (cm^{-1})	I	II	III	IV	V	VI	VII	VIII	IX	X	XI	XII
vs (C=S)	704	744	978	711	736	984	704	745	981	710	790	761
δ_s(S-C-N)	462	505	569	463	594	546	485	476	579	500	580	569
$\rho(NH_2)$	1094	1054	-	1075	1068	-	1084	1021	-	1108	1058	1101
vs N-C-N	1493	1493	1450	1478	1450	1446	1438	1443	1446	1499	1488	1444
vas(N-H)	-	1502	1564	-	1554	1542	1601	1514	1528	-	1524	1568
VasC=S	1423	1297	1233	1370	1292	1224	1377	1312	1339	1390	1294	1228
δNH_2	1618	1624	-	1598	1616	-	1601	1589	-	1607	1609	-
vs NH_2	3233	3233	-	3259	3197	-	3270	2996	-	3283	3287	-
vas NH_2	3350	3430	-	3350	3417	-	3458	3188	-	3381	3381	-

2.2.3 Single X-Ray crystallography

Single crystals of the following complexes $[NiCl_2(SC(NHC_6H_{11})_2]_2$ and $[MnCl_2(CS(NH_2)_2)_4]$ were grown by dissolving the product in methanol and left in room temperature, with subsequent slow evaporation of solvent to yield single crystals thereof. The crystal structures obtained were found to be consistent with the formulae of the complexes and other forms of analysis such as elemental analysis, infrared and mass spectrometry. Details of their data and structural refinement are given in Table 2.2. Their selected bond angles and distances in Table 2.3. A single x-ray crystal of the complex $[CoCl_2(CS(NH_2)_2)_2]$ was obtained in this study which was found to have the same geometry and orientation previously reported by Ramana *et al.*[138] This crystal structure was found to be monoclinic with a space group of c2/c which is observable for

most thiourea complexes.[140] Attempts to grow other crystals were unsuccessful since most complexes were in powder form.

Table 2.2: Crystal data and detailed structure refinement for complexes $[NiCl_2(SC(NHC_6H_{11})_2)_2]$ **(VI)** and $[MnCl_2(CS(NH_2)_2)_4]$ **(VII)**.

Complex	**VI**	**VII**
Empirical formula	$C_{26}H_{48}Cl_2N_4NiS_2$	$C_4H_{16}Cl_2MnN_8S_4$
Formula weight	610.41	430.33
Temperature	100(2) K	100(2) K
Wavelength	0.71073 Å	0.71073 Å
Crystal system	Monoclinic	Tetragonal
Space group	C2/c	P4 (2)/n
Unit cell dimensions	A = 11.3280(12) Å; α = 90°. B = 14.4210(15) Å; β = 90.946 (2)°. C = 19.346(2) Å; γ = 90°.	A = 13.6511 (17) Å; α = 90°. B = 13.6511 (17) Å; β = 90.946 (2)°. C = 8.9664 (15) Å; γ = 90°.
Volume	3160.0(6) $Å^3$	1670.9 (4) $Å^3$
Z	4	4
Density (calculated)	1.283 mg/m^3	1.711 mg/m^3
Absorption coefficient	0.936 mm^{-1}	1.608 mm^{-1}
F(000)	1304	876
Crystal size	0.20 x 0.20 x 0.04 mm^3	0.35 x 0.30 x 0.10 mm^3
θ range for data collection	2.11 to 28.26°.	2.11 to 26.41°.
Index ranges	-14<=h<=14, -18<=k<=17, -24<=l<=24	-17<=h<=16, -17<=k<=12, - 10<=l<=8
Reflections collected	13507	7384

Independent reflections	3690 [R(int) = 0.0607]	1697 [R(int) = 0.0384]
Completeness to θ (25.00°)	99.9 %	98.8 %
Max. and min. Transmission	0.9635 and 0.8348	0.8557 and 0.6030
Goodness-of-fit on F^2	1.036	1.042
Final R indices [I>2sigma (I)]	R1 = 0.0550, wr2 = 0.1132	R1 = 0.0332, wr2 = 0.0681
R indices (all data)	R1 = 0.0794, wr2 = 0.1211	R1 = 0.0503, wr2 = 0.0748
Largest diff. Peak and hole	1.301 and -0.365 e.$Å^{-3}$	0.443 and -0.299 e. $Å^{-3}$

Table 2.3: Selected bond distances (Å) and bond angles (°) for complex $[NiCl_2(SC(NHC_6H_{11})_2)_2]$ **VI.**

Bond distances (Å)		Bond angles (°)	
Ni (1) – S(1)	2.2655(9)	Cl(1)-Ni(1)-S(1)	96.95(3)
Ni(1) – S(1) #1	2.2654(9)	Cl(1)-Ni(1)-S(1) #1	96.96(3)
Ni(1) – S(1)	2.2655(9)	Cl(1)-Ni(1) –S(1)	112.26(3)
Cl(1) – Ni(1)	2.2453(8)	Cl(1)-Ni(1)-S(1) #1	112.26(3)
Cl(1) – Ni(1) #1	2.2454(8)	Cl(1)-Ni(1)-Cl(1)#1	129.75(5)
C(1)-N(2)	1.332(4)	C(1)- S(1)-Ni(1)	106.84(11)
C(1)- N(1)	1.331(4)	S(1)#1-Ni(1)-S(1)	107.86(5)
C(8) – N(2)	1.472(4)	C(1)-N(1)-C(2)	127.2(3)
C(1) – S(1)	1.728(3)	C(1)-N(2)-C(8)	125.4(3)
C(8) – C(13)	1.520(5)	N(2)-C(1)-N(1)	119.8(3)
C(10) – C(11)	1.504(5)	N(2)-C(1)-S(1)	119.5(2)

C(2) – C(3)	1.525(4)	N(1)-C(1)-S(1)	120.7(2)
C(4) – C(5)	1.521(4)	N(1)-C(2)-C(7)	108.4(2)
C(3) – C(4)	1.525(4)	N(1)-C(2)-C(3)	112.5(3)
N(2) - H(2A)...Cl(1)H2	3.281(3)	N(2)-C(8)-C(9)	110.5(3)
N(1)-H(1)- Cl(1)	3.372(3)	N(2)-C(8)-C(13)	110.5(3)

The $[NiCl_2(SC(NHC_6H_{11})_2)_2]$ (VI) structure in Figure 2.2a consists of a 4 coordinated Ni(II) ion in a distorted square planar orientation with the 2 sulphur atoms from the dicyclohexyl thiourea and 2 Cl^- ion from the metal salt. The bond distance for Ni (1)-S (1) #1 and Ni (1)-S (1) 2.654 (9) Å and 2.655 (9) Å are much longer than the Ni (1)-Cl (1) #1 2.2454 (8) Å. The bond angles of the S and Cl around the Ni atom is 112.26(3) [Table 2.3] are much greater than adjacent one comprising of the bond angle of 96.95 (3) causing much distortion to the predicted square planar of 90 °C for all the angles, this could be explained by the constraints from the dicyclohexyl rings coordinated through the sulphur atom. Furthermore the torsion angles found to be 54.12(13) and 167.64(12) are due to electronic effects created by the dicyclohexyl rings during coordination.

The observable feature about thiourea compounds is that they have an intermediate bond character between the double bond of the C-S and the single bond of C-N, where due to this bond character upon coordination there is an increase in the double bond character in C-N and it is much lowered in the C-S to a single bond. The average bond distance for C-N is found to be 1.4005 (average much shorter for C (1)-N (2), C (1)-N (1), C (2)-N (1) and C (8)-N (20), whilst that of C-S is 1.728 Å for a single bond. Each dicyclohexyl ring comprise of a staggered chair cyclohexane and a boat conformation in a corresponding cyclohexyl ring. The chair cyclohexane is in the ring that is joined by the N-H bonds. The hydrogens on adjacent carbons are the same distance apart (~ 0.9900 Å) C(6)-H(6A) -0.9900 and C(7)-H(7a) -0.9900, with minor Van der Waals attraction for each other. The adjacent cyclohexyl ring forms a boat conformation which is much stable relative to the chair conformation which causes torsion strain within the structure and hence

increases distortion of the preferred angle orientation. The packing diagram in Figure 2.2b shows clearly the two conformations exhibited by the cyclohexyl rings.

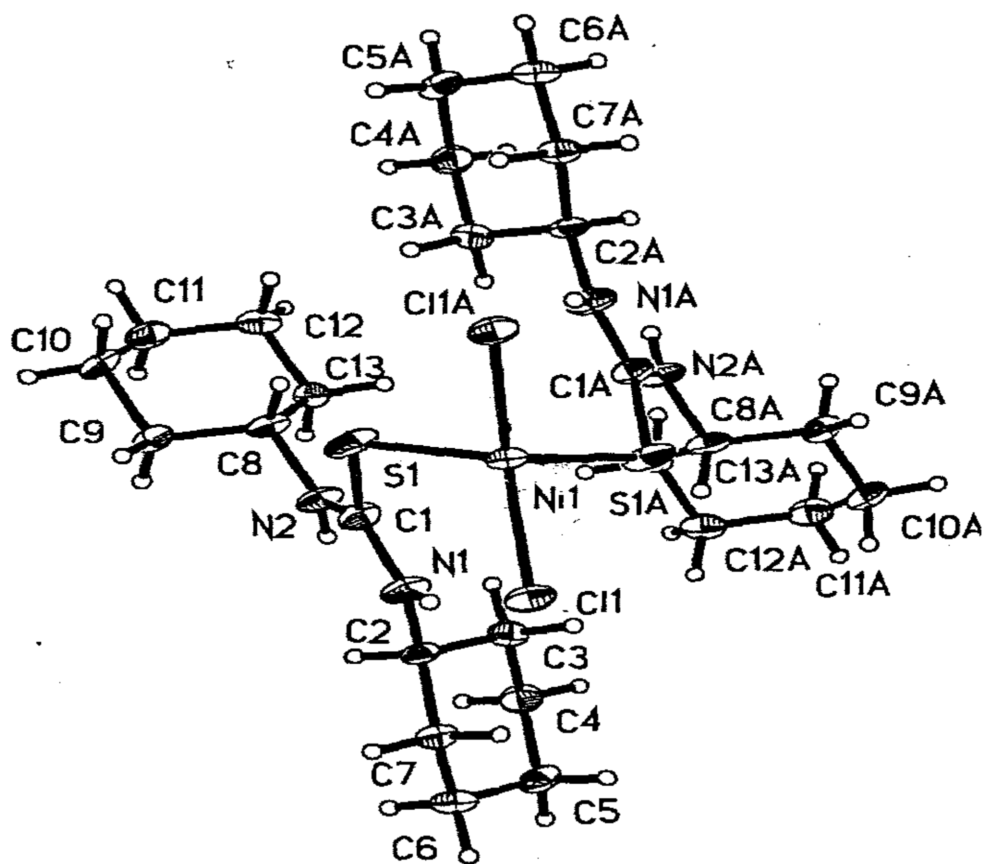

Figure 2.2a: Molecular structure of complex, $[NiCl_2(SC(NHC_6H_{11})_2)_2]$, **(VI)**.

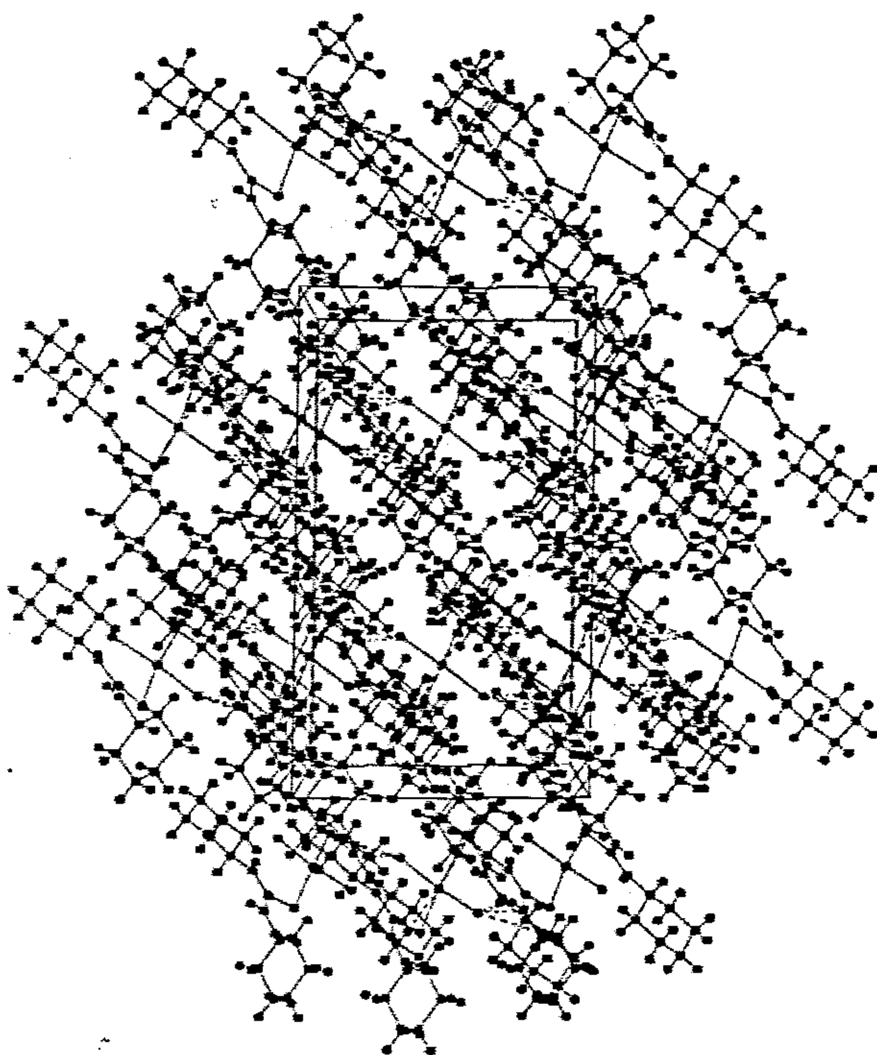

Figure 2.2b: Packing diagram of complex, $[NiCl_2(SC(NHC_6H_{11})_2)_2]$, **(VI)**.

Bond distances (Å)		Bond angles (°)	
Mn(1)-Cl(1) #1	2.5059(7)	Cl(1) #1-Mn(1)-S(1)	88.288(18)
Mn(1)-Cl(1)	2.5059(7)	Cl(1)-Mn(1)-S(1)	91.711(18)
Mn(1)-S(1)	2.6306(7)	Cl(1) #1-Mn(1)-S(1) #1	91.712(18)
Mn(1)-S(1) #1	2.6306(7)	S(1)-Mn(1)-S(1) #1	180.00(3)
Mn(1)-S(2)	2.6765(7)	Cl(1) #1-Mn(1)-S(2) #1	84.396(18)
Mn(1)-S(2) #1	2.6764(7)	Cl(1)-Mn(1)-S(2) #1	95.603(18)
S(1)- C(1)	1.720(2)	S(1)-Mn(1)-S(2) #1	87.339(17)
S(2)-C(2)	1.718(2)	S(1) #1-Mn(1)-S(2) #1	92.661(17)
N(1)-C(1)	1.317(3)	Cl(1) #1-Mn(1)-S(2)	95.605(18)
N(2)-C(2)	1.321(3)	Cl(1)-Mn(1)-S(2)	84.396(18)
N(3)-C(2)	1.315(3)	C(1)-S(1)-Mn(1)	111.68(8)
N(1)-H(1A)	0.87(2)	C(2)-S(2)-Mn(1)	116.20(8)
N(1)-H(1B)	0.80(2)	C(1)-N(1)-H(1A)	120.4(17)
N(2)-H(2A)	0.83(2)	C(1)-N(2)-H(2A)	122.3(17)
N(2)-H(2B)	0.89(2)	C(2)-N(3)-H(3A)	119.8(19)
N(3)-H(3A)	0.80(2)	C(2)-N(3)-H(3B)	119.9(18)
N(3)-H(3B)	0.78(2)	N(1)-C(1)-N(2)	118.6(2)
N(4)-C(2)	1.329(3)	N(1)-C(1)-S(1)	118.8(2)
N(4)-H(4A)	0.75(2)	N(3)-C(2)-S(2)	119.55(19)
N(4)-H(4B)	0.91(2)	N(4)-C(2)-S(2)	121.62(19)

Table 2.4 : Selected bond distances (Å) and bond angles (°) for complex $[MnCl_2(CS(NH_2)_2)_4]$ **VII**

D-H...A	d (D-H)	d (H...A)	D (D...A)	D-H...A
N (1)-H (1B)...Cl(1) #2	0.80(2)	2.53(3)	3.287(3)	159(2)
N (2)-H (2A)...S(2) #2	0.83(2)	2.88(2)	3.548(2)	139(2)

Table 2.5: Hydrogen-bond geometry (Å, °) for complex $[MnCl_2(CS(NH_2)_2)_4]$ **VII**

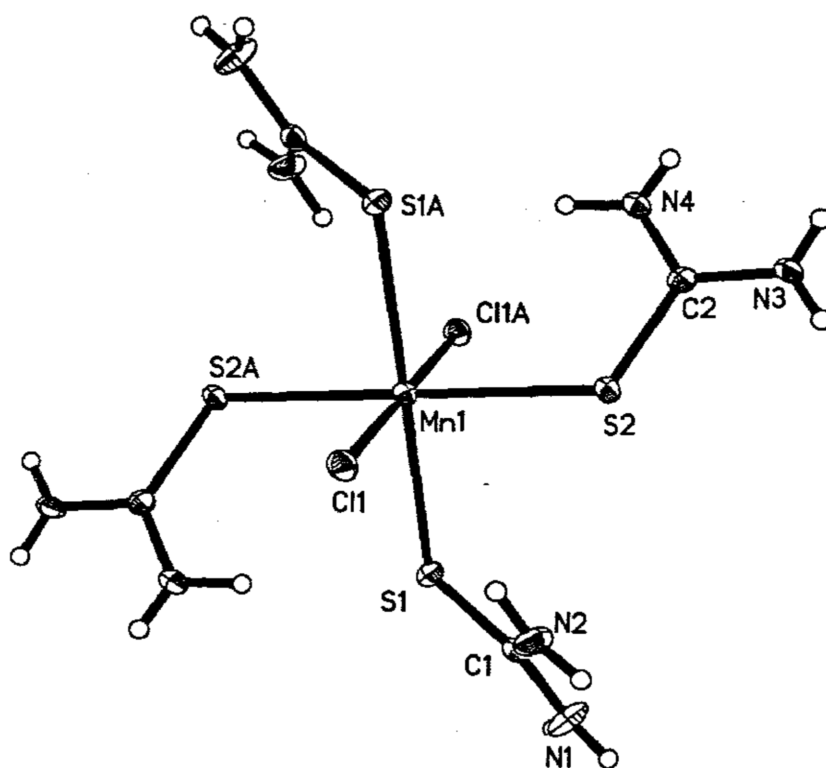

Figure 2.3a: Molecular structure of complex, $[MnCl_2(CS(NH_2)_2)_4]$, **(VII)**.

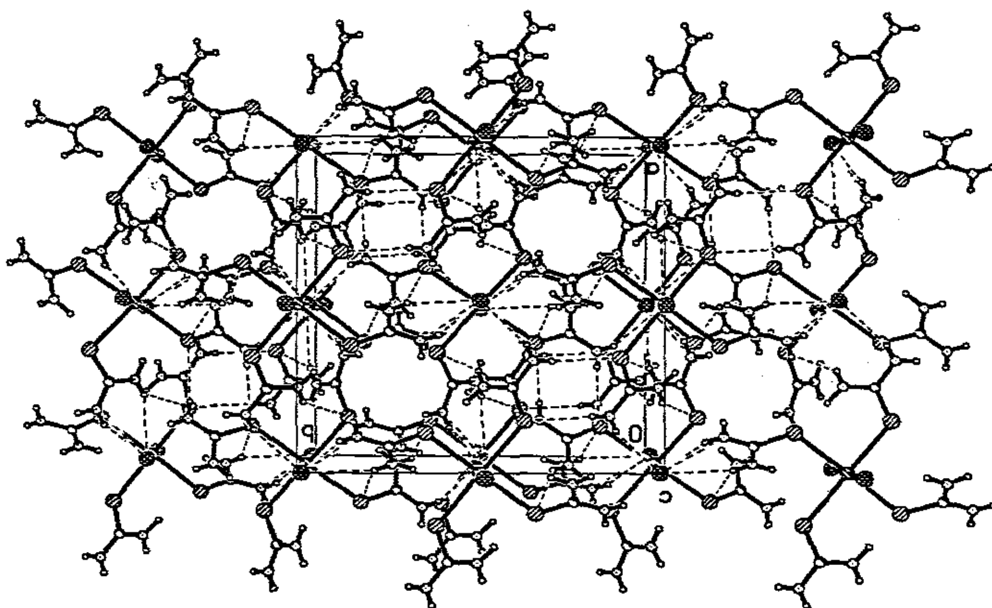

Figure 2.3b: Packing diagram of complex, $[MnCl_2(CS(NH_2)_2)_4]$, **(VII)**.

Divalent manganese ion has an effective $3d^5$ electronic configuration and hence causes least perturbation to the preferred stereochemistry of the complex since the non-bonding shell is symmetrically being half-filled.[139] Evidently as reported by Dash and Rao *et al.* for spin free complexes that the possible and preferred stereochemistry for Mn(II) and bonding orbitals are the following : 4s $4p^3$; 4s $4p^3$ $4d^2$ and 4s $4p^3$ $4d^4$ with the resultant stereochemistry being tetrahedral, octahedral and square antiprism or dodecahedron respectively.[139] Although in this study the preferred stereochemistry for Mn(II) complexes featured tetrahedral and octahedral stereochemistry.

The structure in Figure 2.3 a comprises of the manganese atom coordinated by 4 sulphur atoms from the thiourea ligands around the Mn atom and the 2 chlorine atom above the plane resulting in a slight distorted octahedral coordination geometry. The coordinated 2 Cl^- anions each occupy an axial position, whilst in the equatorial plane, the Mn(II) ion is

coordinated by the 4 thiourea ligands through the S atoms in cis positions, with the maximum deviation from the mean plane calculated to be 0.1476(7) Å. The bond angles show less distortion of the octahedron with S(1)-Mn(1)-S(2) with a bond angle of 92.661 (17)°, while a greater extent of distortion observable in the corresponding geometric angle of S(1)#1-Mn(1)-S(2)#1 with the bond angle of 87.339(17)°. The slight distortion in the orientation of the octahedron is 2.661 from the 90° angle predicted by VSEPR corresponding to octahedral symmetry. The bonded thiourea ligands do not seem to confer much strain on the metal center which might possibly contribute to a larger distortion, as a result forms an almost ideal octahedral.

The bond distances around the Mn ion from Mn(1)-S(2)#1 2.6764(7) Å relative to the adjacent Mn(1)-S(1)-2.6306(7) Å are slightly longer due to a slight torsion from one of the thiourea ligand diagonally opposite the tetragonal system. The mean deviation in distance around the Mn-S bonds is considerably small 0.0917 Å to stabilize the entire structure. The bond angles in the thiourea ligands are also not equivalent with N(3)-C(20)-S(2)-119.55(19)° much shorter than N(4)-C(2)-S(2)-121.62(19)°, whereas those for N(3)-C(2)-N(4)-118.8(2)° in table 2.4 are equivalent, thus this proves that the distortion is through the C=S bond due to coordination to the metal. The packing diagram shows the that the structure consists of molecules in a tetragonal system, orientated in the octahedral geometry held by N(1)-H(1)...Cl(1) in Table 2.5.

2.2.4 Conclusions

The complexes of Co, Ni, Mn and Cd from their alkylthiourea derivatives were synthesized successfully. Following the various analytical measurements performed on these complexes which were consistent and confirmed the purity of these complexes. The synthetic method used for these complexes produced reasonable yields to be used in the second part of this study for the deposition of metal chalcogenide thin films. Crystal structures of bisdicyclohexylthiourea nicke(II)chloride and tetrakisthiourea manganese-(II)chloride were obtained for the first time in this study. A single crystal of bisthiourea cobalt(II)chloride previously reported was also obtained in this study.

CHAPTER 3

DEPOSITION
OF METAL CHALCOGENIDE THIN FILMS

3.1 GENERAL INTRODUCTION

Sulphides of various transition metals show interesting electrical and optical properties such as semi-conductivity, luminescence and photoconductivity.[141-143] An attractive method to prepare these metal sulphides is the degradation of suitable single source precursors, i.e. metal complexes of sulphur containing ligands.[144-146] Thiourea and its derivatives have been used in this study as constituents of the sulphur atoms in the deposition of metal chalcogenide thin films. Thiourea occurs as a mixture of two tautomers: $S = C(NH_2)_2$ (thiourea) + $HS = CNHNH_2$ (isothiourea), accordingly providing three functional groups (amino, imino, and a thiol group).

Single source precursors have definite advantages over the conventional methods, namely solid-state reactions or homogenous precipitation techniques. The requirement of high temperatures (*ca.* 800 °C), long reaction times, formation inseparable mixtures and phase impure compounds handicap the conventional solid-state reactions, while precipitation methods often lead to the formation of amorphous materials which require further annealing to render them crystalline. Moreover, the stability and volatility of the precursors could be increased by tailoring the single source precursors. Therefore these precursors are suitable for the AACVD deposition process due to their stability and volatile nature. The AACVD technique has many advantages over other conventional methods of deposition as it tends to use single source precursors which provide good molecular mixing of chemical precursors enabling the synthesis of multi-component materials with a well controlled stoichiometry. It also allows rapid formation of the deposited phases at relatively low temperatures due to small diffusion distances between reactant and intermediates

Recently metal chalcogenide thin film materials have opened a new area in the field of electronic applications. Their properties can be engineered by changing the crystallite size or thickness and microstructure of the film. Depending upon the deposition conditions, the structural, electrical and optical properties of these materials can be controlled in many ways.[147-151] Essentially one of the main objectives of deposition of

thin films is to obtain films that will adhere to the substrate effectively. This is often not achieved when powdery deposits are achieved instead of crystalline films. Thus it is crucial to obtain ways of optimizing substrate adherence without roughening the surface. One of the methods that have been found to be effective in achieving this goal is the use of the wet chemical etching method. This technique has been used to obtain maximum deposition which results in a smooth surface of the substrate and do not affect thickness measurements of the film being deposited.

3.2 EXPERIMENTAL SECTION – PREPARATION OF THIN FILMS

3.2.1 Chemicals and Materials

The solvents toluene, tetrahydrofuran, ethanol, acetonitrile (HPLC grade) were used as purchased from Fischer Scientific and were of analytical grade. The aluminosilicate microscopic slides were cut into 2 x 2.5 cm^2 pieces. Gallium arsenide (001) single-crystal wafers treated by the Piranha clean method and boat stubs to optimise deposition onto glass substrates.

3.2.2 Instrumentation

3.2.2.1 Thermogravimetric analysis (TGA)

Thermogravimetric analysis (TGA) was performed initially from 50 °C up to 800 °C on Perkin Elmer Pyris 6 TGA with nitrogen flow and heating rate of 10-20 °C min^{-1}. They were later conducted from 20 °C up to 600 °C on a Seiko SSC/S200 model under nitrogen atmosphere (flow rate 20 ml min^{-1}) with a heating rate of 10 °C min^{-1}.

3.2.2.2 X-ray diffraction (XRD)

X-Ray diffraction patterns of thin films were measured using secondary graphite monochromated Cu Kα radiation (40 kV) on either a Phillips X' Pert Materials Diffractometer (APD). Measurements were taken using a glancing angle incidence detector at an angle of 3°, for 2θ values over 10-90° in steps of 0.04°/2s.

3.2.2.3 Scanning Electron Microscopy (SEM)

All films were carbon coated using an Edward's E306A coating system before SEM analysis. Scanning electron microscopy (SEM) and energy dispersive X-ray analysis (EDAX) for films deposited were performed on a Phillips 525 SEM instrument with EDAX 9100 EDS units.

3.2.2.4 UV-Visible Spectroscopy

The optical measurements were performed on a helios (Helioscan) 933322 v 4.55 using intelliscan for thin film measurements in the wavelength taken in the range 200-800 nm.

3.2.2.5 Scanning Interferometer

Thickness measurements were performed with the Zygo New View 100 which utilizes a three-dimensional imaging surface structure analysis by the MetroPro software. The resultant interferogram were captured by a 640 ¥ 480 – pixel CCD array.

3.3 Substrate Cleaning Procedures

3.3.1 General cleaning method

A standard cleaning method was utilized to clean the conventional microscopic slides to prevent organic contamination before the deposition process. The following procedure was used:

- Glass substrates were immersed in 30% nitric acid overnight.
- There were then rinsed in 3 X in deionised water with subsequent sonication for 5 min.
- The substrates were then dried in the oven at 150 °C for an hour.

3.3.2 Glass wet chemical etching

Normally hydrogen fluoride (HF) based etches result in rough surfaces but this procedure has been able to result in smooth surface of the substrate. As it follows that this procedure unlike the other HF techniques utilizes buffered HF and another factor that

which is a great contributor to the resultant etched substrate is the quality of the glass being used and often aluminosilicate glass etches the best.

- A buffered HF mixture is used which was prepared by mixing 40 g of ammonium fluoride (NH_4F) crystals in 60 ml deionised water, this mixture is then transferred to polypropylene or Teflon container.
- Thereafter 10 mL of 49% HF is added to the solution.
- The glass etching solution is made by adding 85 mL deionised water and 5 mL of buffered HF to the water and 9-10 mL of HCl to the solution. The mixture is then stirred with a plastic stirrer.
- A metal mask is patterned on the glass before etching, so that the desired etch regions are exposed and that the backside is protected.
- The glass substrate is then placed in the rinse with deionised water and then blow dried.

3.3.3 Piranha clean

- Cleanliness is the most important requirement for this cleaning procedure. Thus all glassware (beakers) were filled 1/3 full of water with swirling and rinsed 5 times while wafer was inside the beaker.
- Contaminated tweezers are cleaned with a mixture of boiling $H_2SO_4 : H_2O_2$ for 2 minutes.
- The wafer is then placed in the basket thereafter transferred in a beaker with a $HCl:H_2O_2 : H_2O$ (1:1:5) solution for 5 minutes.
- The wafer is then transferred to one of the H_2O baths and removed and placed in one of the beakers with deionised water.
- The wafer is transferred to another beaker and rinsed with deionised water.
- The clean wafer free of organic contaminants is dried under N_2, and ready for use.

3.4 Thin film deposition by CVD

3.4.1 Growth of thin films by AACVD

The precursor was dissolved in a solvent that proved to be soluble, also with reasonable boiling point (toluene, tetrahydrofuran and acetonitrile). A typical experiment would use an average amount of 0.2 g in 30 mL of the respective solvent. The solution was placed in a two necked 100 mL flask with a gas inlet that allowed nitrogen to pass into the solution (to aid transport of aerosol). The glass reactor held a number of glass substrate that was distributed along the length of the reactor and they were heated in a carbolite furnace to the temperature prior to deposition as viewed in Figure 3.1. To optimize the deposition as well as adherence of the film onto the glass substrate boat stubs were used to elevate the glass substrate to facilitate maximum adsorption of the aerosol onto substrates. An aerosol was then generated by the piezoelectric modulator of an ultrasonic humidifier and nitrogen gas passed through the aerosol mist, directing the aerosol to the CVD reactor. A Platon flow gauge was used to control the flow rate in the range of 100-200 cm min^{-1}, enabling controlled delivery of aerosol droplets into the deposition chamber. The aerosol was then allowed to flow over the substrate for a specified time. All deposition experiments were conducted at temperatures of 250-500 °C. It was observed that reproducible results were obtained at temperatures between 350-500 °C.

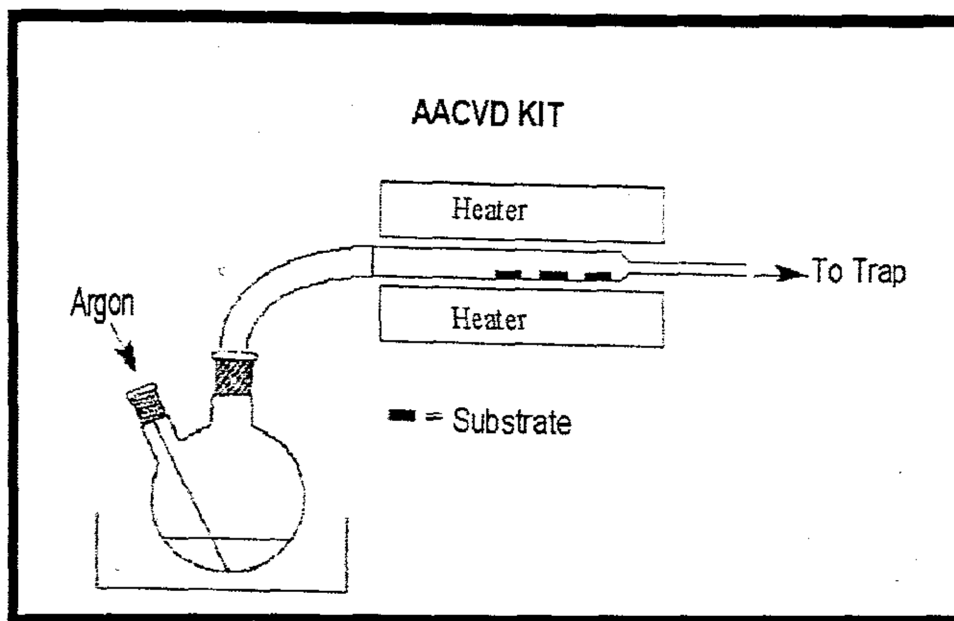

Figure 3.1: Schematic presentation for the AACVD setup

3.5 Results and Discussion

3.5.1 Thermogravimetric analysis for Cobalt Precursors

Thermal decomposition studies on metal coordination complexes have shown various correlations of decomposition temperature with metal ion, ligand character or counter-ion.[149-154] In this study similar observations are found for all the metal alkylthiourea precursors of Cobalt for the complex [I]. Thermal decompositions of the complexes I-III were studied using thermogravimetric (TGA) and differential (DTA) thermal analysis methods in both inert and air atmosphere. Decomposition took place in a two-stage formation with the weight loss of 52.7% from 213-380 found to be the loss of organic residues.[155] The MS residue is found to be from 421.85-766.22 °C, the degradation step initial does not plateau an indication of the loss of the Cl^- ion portion resulting in metal sulphide residue at 47.98% which correlates with the expected theoretical metal sulphide residue 43.63%, with the differences accountable to contaminants therein.

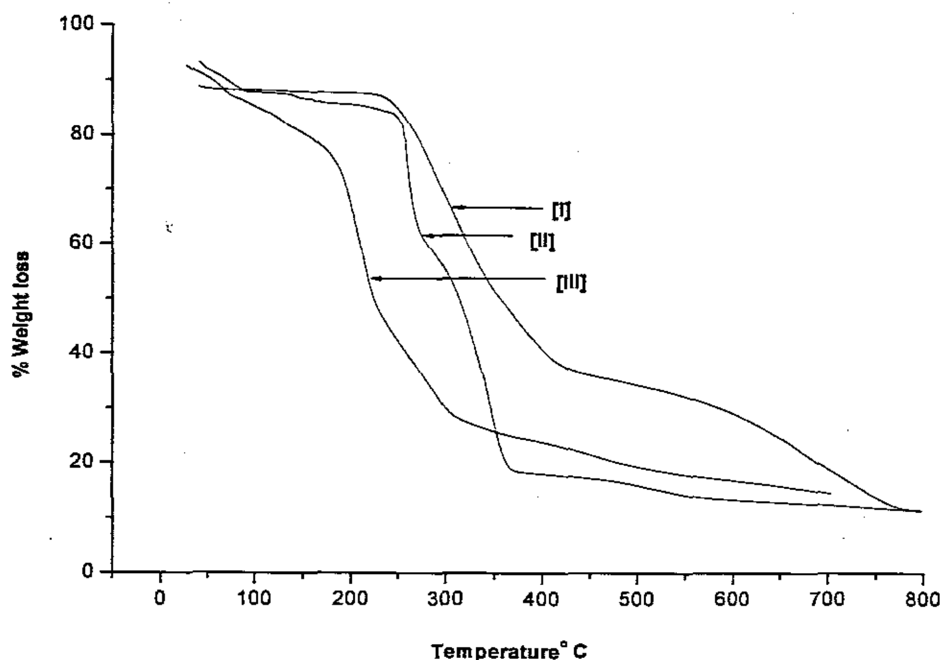

Figure 3.2: TGA spectrum of the Cobalt complexes I, II, III

Generally thiourea complexes on pyrolysis either volatize leaving behind negligible amount of residue or decompose to yield the respective metal sulphide. This is indicative in the two-stage decomposition pattern for [II] found not to correspond to the expected metal sulphide 28.35%, but merely to the negligible amount of residue yielding 38.83%. Complex [III] exhibited a less pronounced 2-stage degradation step from 179-226 °C and 227-315 °C which does not give the expected metal sulphide as could be seen in Table 3.1. It is observable that for all these complexes the decomposition process appears to be quite complex in terms of volatility, all graphs indicate relative volatilization which is the fundamental requirement for the deposition of thin films.

The crystallinity of the deposited films was investigated by powder X-Ray Diffraction (XRD) which showed marked crystallinity with the most intense peak observed at 32.3 °C (620) at 450 °C and indexed as cubic Co_3S_4. The stoichiometric cobalt sulphide normally show amorphous XRD patterns for thin films, but for this study showed reasonable crystallinity for complexes [I] and [II] while for [III] appeared to be highly amorphous.

The XRD pattern (Figure 3.3) of the cobalt sulfide films obtained from complex [I] shows the presence of a mixture of cubic linnaeite Co_3S_4 (JCPDS 42-1448) and cattierite CoS_2 (JCPDS 41-1471). At 400 °C two equivalent peaks distinguished as (411) and (422) with the respective d-spacing in Table 3.1 show only the presence of cattierite CoS_2 while at 450 °C there is the mixture of CoS_2 and Co_3S_4. It is observed that as the temperature increases from 400-450 °C the predominant phase is Co_3S_4 showing marked crystallinity. The morphological studies of the stoichiometric cobalt sulphide thin films were found to comprise mostly of granulated spheres.

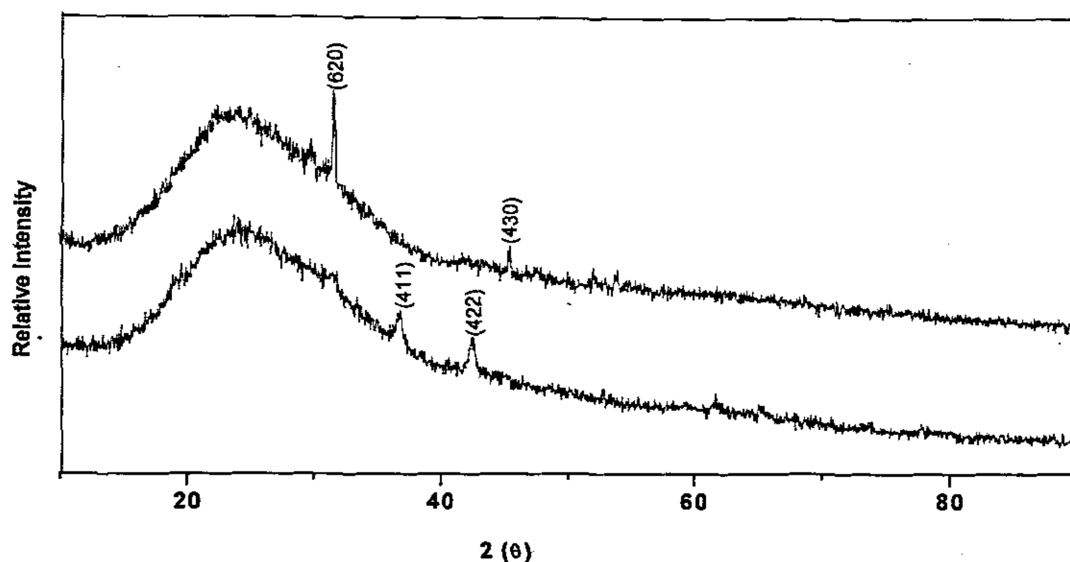

Figure 3.3: XRD pattern for cobalt sulphide from precursor [I] exhibiting CoS_2 and Co_3S_4

Table 3.1 XRD JCPDS data for cobalt sulphide

CoS JCPDS FILES								
41-1471[141]-CoS_2			**42-1448[143]-Co_3S_4**			**73-1703[142]-Co_3S_4**		
hkl	d(lit)/Å(%)	d(exp)/Å	hkl	d(lit)/Å(%)	d(exp)/Å	hkl	d(lit)/Å(%)	d(exp)/Å
411	1.3052(2)	1.2981	311	2.8500(65)	2.7623	620	1.4871(4)	1.4684
422	1.1305(5)	1.1281	533	1.4380(26)	1.4411			
430	1.1075(3)	1.1062	751	1.0890(51)	1.0798			

The XRD pattern (Figure 3.4) of the stoichiometric cobalt sulphide deposited from complex [II] shows the presence of single phase Co_3S_4. Another observable feature of the XRD pattern is that as the temperature is increased the as deposited film becomes more crystalline. Assuming a homogenous strain across crystallites and that the crystallites are isotropic, 3-dimension and spherical the average grain size of microcrystallines can be estimated from the full width at half maximum (FWHM) values of the diffraction peaks. An average crystallite size in the direction perpendicular to the plane of the films is obtained using the Scherrer equation[149], 36.1 nm at 400 °C and 20.9 nm at 450 °C illustrates that as the temperature increases the grain size become smaller and more crystalline.

$$D = \frac{0.94\lambda}{\beta \cos\theta}$$

where λ is the X-ray wavelength, θ the Bragg angle and β the FWHM of the diffraction peak.

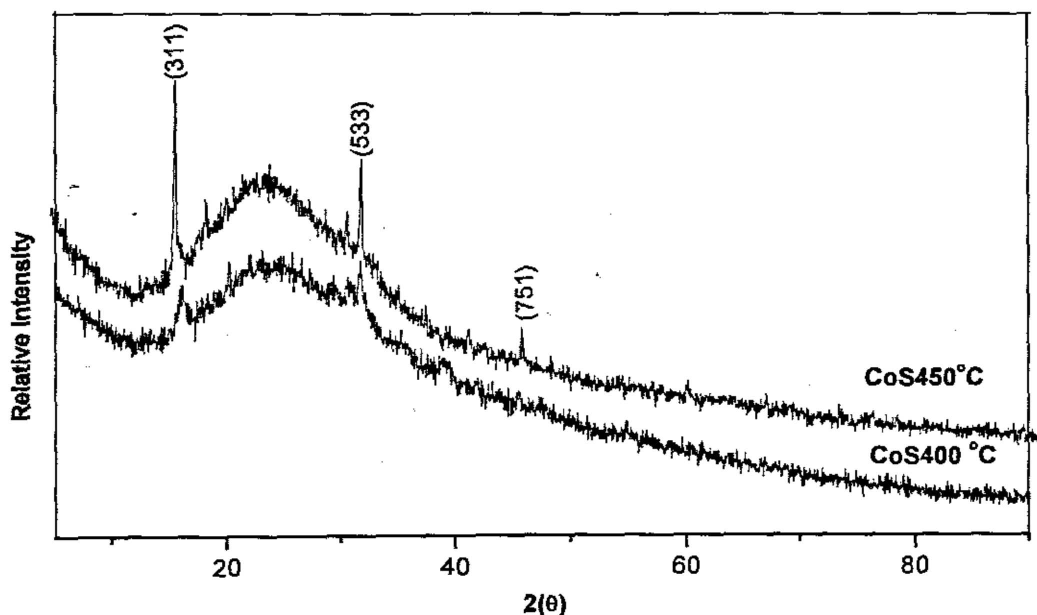

Figure 3.4: XRD patterns for cobalt sulphide (Co_3S_4) from complex [II].

The three dimensional morphology of the films was studied by scanning electron microscopy (SEM). At lower temperatures the morphology studies of the film deposited in the range of 250-300 °C revealed aggregates of granulated spheres. An increase in temperature to 400 °C facilitates more granulated spheres (Figure 3.5). The SEM images show that these spheres do not adhere to any pattern of deposition but merely form non-uniform distributions of spheres. This observation is evident at the surface regions of the substrate where growth of smaller spheres is initiated followed by, the formation of larger granulated spheres at higher temperatures. This is expected due to the kinetics of the particles and their thermodynamic growth when exposed to intense heat at higher temperatures, facilitating the rate of expansion of these spheres.

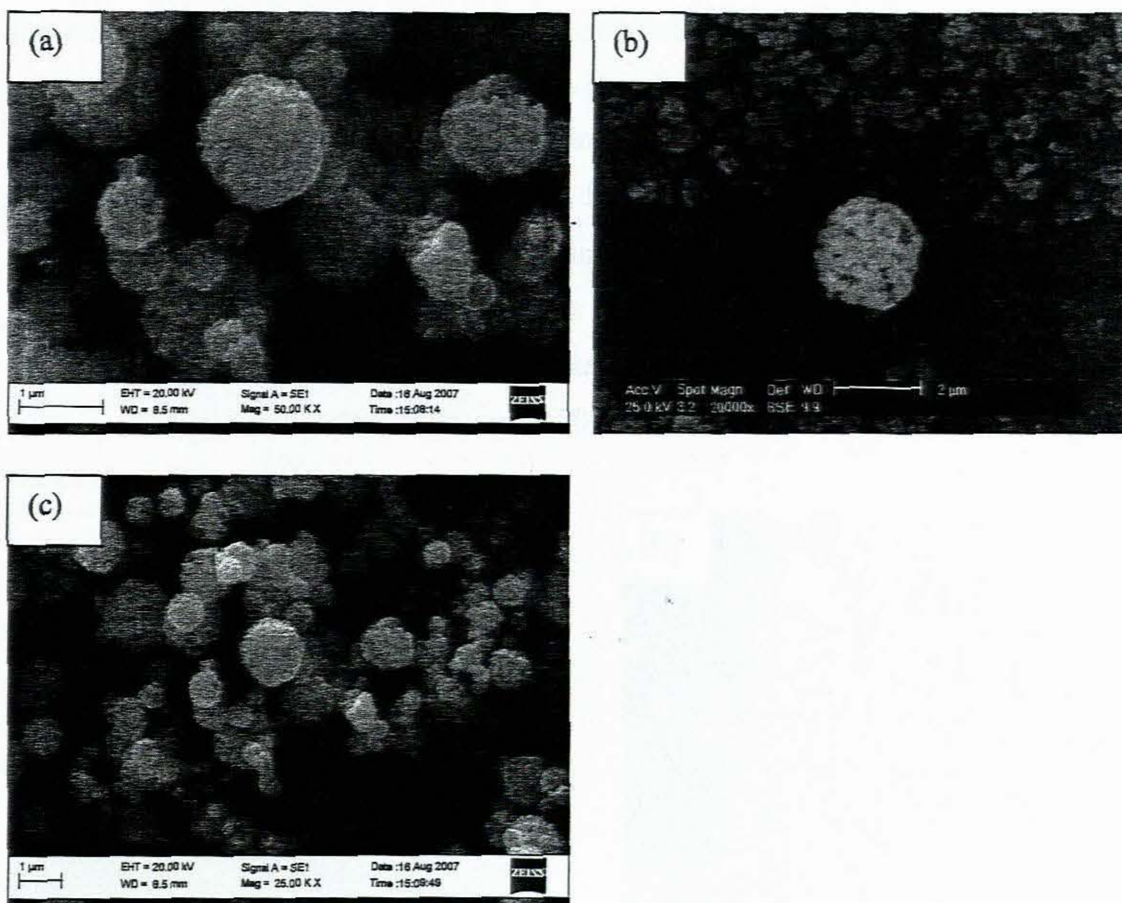

Figure 3.5: SEM micrographs of CoS from [II] at (a) 400 °C, (b) 300 °C showing the formation of granulated spheres and (c) CoS at 400 °C showing non-uniform distributions of spheres.

The EDAX pattern confirms the presence of cobalt and sulphur in *ca* 1:2 ratio in each case with the % Co = 38.40 and % S = 85.25, which is consistent with the XRD studies showing the CoS_2 phase.

It is notable that an increase in temperature affects the morphology of the films. An increase in the temperature to 450 °C shows the transformation of the granulated spheres to hexagonal or cubic crystallites through condensation (Figure 3.6). The lower part of the SEM micrograph in Figure 3.6b shows the migration of these spheres to form aggregates which upon heating infuse to form smoother spheres. In Figure 3.6c the condensation of these spheres is observed with a maximum infusion of particles to form cubic crystals. At a higher temperature of 500 °C the material deposited gets more crystalline, forming larger cubic crystals with the residual amorphous material left at the surface of the substrate (Figure 3.6d). It is evident from the results of CoS obtained from complex [II] that there is a change of morphology as well as the shape of the deposited material from a lower temperature of 250 °C, forming granules, to 300 °C – an increase in temperature facilitating the formation of granulated spheres, 400 °C – agglomeration of the granulated spheres to form non-uniform deposition, 450 °C – condensation of the granulated spheres to form small cubic material and, infusion of these condensates to form larger crystalline cubic shapes and 500 °C – formation of larger crystalline cubic material.

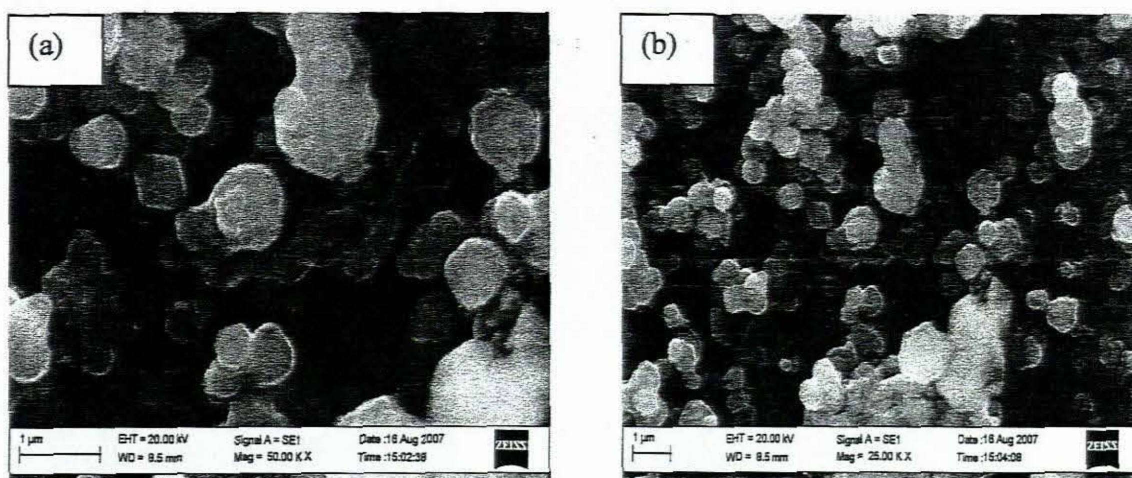

Figure 3.6: SEM micrographs of cobalt sulphide from [II] at 450 °C (a) slow condensation of spheres (b) formation of small cubes

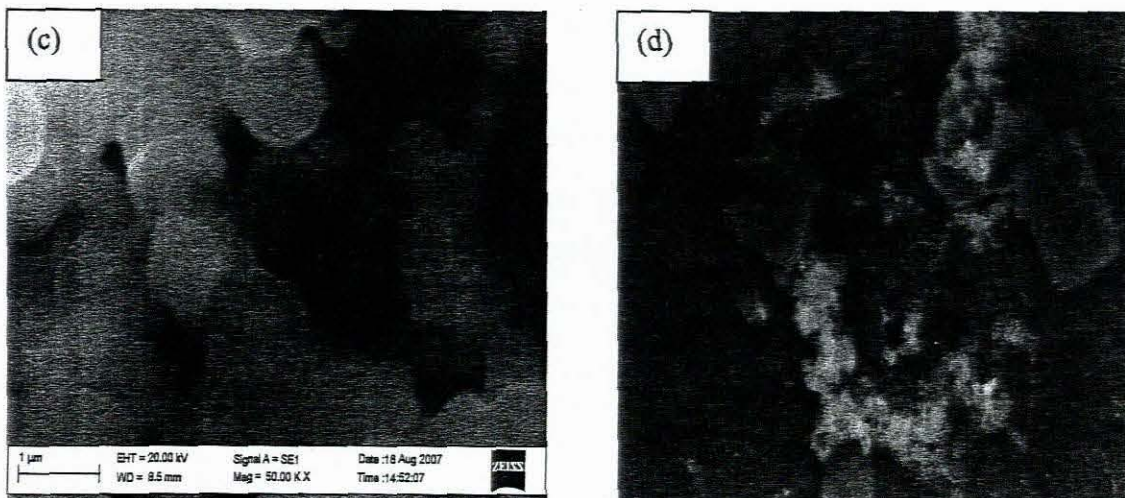

Figure 3.6: SEM micrographs of cobalt sulphide from [II] at 450 °C, contd. (c) condensation of granular spheres (d) cobalt sulphide at 500 °C forming larger cubic particles.

The morphology of the cobalt sulphide deposited from complex [I] shows that the nature of the substituted ligand can adversely affect the morphology of the film. This feature is observed in Figure 3.7 which shows the formation of poorly defined small, smooth and hollow irregular shapes. The morphology of these spheres is not defined due to the largely amorphous nature of these particles as confirmed by the XRD pattern in Figure 3.3.

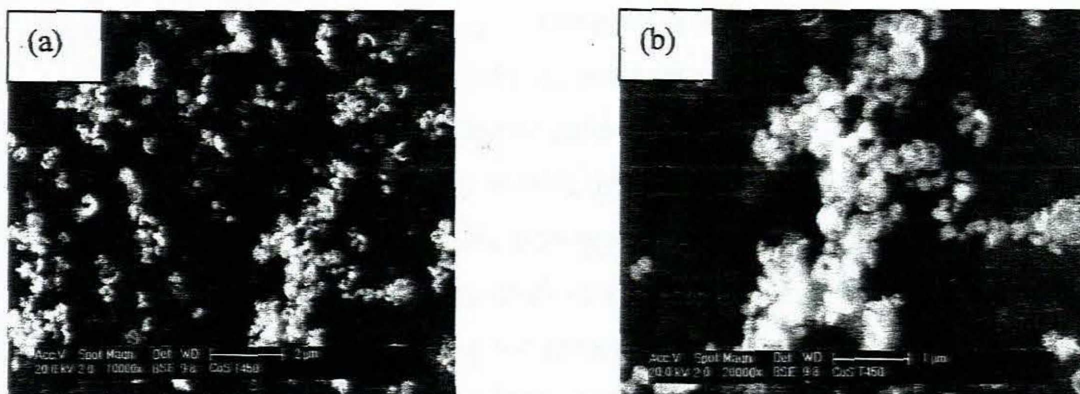

Figure 3.7: SEM micrograph of CoS from [I] (a) showing small irregular shapes (b) less crystalline aggregates of irregular shapes.

3.5.2 Optical Properties of the CoS Thin Films

The absorption spectra of cobalt sulphide from complex [II] shows a remarkably well defined spectrum at 450 °C relative to the film obtained at 400 °C. The optical band gap for the films grown at 450 °C and 400 °C were observed at 285 nm (4.35 eV) and at 323 nm (3.84 eV) respectively. The absorption band gaps are blue are shifted to a higher energy when compared with bulk cobalt sulphide, due to the small grain sizes of the material.

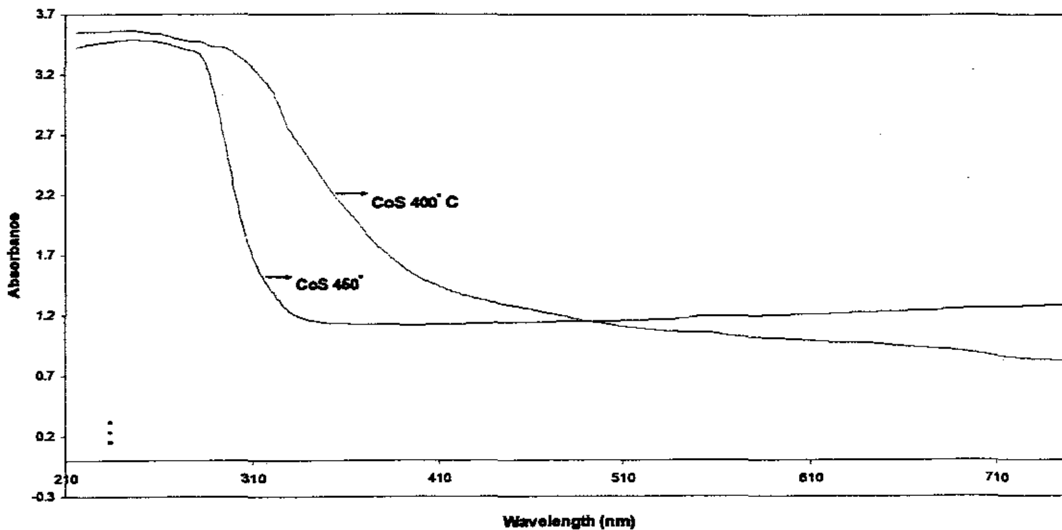

Figure 3.8: Optical absorption of CoS at 400 °C and 450 °C

3.5.3 Thickness measurements for the CoS thin films

The general growth mechanism is an assumption that a continuous thin and adherent layer or monolayer is initially formed, covering the entire substrate surface, which subsequently grows in a layer-by-layer pattern. However this is not the case for some metal sulphides which tend to exhibit non-uniform deposition, agglomerates and depending on the different condition parameters weak adherence on the substrates is often achieved. The particles are then sintered on the heated substrate, leading to the formation of porous films, with poor adhesion. Attempts were made in this study to optimize the adhesion properties of these films by using boat stubs to facilitate maximum adsorption of the vapour in depositing CoS thin films. These attempts proved to be a

success with the initially deposited film only forming porous films, due to the evaporated material escaping to the elevated areas of the glass reactor. The latter experiments gave uniform films with reasonable thickness of 12.26 nm.

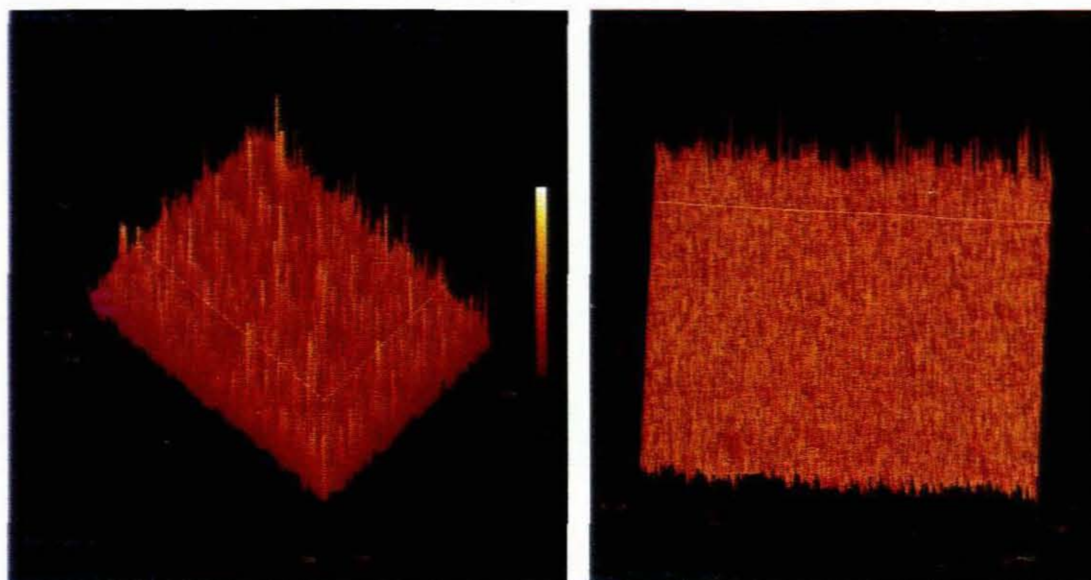

Figure 3.9.a: Surface morphology of CoS at 400 $^{\circ}$C (a) top view (b) alternate view

A notable feature as seen in Figure 3.9a (b) is that the surface of the film has a uniform distribution of deposited material and as the layer by layer accumulation of the film increases, a non-uniform distribution of particles is formed on the top as seen in Figure 3.9b (a).

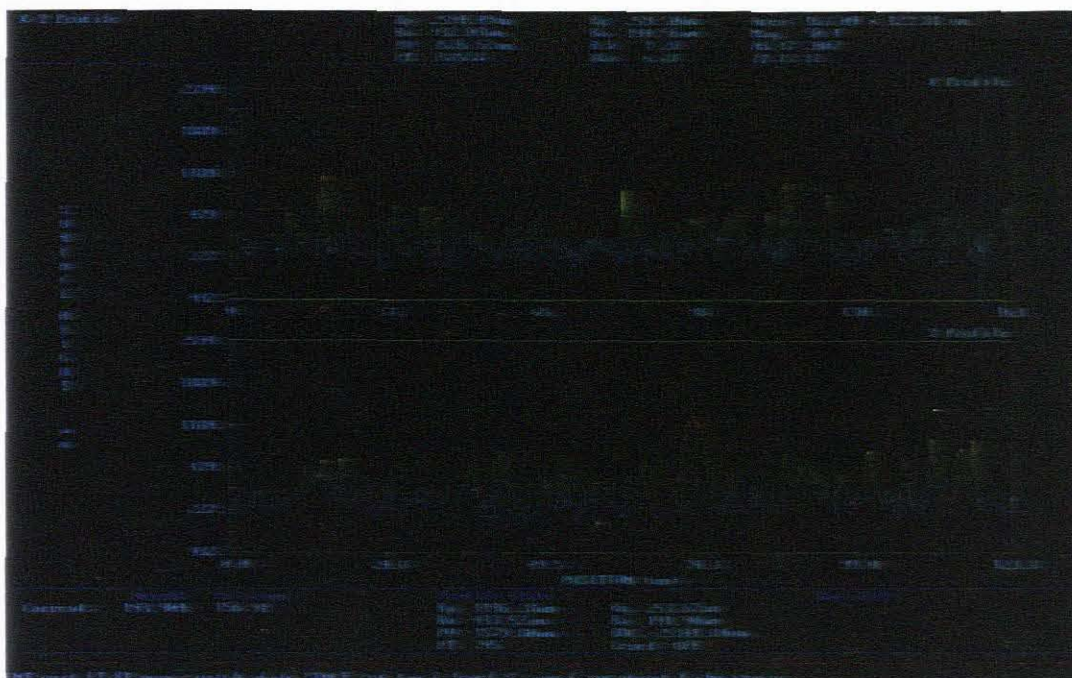

Figure 3.9b: Interference pattern of the CoS thin film deposited at 400 °C

The surface height spectrum shows an indication of relatively minimal irregularities with the maximum peak at 74.3 μm. The spectrum shows an average proportion of distribution in particles deposited.

3.5.4 Thermogravimetric analysis for Nickel Precursors

Different decomposition patterns for NiS complexes were obtained, with the major progression found to be that of 2-stage decomposition for these complexes (Figure 3.10). Complex [IV] shows a two step degradation profile with the first degradation step from 213-255 °C and the second minor stage from 255-310 °C resulting in a total weight loss of 80.77% and a residue of 19.23% which is shown in Table 3.4. The minor portion of the second stage is the decomposition of the thiourea breaking the C-S bond to leave the NiS.[150] All the thermograms start above 100 °C implying that there is neither water nor solvent molecule attached to the complex.

The TGA profile of complex [V] consists of one well defined stage of decomposition, an indication of high deposition due to its volatility. The defined stage starts 188-246 °C involving decomposition of the remaining organic moiety which constitutes approximately 94.86% leaving behind a negligible amount of residue.

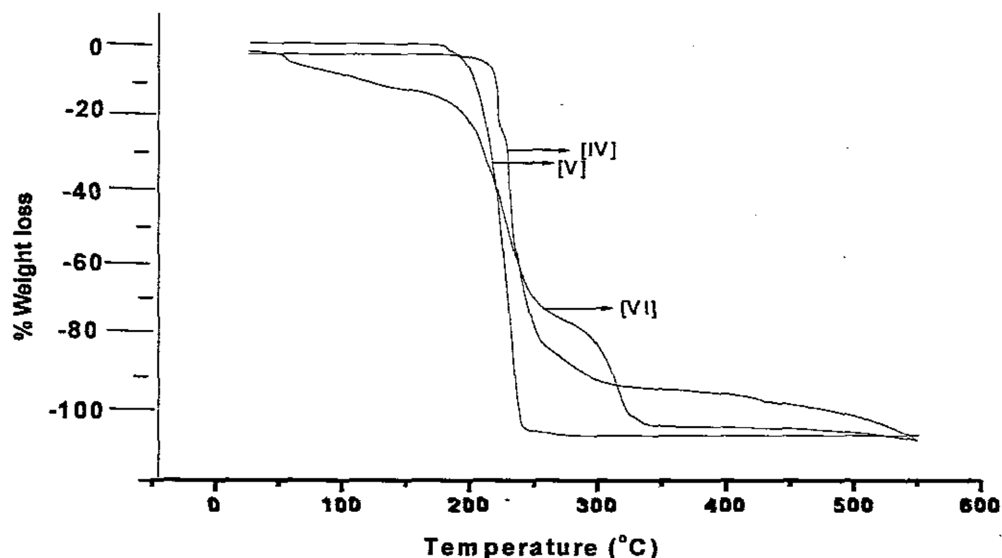

Figure 3.10: TGA spectra of Nickel complexes IV, V, VI

The presence of stoichiometric NiS was confirmed by their XRD patterns which showed the presence of NiS_2 (Figure 3.11). The XRD pattern of NiS does not show much crystallinity and exhibits two phases at 350 °C, a minor $Ni_{3-x}S_x$ phase and one prominent β-NiS_2 (pyrite) phase. After annealing the films at 400 °C the only distinguishable phase which remained was that of $Ni_{3-x}S_2$. Annealing removed the β-NiS_2 phase. The EDAX study done on these films confirms a higher % ratio of S relative to the Ni present in these films.

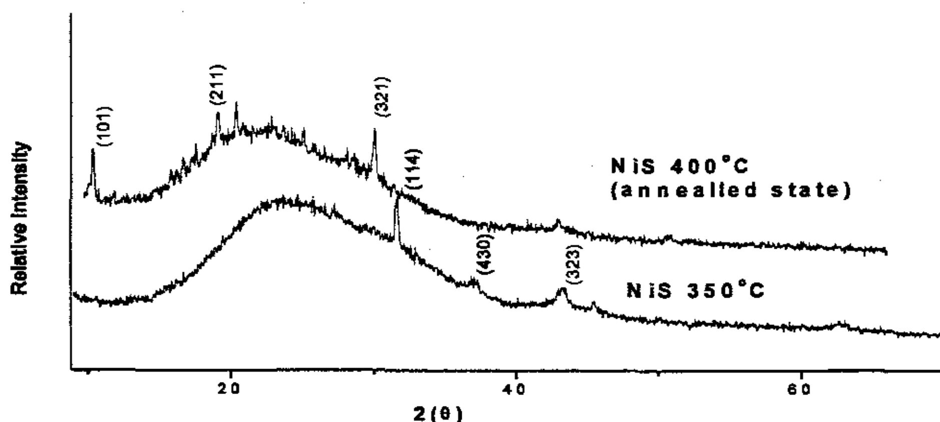

Figure 3.11: XRD pattern of NiS at 350 °C and 400 °C for $Ni_{3-x}Sx$ and NiS_2 from complex [IV]

In contrast to the NiS films obtained from [IV], the films deposited from complex [V] at 400 °C showed the presence of the predominantly NiS_2 (pyrite) phase with one peak (321) of α-$NiS_{1.97}$ (hexagonal) phase present (Figure 3.12). The nickel-sulphur phase diagram reported by Kullerund and Yund indicates that the α-β phase transformation takes place between 282 and 379 °C depending on composition, which is accompanied by ~ 4% volume change.[151] This follows several reports that the stoichiometric NiS crystallizes in two structures: the low-temperature rhombohedral (β-NiS, millerite) and the high-temperature hexagonal (α-NiS) crystal structures.[152,153] The grain size measurements obtained were 39 nm for NiS from [IV] at 350 °C and 22 nm for NiS from [V]. The films from complex [VI] were highly amorphous and their grain size could not be measured.

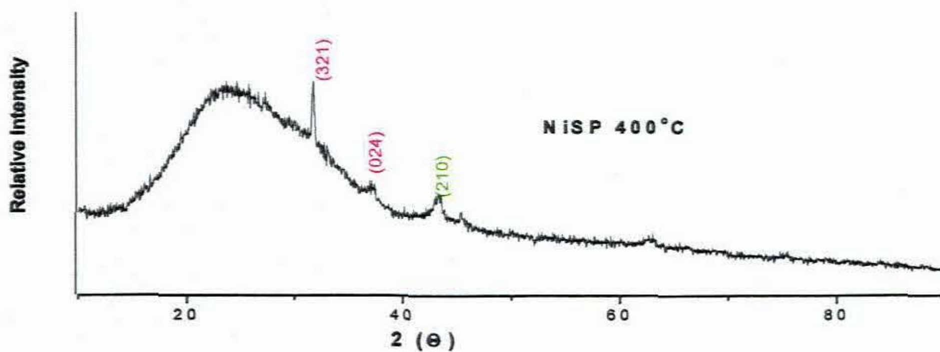

Figure 3.12: XRD pattern of NiS at 400 °C exhibiting a mixture • NiS_2 and • $NiS_{1.97}$

To enhance crystallinity in these films deposition on GaAs (100) was undertaken with a considerably small lattice mismatch of the GaAs relative to the film. In this case the predominant phase was found to be $Ni_{3-x}S_2$ with $NiS_{1.97}$ also present and one peak in the direction of (531) to be of NiS_2 (Figure 3.13).

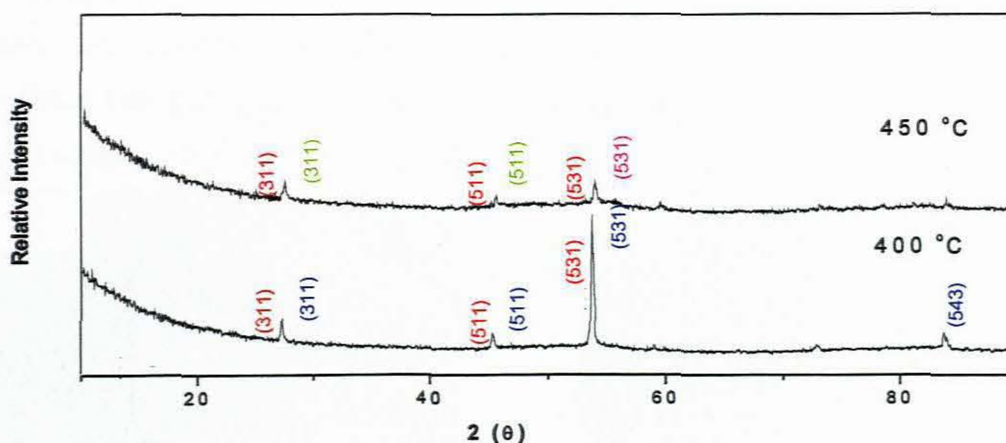

Figure 3.13: XRD pattern of NiS deposited from GaAs substrate

Table 3.2: XRD JCPDS data for NiS and GaAs

NiS_2 80-0375[150]			$Ni_{3-x}S_2$ 14-0358			$NiS_{1.97}$ 83-0575		
hkl	d(lit)/Å(%)	d(exp)Å	hkl	d(lit)/Å(%)	d(exp)	hkl	d(lit)/Å	d(exp)Å
321	1.4605(18)	1.4638	101	4.130(22)	4.1681	311	1.711(56)	1.6951
024	1.269(12)	1.2591	211	2.294(25)	2.2468	222	1.638(20)	1.6272
210	2.5131(50)	2.5042	114	1.5110(60)	1.5112			
430	1.1239(3)	1.1132	323	1.0500(35)	1.0809			
			321	1.5012(18)	1.4659			

GaAs 32 - 0389		
Hkl	D(lit)/Å	d(exp)
511	1.0818(18)	1.0792
531	0.9546(17)	0.9531

The morphology studies of the NiS deposited from [IV] at 350 °C showed initial growth in the shape of a star-fish rod as seen in the SEM micrographs shown in Figures 3.14a and 3.14b. At 400 °C a remarkable clearer view of the star-fish rods, with the outgrowths of these rods arising from a central point forming a star-fish arrangement. (Figure 3.14c). In micrograph (d) shows the length of these rods *ca.* 52 μm extensions.

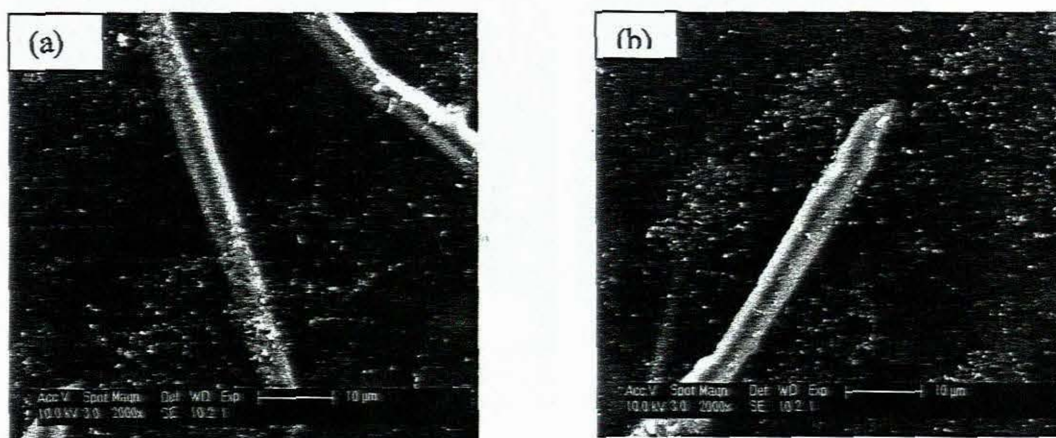

Figure 3.14: SEM micrographs of NiS from [IV] (a) initial-growth at 350 °C, (b) petrusion of rod-like structures

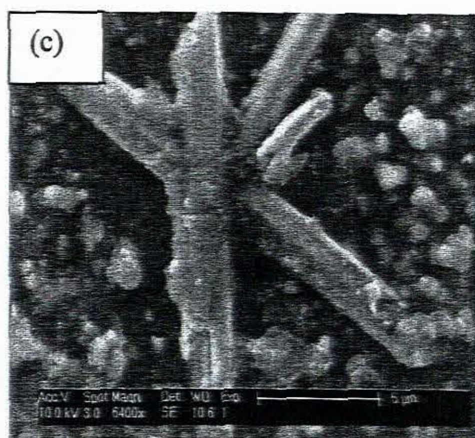

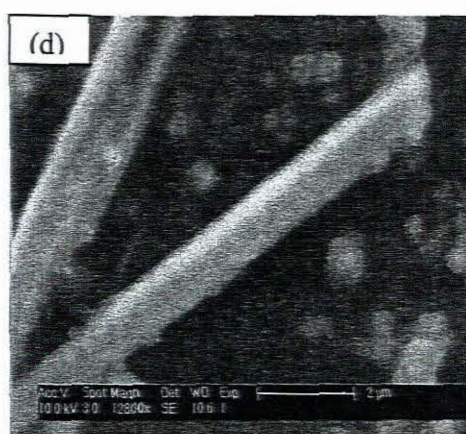

Figure 3.14: SEM micrographs of NiS from [IV], contd (c) NiS at 400 °C showing star-fish rods, (d) extension of the rod.

The morphology of films obtained at 400 °C from complex [V] showed the formation of granules as well as spheres with a predominance of spheres on the surface of the film (Figure 3.15). The granules are then formed into non-defined cubes as seen in Figure 3.13b with spheres at the surface.

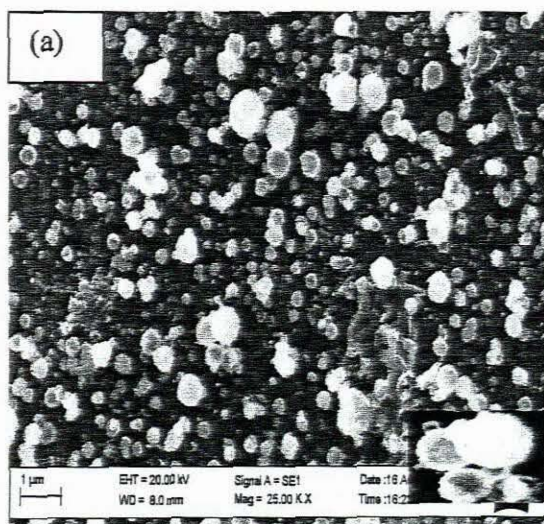

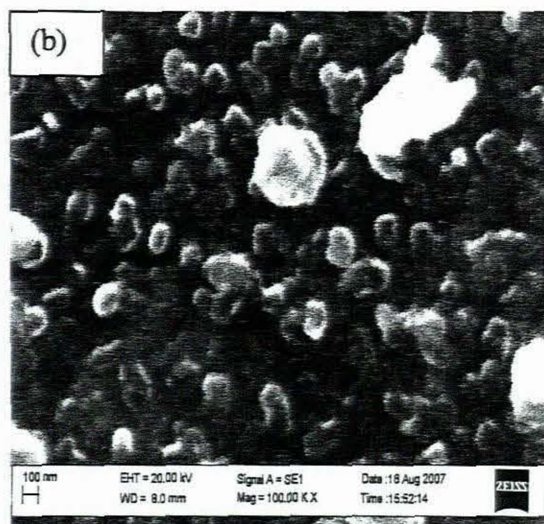

Figure 3.15: (a) Plain view of film grown from [V] at 400 °C showing the presence of spheres (b) granules forming cubes

The morphology of the film deposited from [VI] showed the presence of spheres at the surface of rod-like outgrowths. An assumption was made from the observation therein, that the spheres formed from these rod-like structures after exposure to immense heat as they appear highly crystalline than the latter rods.

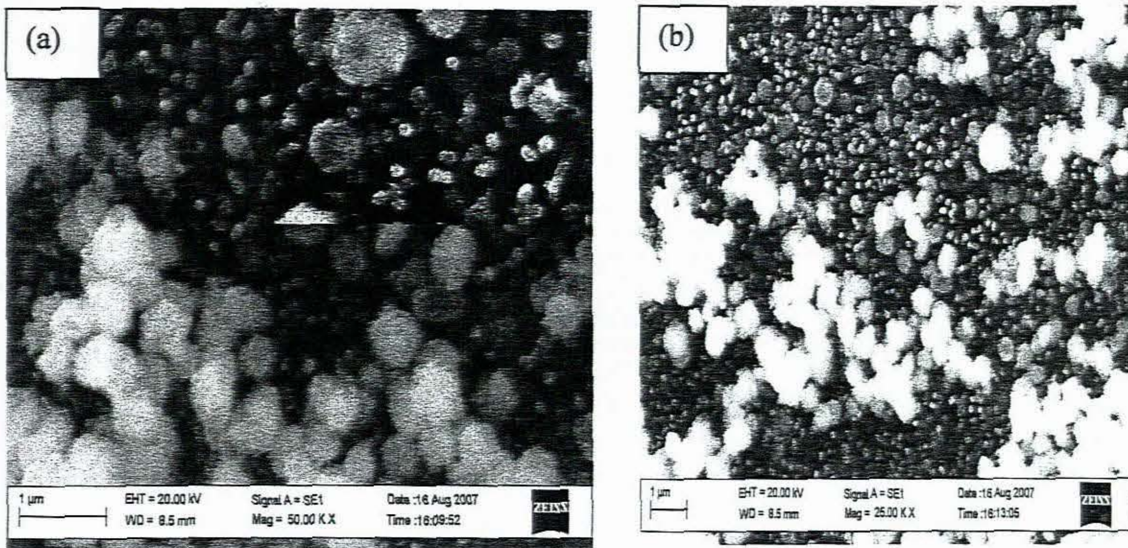

Figure 3.16: SEM micrographs (a) spheres and rod-like elements (b) heterogeneous uniform deposits of spheres and rod-like elements.

3.5.5 Optical Properties of NiS thin films

The UV-Vis spectrum of NiS thin films was found to exhibit blue-shifted absorption spectra in relation to bulk NiS. The optical band gaps were found to be at 284 nm (5.12 eV) for deposition at 400 °C and 242 nm (4.36 eV) for deposition at 450 and 500 °C respectively. These band gap energies were higher than bulk NiS (E_g = 2.1 eV[154]). The higher energy band gaps in contrast to that of bulk, is due to the small dimensions of the rod-like structures. Hence it was observed that an increase in temperature shifted the spectra to shorter wavelength causing a blue-shift in their wavelength.

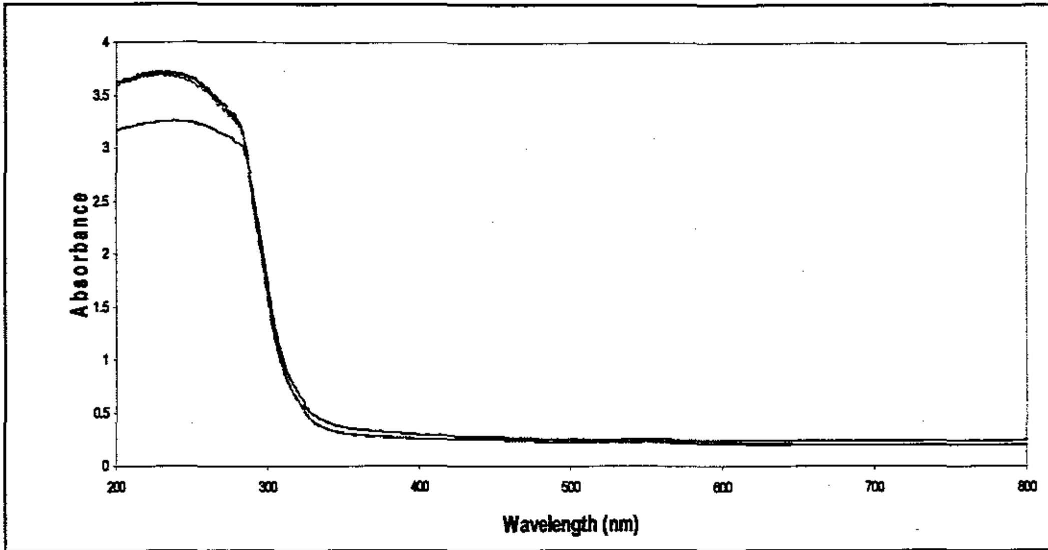

Figure 3.17: Optical properties of NiS at • 400 °C • 450 °C and • 500 °C

3.5.6 Thickness measurements for NiS thin films

Thickness measurements obtained from NiS using the following relation:

$$h = \frac{\Delta l}{l} \qquad (3)$$

Where l is the distance between 2 neighbouring fringes, h is the height of the deposited film and Δl-interference fringe displacement. The thin film in Figure 3.18a (400 °C) was found to be 8.08 nm in thickness with some contours and valleys where minimal aerosol was able to reach the substrate, by contrast the film deposited at 450 °C was 11.56 nm in thickness, very uniform with minor irregularities.

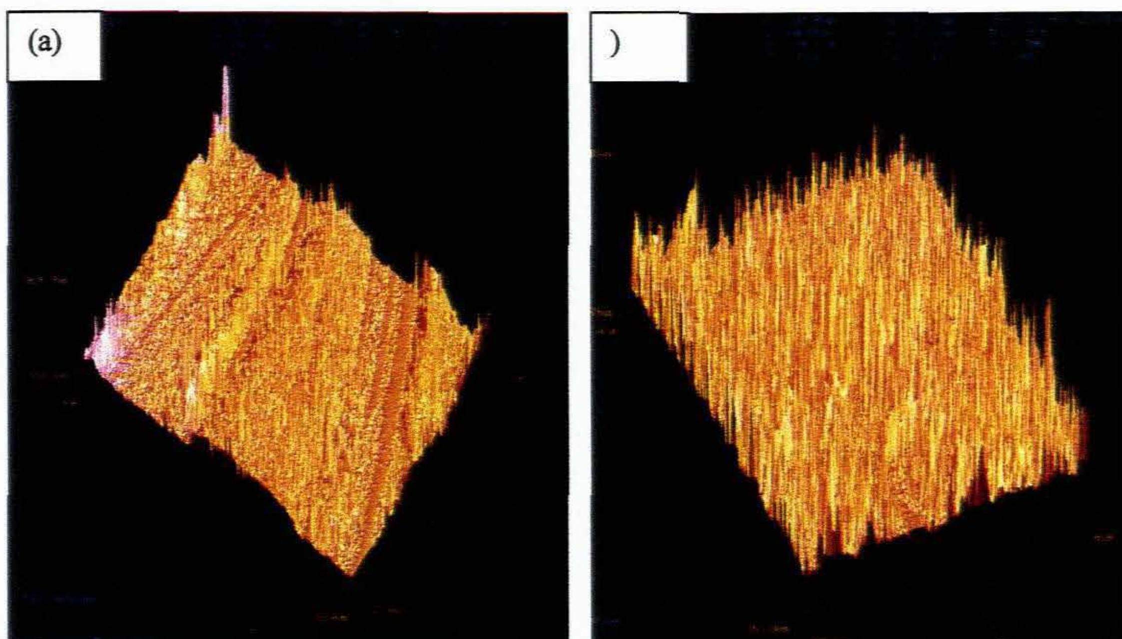

Figure 3.18: Surface morphology of NiS films (a) 400 °C and (b) 450 °C

3.5.7 Thermogravimetric analysis of Manganese Precursors

The TGA profile for the manganese alkylthiourea complexes comprise of poorly defined stages of decomposition. The thermogram obtained from complex [VII] exhibits a one step decomposition pattern from 210-401 °C resulting in a total mass loss of 69.81%. The thermogram of complex [VIII] shows a two step decomposition progression with a total mass loss of 69.02%, from 245-327 °C leaving behind the respective metal sulphide. The thermograms of manganese complexes showed less volatility than those from other complexes and hence, did not produce the expected thin films. This intricate volatilisation is also shown from the amorphous XRD pattern obtained from these films of MnS.

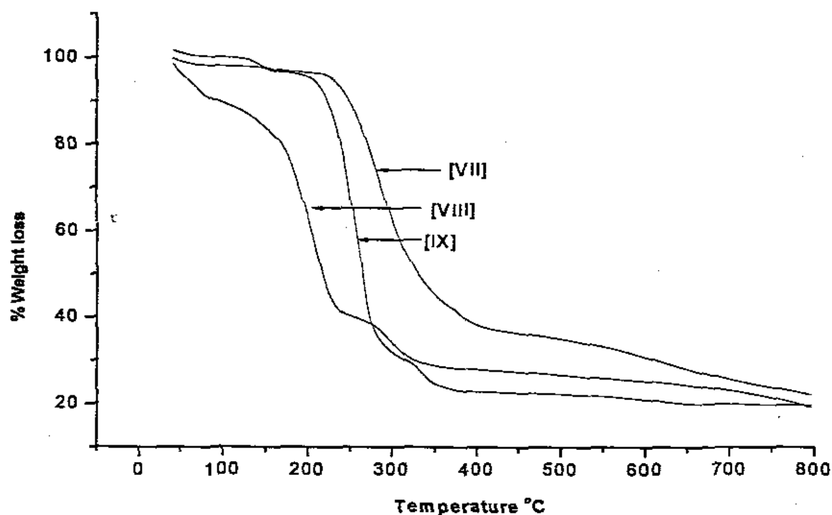

Figure 3.19: TGA curves of manganese complexes VII, VIII, IX

Almost all the thin films obtained from the deposition of MnS appeared to be highly amorphous, with the most favourable results obtained from the deposition of MnS at 450 °C. MnS obtained from complex [VII] shows the presence of 2 small peaks within an amorphous environment with the direction of orientation in Figure 3.20 found to be (102) and (713) indexed as α-MnS (Alabandite) phase.

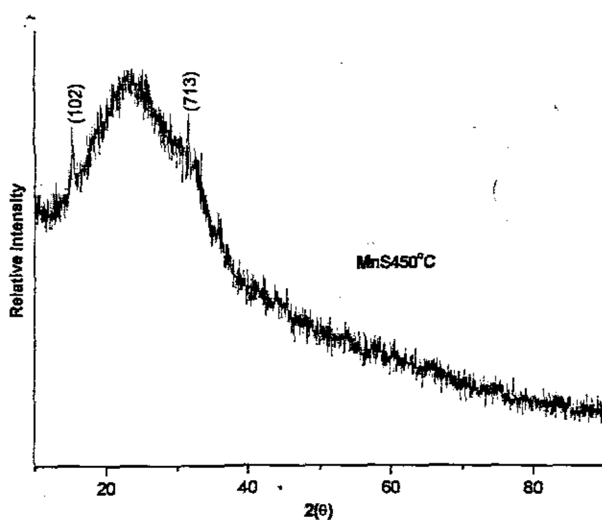

Figure 3.20: XRD pattern of MnS at 450 °C

Table 3.3: XRD JCPDS data for MnS

MnS JCPDS FILES 08-0247[148] & 40-1289[147]		
hkl	d(lit)/Å (%)	d(exp)/Å
102	2.3540(21)	2.8856
713	1.4610(5)	1.4601

The surface morphology pattern of MnS deposited at 300 °C illustrates a non-uniform distribution of polycrystalline growth of thin film. Polycrystalline growth involves nucleation at different substrate sites and then leading to growth of islands, coalescing to form a polycrystalline layer. Polycrystalline irregular growths are observable in (Figure. 3.21). Although the morphology of these growths is not well defined they appear to be rather crystalline.

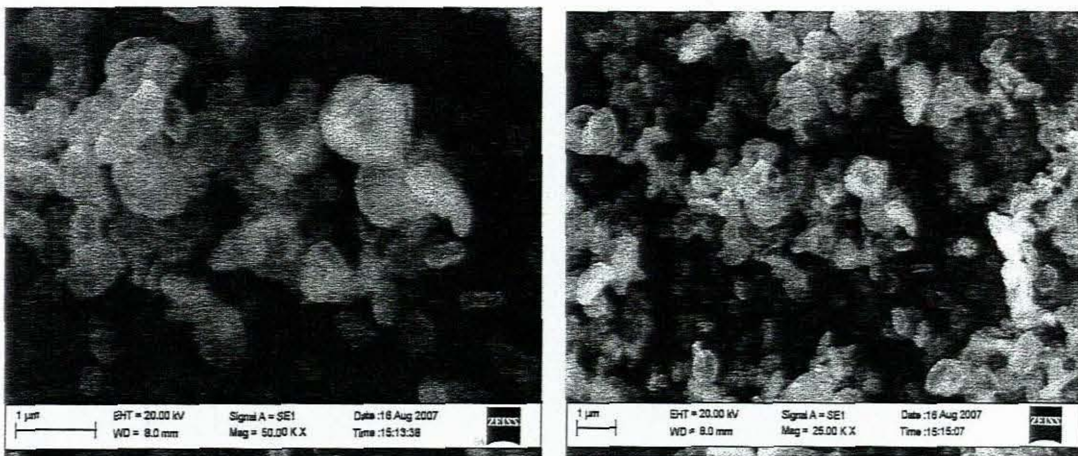

Figure 3.21: SEM micrographs of MnS deposited at 300 °C

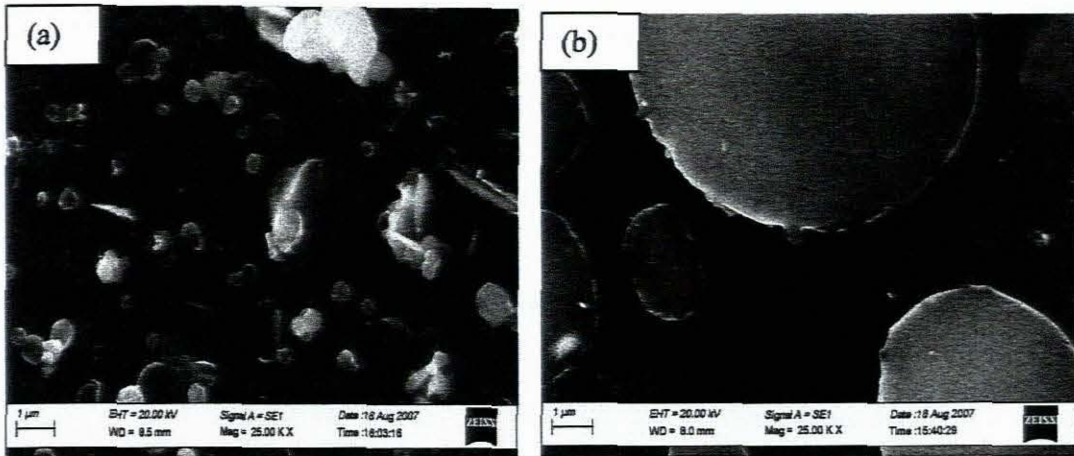

Figure 3.22: SEM micrographs of MnS deposited at (a) 400 °C, (b) 450 °C

At higher temperature the morphology changes where in (a) polycrystalline granular elements condense to take another orientation in (b) at 450 °C full condensation of these particles facilitates the formation of round-platelets like elements.

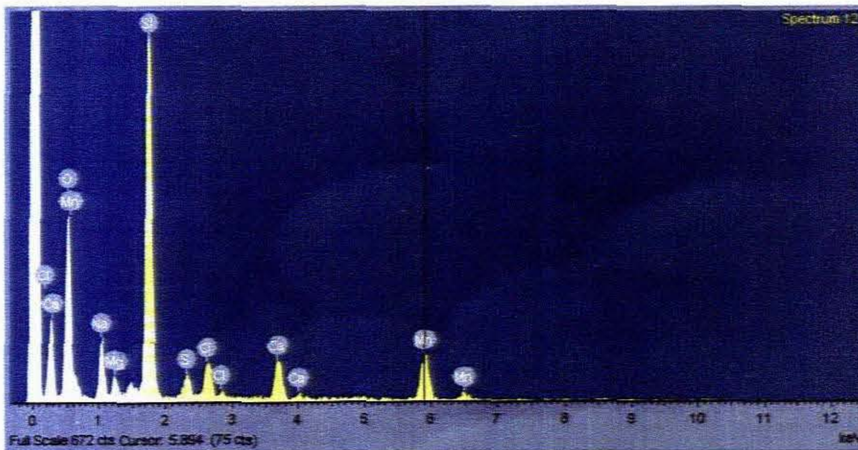

Figure 3.23: EDAX spectrum illustrating the ratio of MnS

The EDAX and the XRD spectra also confirmed the presence of MnS with the ratio being % Mn = 75.92 and % S = 24.08 respectively. The other constituents in the spectra are attributable to the glass components of the substrate.

3.5.8 Optical Properties of MnS thin films

The absorption spectra for the MnS thin films grown at 350 and 400 °C are shown in Figures 3.24 and 3.25 respectively. The band gap for the manganese sulphide is observed at 3.7 eV.[155] In this study the band gap energy was observed to be at 4.37 eV (350 °C) and 4.41 eV (400 °C). These observations shows a blue shift to higher energy in the spectra which is in contrast to the bulk, this could be explained by the small dimensions of the morphology of these films.[156] The difference in band gap energy for the materials deposited at different temperatures show a slight shift to higher energy (0.04 eV from 350-400 °C) with an increase in temperature (Figure 3.25).

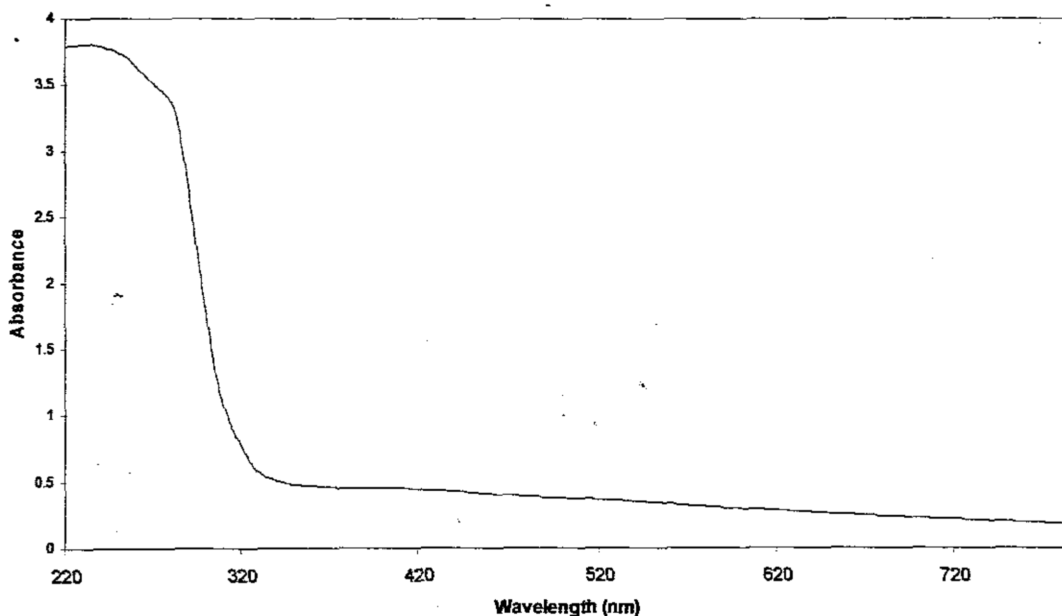

Figure 3.24: Absorption spectrum of MnS thin film deposited at 350 °C

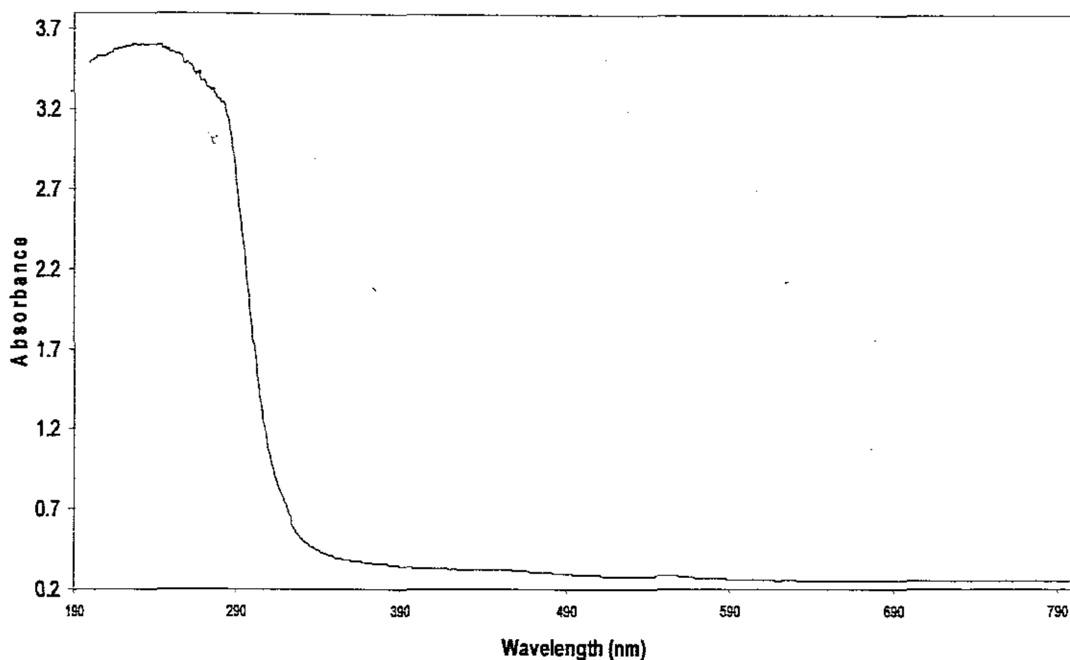

Figure 3.25: Absorption spectrum of MnS thin film deposited at 400 °C

3.5.9 Thickness measurements for MnS thin films

Thickness measurements of MnS as shown in Figure 3.26 illustrate minimal deposition with a lot of discontinuities and contours. This was due to the lack of adhesion of MnS to the substrate owing to the nature of the precursor, nevertheless attempts made allowed reasonable deposition of this precursor. The thickness was found to be 102.13 nm for the respective MnS thin film. The interference pattern of MnS in Figure 3.27 shows the peak contributed by the discontinuity of the film, the rest of the surface shows less irregularities giving a non-uniform distribution of the deposited material to the substrate.

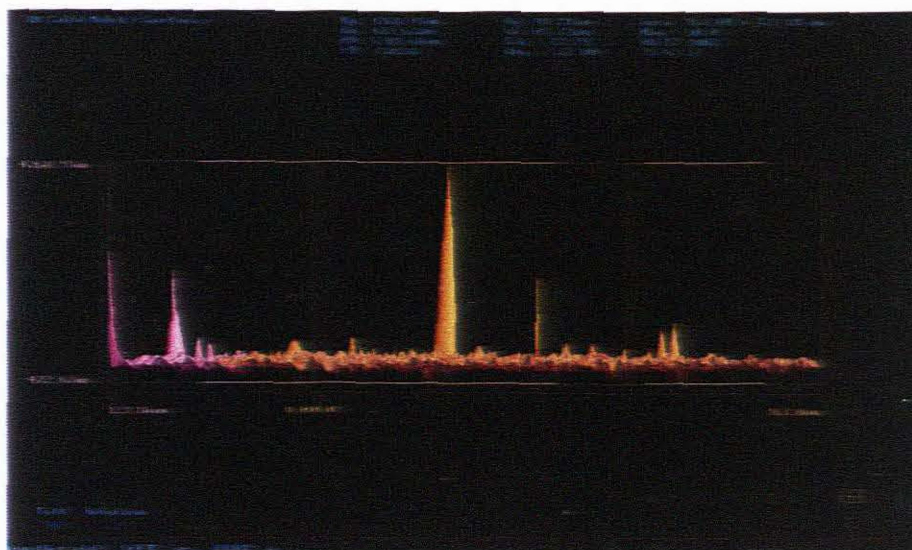

Figure 3.26: Surface morphology of MnS film at 400 °C

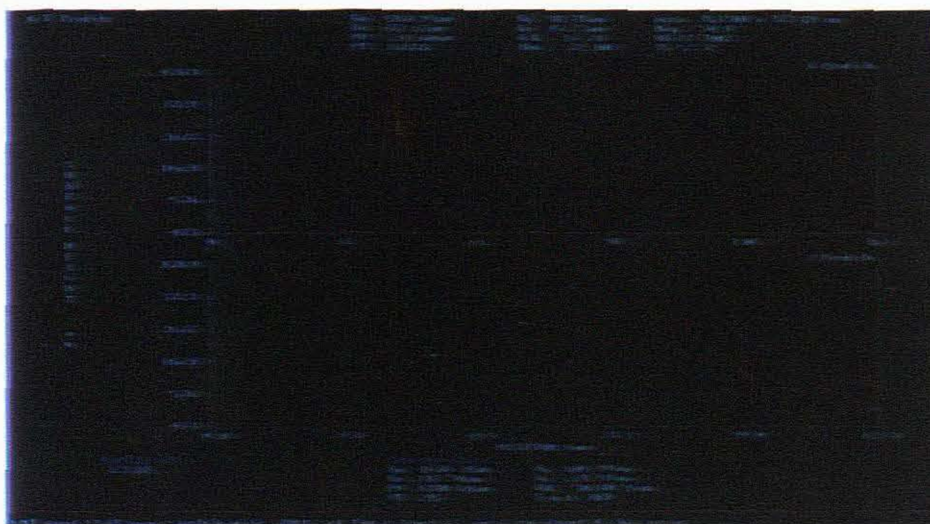

Figure 3.27: Interference pattern of MnS at 400 °C

3.5.10 Thermogravimetric analysis for Cadmium Precursors

The TGA profile for the cadmium complexes has well defined decomposition stages. All the thermograms start well above 100 °C implying an absentia of water or solvent

attached to the complex. Whereas, for complex [X] it has a 2-stage profile with a total mass loss of 77.12% leaving a negligible residue as seen in Table 3.4. The TGA profile of complex [XI] has 3-stage decomposition, with a total mass loss of 59.98% leaving a respective metal sulphide residue of 40.02% with a negligible difference of 2.58% from the theoretical. Lastly the TGA profile of complex [XII] show 2-stage decomposition with a total mass loss of 84.18%. These thermograms and their decomposition stages indicate stability but slow volatilization due to the many steps required for decomposition.

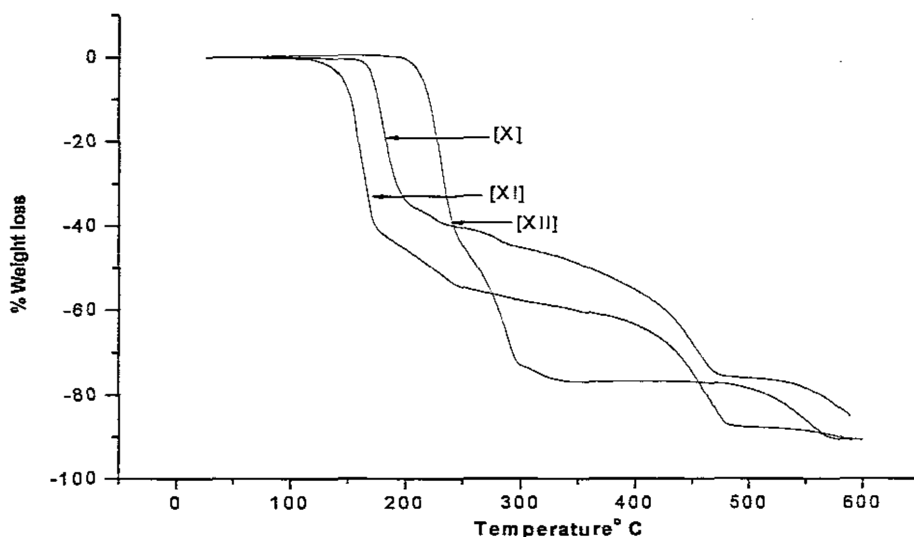

Figure 3.28: TGA graph of cadmium complexes X, XI and XII

Table 3.4: The summary of TGA data for complexes I-XII

Precursors	Stages of decomposition	% Total of material Loss (0 - 400 °C)	Experimental MS % residue	Theoretical Residual % MS
$[CoCl_2(CS(NH_2)_2)_2]$ [I]	1-stage	52.05	47.98	43.63
$[CoCl_2(CSNHC_6H_5NH_2)_2]$[II]	2-stage	61.17	38.83	28.35
$[CoCl_2(CSNHC_6H_{11})_2)_2]$ [III]	Less pronounced	76.40	23.60	20.17
$[NiCl_2(CS(NH_2)_2)_2]$ [IV]	2- stage	80.77	19.23	43.58
$[NiCl_2(CSNHC_6H_5NH_2)_2]$ [V]	1-stage	94.86	5.14	28.31
$[NiCl_2(CSNHC_6H_{11})_2)_2]$ [VI]	2- stage	78.54	21.46	20.14
$[MnCl_2(CS(NH_2)_2)_4]$ [VII]	1-stage	69.81	30.19	42.57
$[MnCl_2(CSNHC_6H_5NH_2)_2]$ [VIII]	2-stage	69.02	31.00	27.67
$[MnCl_2(CSNHC_6H_{11})_2)_2]$ [IX]	3-stage	79.46	20.54	19.63
$[CdCl_2(CS(NH_2)_2)_2]$ [X]	2-stage	77.12	22.88	52.61
$[CdCl_2(CSNHC_6H_5NH_2)_2]$[XI]	3-stage	59.98	40.02	37.44
$[CdCl_2(CSNHC_6H_{11})_2)_2]$[XII]	2-stage	84.18	15.82	26.58

The XRD pattern obtained from complex [XII] show a phase change from lower temperatures (300-350 °C) with a presence of 2 phases, hexagonal and orthorhombic, whilst at higher temperatures (400-450 °C) the cubic phase is predominant. Initially as can be seen in Figure 3.29 the XRD pattern of the films obtained at 250 °C appears to be amorphous. As the temperature increases there is a marked increase in crystallinity. The direction of orientation is found to be at (200), (220), (215) and (302) which correspond to the hexagonal phase and (012) and (211) for the orthorhombic phase which can be correlated to the JCPDS files in Table 3.5.

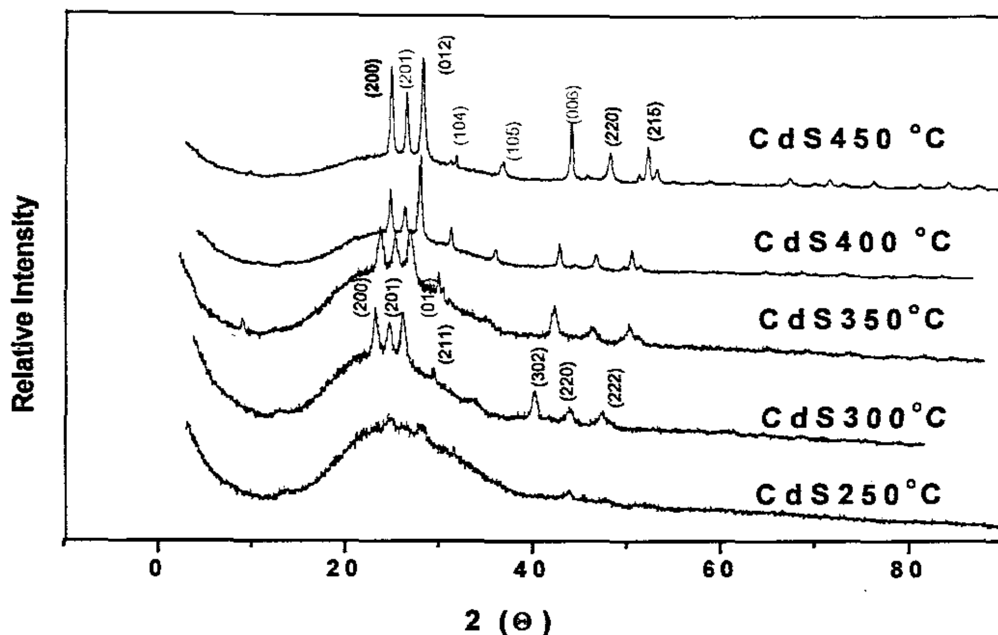

Figure 3.29: XRD pattern of CdS thin film *ca* (250-450 °C)

Table 3.5: XRD JCPDS data for CdS

CdS JCPDS FILES								
41-1049[141]			**43-0985[142]**			**75-1545[143]**		
hkl	d(lit)/Å	d(exp)/Å	hkl	d(lit)/Å	d(exp)Å	hkl	d(lit)/Å	d(exp)/Å
200	1.793	1.8124	012	1.6080(45)	1.6329	201	1.7329(25)	1.73476
220	1.0352(9)	1.0358	211	1.4700(33)	1.4673	105	1.2592(19)	1.26063
215	0.9543(30)	0.9544				006	1.1206(2)	1.1123
222	0.9893(16)	0.9833						
302	1.1262(20)	1.1121						

The morphology studies of the films obtained from complex [XII] showed a variation of crystallinity whereas initially at 250 °C an evidence of amorphous granules was observed. In Figure 3.30 micrograph (b) a formation of spore-like rods is observed, showing that the growth of these granules yield spore-like rods. These observations are different from those seen at 300 °C in Figure 3.31 with formation of cubic crystallites 0.95 µm.

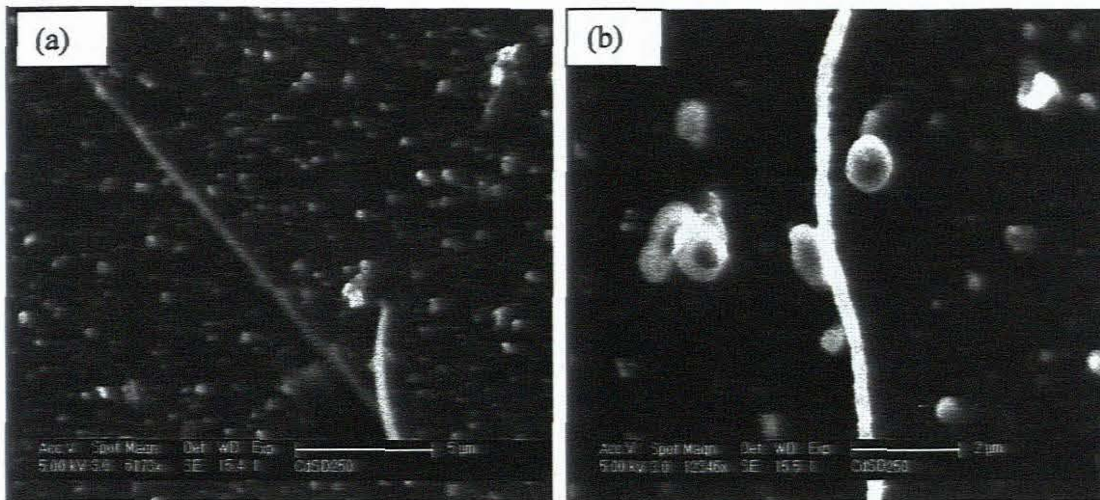

Figure 3.30: SEM micrographs of CdS deposited at 250 °C

Figure 3.31: SEM micrographs of CdS deposited at 300 °C

EDAX confirms the structural properties of these films which are comprised of % Cd = 51.43 and % S = 48.51, although the presence of cubic phase from the XRD pattern is only observed at 400 °C it was found to initially formed at 300 °C.

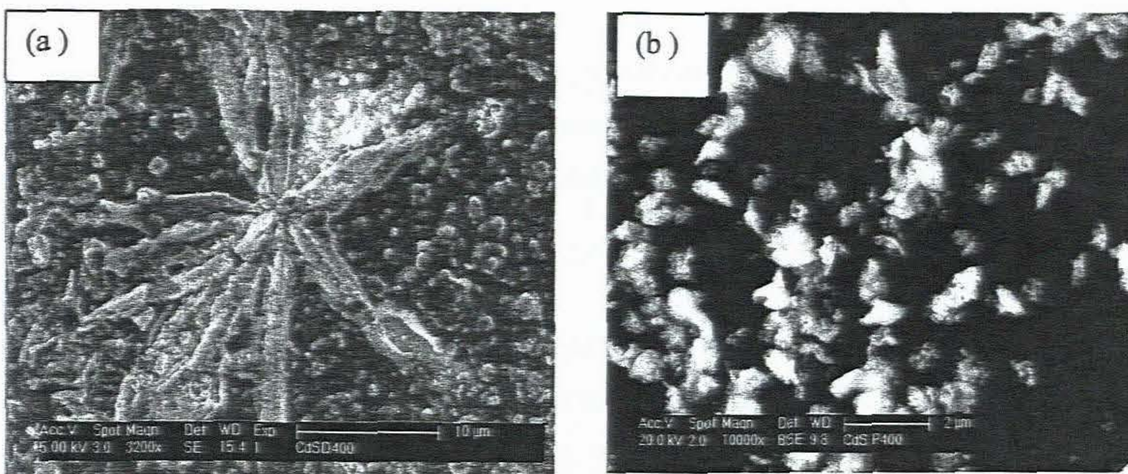

Figure 3.32: SEM micrographs of CdS (a) CdS at 400 °C from [XII] (b) CdS at 400 °C from [XI]

A correlation between the films deposited at the same temperature in Figure 3.32 was made to show the ligand has an impact in the resultant morphology of the deposited film. In micrograph (a) star-like rods formed from dicyclohexylthiourea ligand has a different morphology compared to that in (b) an island formation of crystallite deposited from the phenylthiourea ligand. Hence it is evident that the ligand substituent, the temperature and varying deposition parameters play a major role in the resulting morphology of the deposited film.

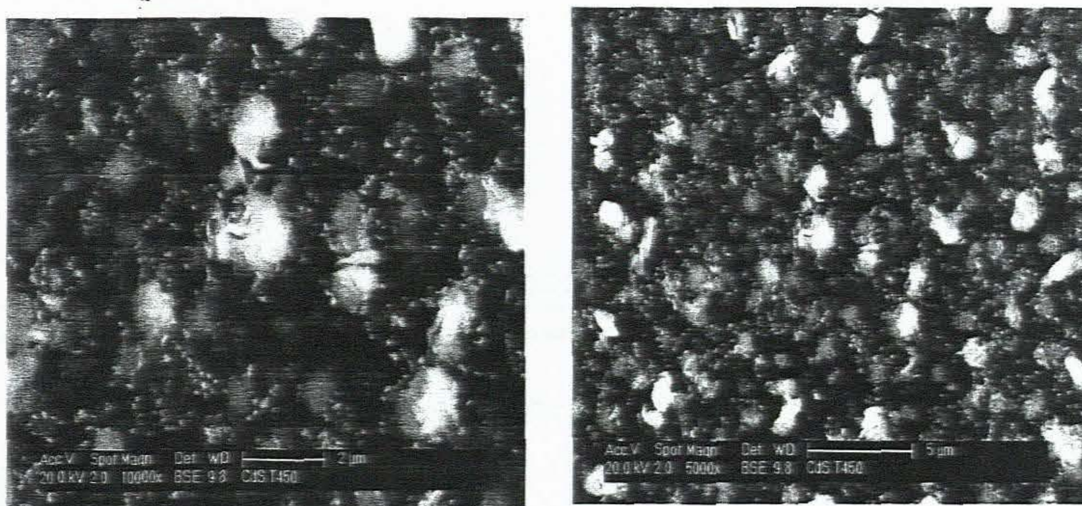

Figure 3.33: SEM micrograph of CdS deposited at 450 °C from [X]

The morphology of the deposited film from complex [X] showed a network of interconnected spherical crystallites, with a protrusion of somewhat cylindrical spheres (Figure 3.33). The grain size measurements were found to show variation as the temperature was increased at 300 °C (5.60 nm), 350 °C (5.93 nm), 400 °C (7.49 nm) and 450 °C (7.64 nm) respectively.

3.5.11 Optical Properties of CdS thin films

The absorption band edge (Figure 3.34a) of CdS obtained at 450 °C was observed to be blue-shifted in relation to the bulk material (2.42 eV)[157] with a wavelength of 478 nm (2.59 eV). The absorption spectrum (Figure 3.34b) of the films deposited at 450 °C shows a prominent shoulder with optical band gap energy of 2.48 eV slightly greater than that of bulk CdS which is 2.42 eV. The higher value than bulk band gap is indicative of quantum confinement effects brought about by the small grain size within these films. The optical properties of these films obtained in this present study compare well with thin films grown by chemical bath deposition.[158]

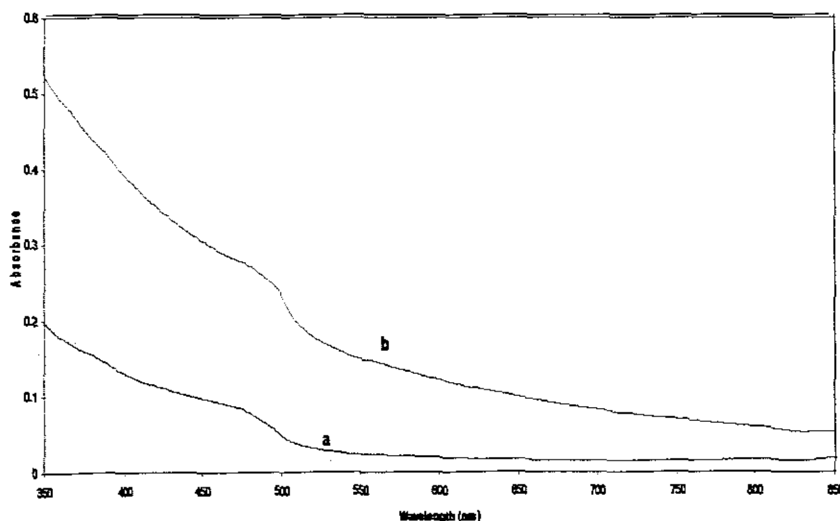

Figure 3.34: Absorption spectrum of CdS thin film (a) 400 °C (b) 450 °C

3.5.12 Thickness measurements of CdS thin films

The surface morphology observed for CdS at 400 °C in Figure 3.35 shows non-even distribution of the deposited material, although there was sufficient deposition of the film with film thickness of 46.78 nm. A thin film was deposited at 450 °C obtained to be 5.73 nm although it was a non-uniform distribution, this is illustrated in the interference pattern thereof with a lot of height peak of different wavelengths (Figure 3.36).

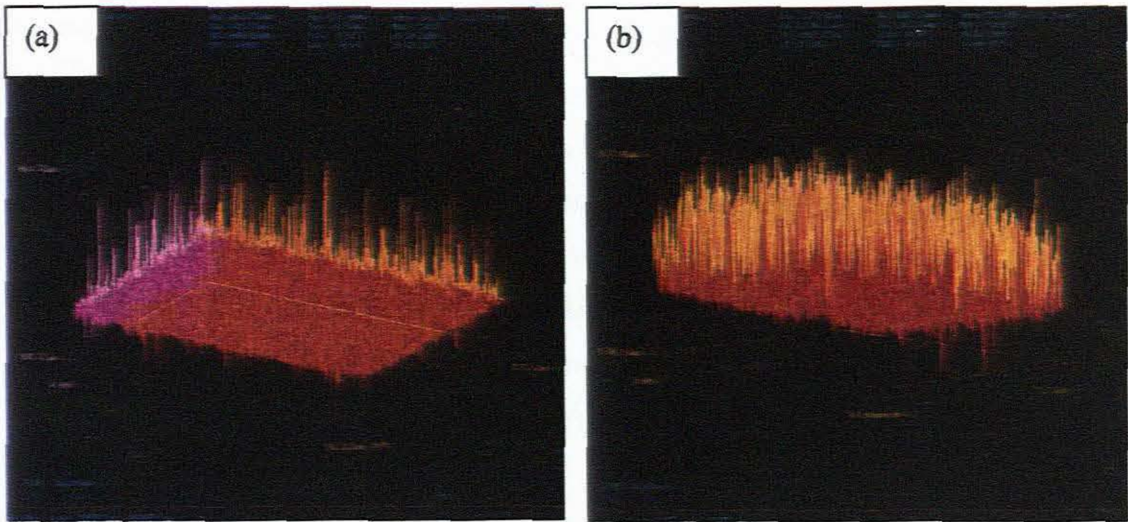

Figure 3.35: Surface morphology of CdS thin film (a) 400 °C (b) 450 °C

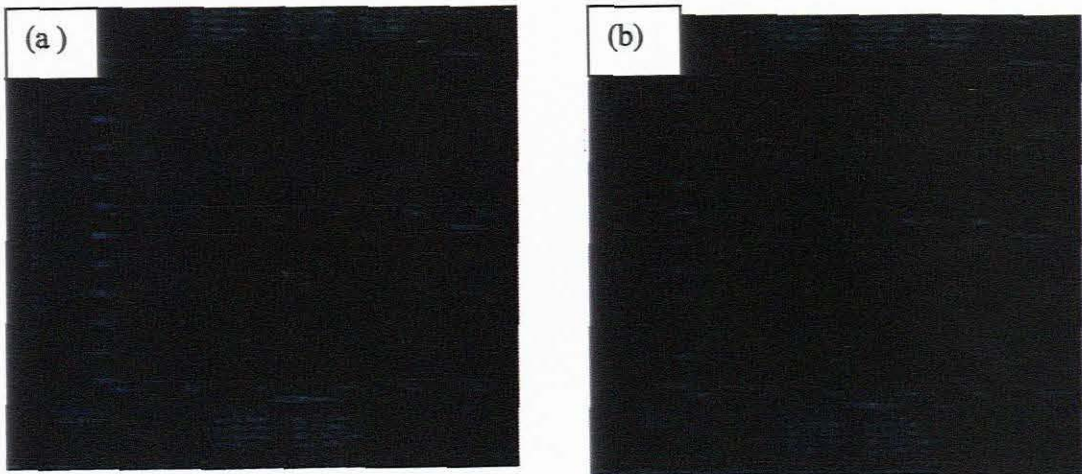

Figure 3.36: Interference pattern of CdS film (a) 400 °C (b) 450 °C

3.5.13 Conclusion

Thin film of Co_3S_4, CoS_2, CoS, $Ni_{3-x}S_2$, NiS_2, MnS and CdS have been successfully deposited using the AACVD technique and their optical properties studied. All films of CoS, MnS, NiS and CdS showed the blue-shifted wavelengths in their absorption spectra. The optical properties of all deposited films were found to deviate from the respective bulk metal sulphides. The XRD patterns of these thin films and their EDAX confirmed the expected structural properties. The influences of various deposition parameters such as temperature, flow rate and precursor concentration demonstrated optimal deposition of all the films. Temperature has the greatest effect, affecting both the grain size and the morphology of as deposited films. It is observed that a temperature increase tends to enhance mass transfer, resulting in shorter times needed to prepare the layer and in smaller grain size thereby facilitating layers that does not exhibit good adherence. Using boat stubs to elevate the substrate and controlling the various parameters such as flow rate as well as using different substrates for deposition enhanced adherence of as deposited films and their crystallinity.

REFERENCES

References

1. K. Badeker, *Ann. Phys. (Leipzig)* **22**, 749 (1907).
2. A. Rosenheim and V. J. Meyer, *Z. Inorg. Allgem. Chem.*, **49**, 13 (1906).
3. F.A. Cotton, O.D Faut and J.T. Mague, *Inorg. Chem.* **3**, 17 (1964).
4. H. Yoshida, H. Furubayashi, Y. Inque and T. Tanomura, *J. Vac. Soc. Japan* **19**, 13 (1976).
5. R. Latz, K. Michael and M. Schere, *J. Appl. Phys Japan,* **30**, L149 (1991).
6. G. Green and P. O' Brien, *J. Mater. Chem.,* **14**, 929-636(2004).
7. H. T. Tien and J. Higgins, *J. Electrochem. Soc,* **127**, 1475(1980).
8. G. Hass, J. B. Heaney and A. Toft, *Appl. Opt.,* **18**, 1488(1979).
9. N. Miura, T. Ishikawa, T. Sasak, T. Oka, H. Onatta, H. Matsumoto and R. Nakano, *J. Appl. Phys. Japan,* **31,** L46 (1992).
10. J.S. De Lodyguine, *Illuminant for incandescent lamps*, US patent 575002 (1893).
11. K.L Choy In: H.S Nalwa, *Handbook of Nanostructured Materials and Nanotechnology, Vol 1: Synthesis and Processing*, San Diego(CA): Academic Press: p. 533, (2000).
12. B.R. Kim, S.C Hwang, HG Lee, H.S Shin, *Korean J. Chem. Eng.*, **17**(5) 524-527 (2000).
13. Hayness, B.S, Hander, H. Wagner H.G.G In: 17th International Symposium on Combustion, Pittsburgh (PA) Combustion Institute,1365 (1979).
14. M.K Akhtar, S.E Pratsinis, S.V.R Mastrangelo, *J. Am. Ceram. Soc.*, **75**, 3408(1992).
15. L.G. Hurbert-Pfalzgraf, H. Guillon, *Appl. Organomet. Chem.*, **12**, 221(1998).
16. M. Glerup, H. Kanzow., R.Almairac, M.Castignolles, P. Bernier, *Chem. Phys. Lett.*, **377**, 293(2003).
17. K.L. Choy, in Handbook of Nanostructured *Materials and Nanotechnology, vol.1: Synthesis and Processing* (Ed. H.S. Nalwa), Academic Press, San Diego, CA, (2000).
18. A. Conde-Gallardo, N. Castillo, M. Guerrero, *J. Appl. Phys.*, **98**, 054908(2005).
19. T.T. Kodas, M.J. Hampden –Smith, *Aerosol Processing of Materials*, Wiley – VCH, Wenheim, Germany (1999).
20. M.H. Jin, K.K. Banger, J.D. Harris, A.F. Hepp, *Mater. Sci. Eng.*, **116**, 395(2005).
21. R.J. Lang, *J. Acoust. Soc. Am.*, **34**, 6(1962).
22. O, Renault, M. Laabeau, *J. Electrochem. Soc.*, **146**, 3731(1999).
23. A. Davies, N.E. Hudson, L. Pirie, *Med. Eng. Phys.*, **17**, 387(1999).
24. Basu P.K and P. Pramanik, *Mater. Sci. Lett.* **5**, 216(1986).
25. J.N. Smith, R.C. Flagan, J.L. Beauchamp, *J. Phys. Chem. A.*, **106**, 9957(2002).
26. A. Gomez, G. Chen., *Combust. Sci. Technol.*, **96**, 47 (1994).
27. X.H. Hou, K.-L. Choy, *Surf. Coat. Technol.*, **15**, 180(2004).
28. Yee Wee Koh, Chian Sing Lai, A Yan Du, *Chem. Mater.*, **15**, 4544 (2003).
29. A. M Bond, R.L Martin, *Coord. Chem. Rev.* **54**, 23(1984).
30. A.T. Kana, T.G. Hibbert, M.F. Mahon, K.C Molly, I.P. Parkin, L.S. Price, *Polyhedron* **20**' 2989(2001).
31. A.V. Ivanov, O.N. Antzukin, *Polyhedron,* **21**' 2727 (2002).
32. P. Mathur, A.K. Ghosh, S. Mukhopadhyayi, C. Srinivash, S.M. Mobin, *J. Organomet. Chem.,* **678**, 142(2003).
33. R. Pastorek, Z. Travnicek, E. Kvapilova, Z. Indelar, F. Brezina, J. Marek, *Polyhedron,* **18**, 3401 (1999).

34. R.B Hall and J.B Meakin, *Thin Solid films,* **63**, 203(1979).
35. J. Britt. and C. Ferekides *Appl. Phys. Lett.*, **62**, 2851(1993).
36. G. Blandenet, M. Court, Y. Lagrade., *Thin Solid Films*, **77**, 81(1981).
37. C.D Lokhande, A. Ennaoui, P.S Patil, M. Giersig, M. Miuller, K. Diesner and H. Tributsch, *Thin Solid Films,* **330**, 70 (1998a).
38. T.J. Coults, M.W. Wanless, J.S. Ward, S. Johnson *25th IEEE Photovoltaic Specialists Conference*, **25** (1996).
39. J. Cheon, D.S Talaga, J. Zink, *Chem. Mater.*, **9**, 1208(1997).
40. F. Maung, *Chem. Vap. Deposition*, **2**, 113(1996).
41. D.N. Coucouvanis, The precursors were prepared by reported methods: *Prog. Inorg. Chem.*, **11**, 233(1970).
42. R. Nomura, K. Kanaya and H. Matsuda, *Ind. Eng. Chem. Res.* **28**, 878(1989).
43. V.N. Semyonov, E.M. Averbach, L.A Michalyeva, *Zh. Neorg. Khim*, **24**, 911(1979).
44. K.V. Kerm, A.O. Tilling, J.A. Varvas, *Proc. Tallinn Tech. Univ.*, **479**, 101(1980).
45. W. M Kriven, *Mater. Sci. Eng. A.*, **127**, 249 (1990).
46. G.V. Samsonov, S.V. Drozdova, The Sulphides, *Metallurgiya*, Moscow, (1972).
47. K. Anuar, Z. Zulkarnain, N. Saravan, A. Zuriyatina, R. Sharin, *Mater. Sc.*, **10**, 157 (2004).
48. F. Jellínek, *Inorganic Sulphur Chemistry* (edited by G. Nickless), Elsevier p.669, (1968).
49. G. Brauer, *Handbook of Preparative Inorganic Chemistry*, 2nd edition. Academic Press, vols. 1, 2 (1963).
50. S. Furuseth and A. Kjekshus, *Acta. Chem: Scand.*, **19**, 1405(1965).
51. F. Hulliger, *Structure and Bonding,* **4**, 83(1968).
52. H. Wiedemeier and P.W. Gilles, *J. Chem. Phys*. **42**, 2765(1965)
53. M. Yoshimura, S.H. Yu., *Adv. Funct. Mater.* **12**, 277 (2002).
54. S. Sivaram, *Chemical Vapour Deposition: Thermal and Plasma Deposition of Electronic Materials*, van Nostrand Reinhold, New York, 1995.
55. A.C. Jones, *J. Mater. Chem.*, **12**, 2576(2002).
56. I.K. Igumenov, F.A. Kuznetsov and V.R. Belosludov; *Proc. Electrochem. Soc.*, **273**, 96(1996).
57. R.G. Gordon, *Proc. Electrochem. Soc.*, **13**, 248(2000).
58. C. Roger, T. Corbitt, C. Xu, D. Zeng, Q. Powell, *Nanostruct. Mater*, **4**,529(1994).
59. L.G. Hurbert-Pfalzgraf, H. Guillon, *Appl. Organomet. Chem.*, **12**, 221(1998).
60. M. Elphich, *Electronic Design*, **21**, 58(1975).
61. G.G. Stillman, C.M. Wolfe and T. Molngailis, *Appl. Phys. Lett.*, **25**, 36(1974).
62. M.G. Craford, *Prog. Solid. State Chem.*, **8**, 127(1973).
63. M.G. Craford, N. Holonyak, Jr, "In Optical Properties of Solids: New Developments", B.O Seraphin ed., North-Holland, Amsterdam, p. 187(1976).
64. D.G Thomas, *IEEE Trans. Electron. Dev.*, **18**,621(1971).
65. M.G. Craford, *IEEE Trans. Electron.*, **24**, 935(1977).
66. A.A. Bergh, P.J. Dean, "Light Emitting Diodes," Clarendon Press, Oxford, 1976.
67. H. Kressel, J.K. Butler, "Semiconductor Lasers and Heterojunction LEDs" Academic Press, New York, (1978).
68. H.C. Casey. JR., M.B. Panish, "Heterostructure Lasers", Academic Press, New York, (1978).

69. J.R. Carruthers in "Current Topics in Materials Science", E. Ikaldis, ed., vol. 3, North- Holland, Amsterdam, p. 463, 1979.
70. D. Botez, G.J. Herskowitz, *Proc. IEEE*, **68**, 689 (1980).
71. T. Izawa, H.Mori, Y. Murakami, *Appl. Phys. Lett.*, **38**, 483(1981).
72. H.J. Hovel, *Solar Energy Mater*, **2**, 277(1980).
73. H.J. Hovel, "Solar Cells", in "Semiconductors and Semimetals" (R.K Willardson and A.C. Beer, eds.0, vol. 11, Academic Press, New York (1975).
74. K.J. Bachmann, in "Current Topics in Materials Science, E. Kadis, ed., vol. 3, North – Holland, Amsterdam, p. 477, 1979.
75. P.A. Iles, *J. Vac. Sci. Technol.*, **14**, 1100(1977).
76. H. Kressel, P. Robinson, V.L. Dalal, *Appl. Phys. Lett.*, **25**, 197(1974).
77. J. Mimila- Arroyo, Y. Marfaing, G. Cohen- Solal, *Solar Energy Mater*, **1**, 171 (1979).
78. Y. Tawada, H. Okamoto, Y. Hamakawa, *Appl. Phys. Lett.*, **39**, 237(1981).
79. P. van Hallen, R. P. Mertens, R.J. van Overstraeten, *IEEE Trans. Electron. Dev.*, **25**, 507 (1978).
80. L.A. Ryabova in "Current Topics in Materials Science," vol. 7, North- Holland, Amsterdam, p. 587, 1981.
81. C.F. Powell and J.H. Oxley., eds, "Vapour Deposition," Wiley, New York, p. 277, 1966.
82. H.M. Manasevit, A. Miller, F.L. Morritz, and R. Nolder, *Trans. Met. Soc.* AIME, **233**, 540(1965).
83. A.C. Thorsen and A.J. Hughes, *Appl. Phys. Lett.*, **21**, 579(1972).
84. A.J. Hughes, *J. Appl. Phys.*, **46**, 2849(1975).
85. S. Horiuchi, *Solid State Electron*, **18**, 111 (1975).
86. T.I. Kamins and T.R. CASS, *Thin Solid Films*, **16**, 147 (1973).
87. A.M. Glauert, eds., "Practical Methods in Electron Microscopy," Elsevier, New York, 1972.
88. R. Sinclair, *Indust. Res.*, **15**, 62(1973).
89. G.R. Booker and R. Stickler, *Brit. J. Appl. Phys.*, **13**, 446(1962).
90. E. Biedermann and K. Brack, *J. Electrochem. Soc.*, **113**, 1088(1966).
91. E.S. Meieran, *J. Appl. Phys.*, **36**, 2544 (1965).
92. J.J. Coleman, G. Constrini, S. J. Jeng and C. M. Wayman, *J. Appl. Phys.*, **59**, 428 (1976).
93. W. R. Runyan, "Semiconductor Measurements and Instrumentation, "McGraw- Hill, New York, 1975.
94. M. Ohring, *The Materials Science of Thin Films*, 2nd ed. San Diego: Academic Press, p.586, 2002.
95. R. F. Bushah, ed., "*Deposition technologies for films and Coating*," Noyes, Park Ridge, NJ, 1982.
96. S.M. Sze, ed., "VSLI Technology, "McGraw – Hill, New York, 1983.
97. N.G. Einspruch, ed., "VSLI Handbook," Academic Press, New York, 1985.
98. B. Schwartz and H. Robbins, *J. Electrochem. Soc.*, **108**, 365 (1964).
99. D.L. Klein and D.J.D' Stefan, *J. Electrochem. Soc.*, **109**, 37 (1962).
100. L.H. Blake and E. Mendel, *Solid State Technology*, **13**, 42 (1970).
101. E. Mendel and K. Yang, *Proc. IEEE*, **57**, 1476 (1969).
102. I.J. Pugacz-muraszkiewics and B.R. Hammond, *J. Vac. Sci. Technol.*, 1449 (1977).

103. P.B. Ghate, *Thin Solid Films*, **93**, 359 (1982).
104. B. Petit, J. Pelletier, and R. Molins, *J. Electrochem. Soc.*, **132**, 982 (1985)
105. K.E. Bean, *IEEE Trans. Electron. Dev.*, **25**, 1185 (1978).
106. H.A. Waggener, R.C. Kragness, and A.L. Tyler, *Electronics*, **23**, 274 (1967).
107. D.P. Clemens, *Electrochem. Soc. Extend. Abstr*, **73**, 407 (1973).
108. L.I. Maissel and R. Glang, eds, "*Handbook of thin films Technology*", McGraw-Hill, New York, 1970.
109. A.D. Weiss, *Semicond. Int.*, **16**(11), 73 (1973).
110. A.H. Agajanian, *Solid State Technol.*, **16**(11), 73 (1973).
111. R.B. Herring, *Solid State Technol.*, **19**(5), 37(1976).
112. J.A. Keenan and G.B. Larrabee, vol. 6 VSLI Electronics-Microstructure Science," Academic Press, 1983.
113. H.H. Wieder, *J. Vac. Sci. Technol.*, **18**, 827 (1981).
114. Technical Bulletins – "Data Sheets on GaP, GaAs, GaSb, InP, InAs, and InSb Slices," MCP Electronic Materials, Ltd., Alperton, Wembley, England.
115. Technical Bulletin – "7059 Glass Substrates," Corning, NY.
116. G.A. Keig, *Solid State Technol.*, **15**(9), 53 (1972).
117. G.W. Cullen and C.C. Wang, eds., "Heteroepitaxial Semicondutors for Electronic Devices," Springer- Verlag, New York and Berlin, 1978.
118. Technical Bulletin – "AlSi Base Ceramic Substrates," American Lava Corporation, Chattanooga, TN, 1971.
119. C.C. Allen and E. G. Bylander, ed., "Metallurgy of Semiconductor Materials," Interscience, New York, 1962, p. 113.
120. J.R. Ligenza, *J. Electrochem. Soc.*, **109**, 73(1962).
121. W.A. Pliskin and S.J Zanin, eds., "*Handbook of thin film Technology*," McGraw-Hill, New- York, 1970.
122. B. E. Reason, in "*Modern Workshop Technology*," Part 2, Macmillan, London, 1970, pp-1-51.
123. Technical Bulletin – "The Talystep and the Talysurf – Thin film and surface measuring instrument," Rank Taylor Hobson, Leicester, England.
124. Technical Bulletin – "The Dektak – Surface Profile measuring system," Sloan Technology Corp., Santa Barbara, CA.
125. Technical Bulletin – "The Alpha – Step – Thin film and surface profile measurement," Tencor Instruments, Mountainview, CA.
126. F. C. Eversteyn and G. J. P. M. van der heuvel, J. Electrochem. Soc., **120**, 699, 1973.
127. S. Tolansky, "*Multiple Beam Interferometry of Surfaces and Films*," Oxford University Press, London, 1948.
128. S. Tolansky, "Interferometry," Wiley, New York, 1954.
129. G. R. Booker and C.E. Benjamin, *J. Electrochem. Soc.*, **109**, 1206(1962).
130. M. Bloom, Semicond. Prod., **6**, 26(1963).
131. J.A. Kurtz, *Solid State Technol.*, **13** (12), 64(1969).
132. Bruker(2001).SMART (Version 5.625), SADABS (Version 2.03a) and SHELXTL (Version 6.12). Bruker AXS Inc. Madison, Wisconsin,USA.
133. Bruker (2002). SAINT. Version 6.36a. Bruker AXS Inc., Madison, Wisconsin, USA.

134. G.M. Sheldrick, (1997). SHELX97. Programs for crystal structure Analysis (Release 97-2). University of Gottigen, Germany.
135. K. Swaminathan and H.M.N.H Irving, *J. Inorg. Nucl. Chem.*, **26**, 1292 (1964).
136. E.B. Sandell, *Colorimetric Determination of trace elements*, p. 199. Interscience (1959).
137. A. Yamaguchi, R. B. Penland, S. Mizushima, *J. Am. Chem. Soc.*, **80**, 527 (1958).
138. K.C. Dash and D.V. Ramana Rao, *Indian J. Chem.* **350**, 208 (1967).
139. K.C. Dash and D.V.R. Rao, *Z. Anorg. Allgem. Chem.*, **345**, 217(1966).
140. J.E. O' Connor and E.L. Amma, *Chem. Commun.*, 892(1968).
141. Razik, N., *J. Mater. Sci. Lett.*, **6**, 1443 (1987).
142. Suzuki, T., Yagi, T., Akimoto, S.I., *J. Appl. Phys.*, **54**, 748 (1983).
143. Ulrich, F., Zachariasen, W., Z. Kristallogr., Kristallgeom., Kristallphys, Kristallchem., **62**, 260 (1925).
144. D. Nodland, G. McCarthy, P. Bayliss, North Dakota, USA, ICDD Grant-in-Aid.
145. O. Knop, K.I.G Reid, Sutarno, Nakagawa, Y., *Can. J. Chem.*, **46**, 3463(1968).
146. Caglioti, Roberti, Gazz. Chim. Ital., 62, 20(1932).
147. L. Martin, M. Troemel, *Institut fur Anorganische Chemie*, Frankfurt, West Germany, ICDD Grant-in-Aid, (1989).
148. P. De Wolf, Technisch Physische Dienst, Delft, the Netherlands, ICDD Grant-in-Aid.
149. B.D. Cullity, Elements of X-ray Diffraction, vol. 91, 2nd ed., Addison – Wesley, Readings, MA, 501, 1978.
150. R.A. Bailey and W.J. Tangredi, *J. Inorg. Nuc. Chem.*, **38**, 2223 (1976).
151. G. Kullerund, R.A. Yund, *J. Petrol.* **3**, 126 (1962).
152. N.H. Kolkmeijer, A.L. Th. Moesveld, *Z. Kristallogr.* **80**, 91 (1931).
153. M. Laffite, *Bull. Soc. Chim. Fr.* 1211 (1959).
154. M. Nakumura, A. Fugimori, M. Sacchi, J.C. Fuggle, A. Misu, *Phys. Rev. B*, **48**, 16942(1993).
155. O. Goede, W. Heimbrodt, V. Weinhold, *Phys. Status Solidi B*, **11**, 146(1988).
156. Hu. Yong, Jia fu Chen and Xiaolong Li, Adv. *Funct. Mater*, **14**, 386(2004).
157. P.R. Herezfeld, *Physica*, **39**, 439(1968).
158. K.S. Ramaiah, R. D. Pilkington, D. Tomlinson and A.K. Bhatnagar, *Mater. Chem.* Phys, **68**, 22(2001).